Design Studies for an Air Fluorescence Telescope with Silicon Photomultipliers for the Detection of Ultra-high-energy Cosmic Rays

von

Christine Peters

Masterarbeit in Physik
vorgelegt der

MATHEMATISCH-NATURWISSENSCHAFTLICHEN FAKULTÄT
der Rheinisch-Westfälischen Technischen Hochschule Aachen

im

September 2013

angefertigt im

III. Physikalischen Institut, Lehrstuhl A

Erstgutachter und Betreuer

Prof. Dr. Thomas Hebbeker
III. Physikalisches Institut A
RWTH Aachen University

Zweitgutachter

Prof. Dr. Christopher Wiebusch
III. Physikalisches Institut B
RWTH Aachen University

Contents

Chapter 1

Introduction

The field of research of astroparticle physics combining high-energy particle physics, cosmology and astrophysics, allows an extended look into the universe.
While astronomical objects and phenomena are extensively studied by astronomy, astroparticle physics focuses on the physical processes and production mechanisms behind the phenomena which are still unknown. Therefore, cosmic particles are used as messengers from the universe, among them ultra-high-energetic ($E > 10^{18}\,\mathrm{eV}$), charged particles.
These ultra-high-energy cosmic rays (UHECRs) constantly penetrate the atmosphere of the Earth. While interacting with molecules of the air, an avalanche of secondary particles is initiated. An extensive air shower (EAS) develops and can be observed by large ground-based detectors.

The largest experiment on the southern hemisphere studying UHECRs is the Pierre Auger Observatory located in Argentina. It is based on a hybrid design using two complementary detection techniques to obtain a detailed observation of the EAS: On the one hand the surface detector consisting of water Cherenkov tanks determines the lateral distribution of the shower by the detection of charged particles reaching the ground. On the other hand the fluorescence detector studies the full development respectively the longitudinal distribution of the shower by the detection of fluorescence light in the UV regime. This ultraviolet light is emitted by the de-excitation of molecules in the air, which have been excited by charged particles of the shower, as electrons and positrons.

The fluorescence detector of the Pierre Auger Observatory consists of 24 telescopes based on the Schmidt-camera layout. The incoming light is reflected by a spherical mirror onto a focal plane instrumented with 440 Photomultiplier tubes (PMTs) each having a maximal quantum efficiency of approximately 25 % in the fluorescence wavelength regime. The spherical aberrations introduced by the mirror are reduced by implementing a Schmidt corrector ring. This improvement of the image quality allows an increased aperture in respect to a Schmidt telescope without a corrector. The design of each telescope allows to efficiently detect cosmic rays with an energy above $10^{17}\,\mathrm{eV}$, but has to cope with a low duty cycle of about 10 % since measurements can only be taken in moon- and cloud-less nights.

For the next generation of fluorescence telescopes a higher sensitivity to detect the faint flushes of EAS is mandatory to increase statistics as well as spatial and energy resolution. Silicon photomultipliers (SiPMs) are promising light detection devices discussed to replace the currently used PMTs and to improve the light detection efficiency, in particular due to their expected high photon-detection efficiency of up to PDE $\simeq 60\,\%$ for prospective generations of SiPMs.

The prototype FAMOUS (First Auger Multi-pixel photon counter camera for the Observation of Ultra-high-energy-cosmic-ray air Showers) is designed and built to test the feasibility of the detection of cosmic rays by an SiPM camera. It is based on a refractive design using a Fresnel lens to focus the light onto the focal plane consisting of 64 pixels. The simulated, expected performance of the prototype is very promising.

As the detection principle of cosmic rays with SiPMs will be proven by FAMOUS, the question arises, how to make the best use of an SiPM camera in a large ground-based experiment as the Pierre Auger Observatory. In principal, two basic ideas are conceivable: An experiment consisting of large aperture fluorescence telescopes located at large distances between each other or an experiment consisting of smaller telescopes with a smaller spacing.

In the context of this thesis, design studies have been performed based on simulations to optimise the optical baseline design of a large aperture telescope for the detection of fluorescence light with SiPMs. After an introduction into the theory of cosmic rays in chapter 2, the detection techniques and the detectors used at the Pierre Auger Observatory are explained in chapter 3. Chapter 4 describes the optical baseline design of FAMOUS discussing each component in detail and its expected performance. Chapters 5 and 6 focus on the design studies of two different telescope baseline designs. First, the refractive design of the FAMOUS prototype is analysed for the use of a large Fresnel lens. In chapter 6, the reflective design based on the Schmidt-camera layout is investigated and optimised for the detection of fluorescence light with an SiPM camera. Chapter 7 gives an outlook on further studies to evaluate the best application of an SiPM camera for the detection of ultra-high-energy cosmic rays.

Chapter 2

Cosmic Rays

In 1912, Victor Hess found a first indication of a radiation coming from the cosmos which constantly penetrates the Earth. Those cosmic rays are charged, energetic particles whose kinetic energy range covers several orders of magnitudes from MeV up to beyond 100 EeV. Although this discovery was made more than 100 years ago, many properties still remain unknown. Studying cosmic rays is therefore a major area of research (overview given by [67]). The common theoretical models and the main observational results are summarised in this chapter (for more details see [28], [80]).

The best datasets for the lower energy range $E = [10^{10}\,\text{eV}\,,\,10^{14}\,\text{eV}]$ have been obtained in space experiments by direct measurements [79]. At the highest energies $E > 10^{17}\,\text{eV}$, the cosmic ray flux is very low less than $1\,\text{m}^{-2}\,\text{year}^{-1}$, and detectors in space are strongly limited in size and weight. Therefore, the ultra-high-energy cosmic rays with $E > 10^{18}\,\text{eV}$ (UHECRs) can be observed only by indirect measurements. When cosmic rays hit the Earth's atmosphere, they interact with nuclei high in the atmosphere. Each of these interactions initiates a cascade of secondary particles which can be studied by very large ground based experiments.

In this thesis, the focus will be on the detection of UHECRs with the fluorescence detection technique. The particles of the cosmic rays are strongly influenced by intergalactic magnetic fields on their trajectory from their origin to the Earth. The resulting deflection decreases with increasing energy of the particles. Thus, UHECRs point back to their place of origin and their sources, and the production mechanisms can probably be identified with better accurracy than for lower energies cosmic rays.

2.1 Energy Spectrum

The energy of cosmic rays follows a power law spectrum, $J(E) \propto E^{-\gamma}$. The differential flux J corresponding to the number of cosmic rays per area, time, solid angle and energy is shown in figure 2.1 as a function of the energy above $10^{12}\,\text{eV}$ [28]. The spectrum is multiplied by a factor of $E^{2.5}$ to emphasise the spectral shape.

The spectrum below $E = 10^{15}\,\text{eV}$ falls steeply with a spectral index $\gamma = 2.7$ which leads to a decrease of the differential flux by a factor of 500 for an increase of one order of magnitude in energy. Above the first structure in the spectrum (the knee) the differential flux decreases even steeper by a factor of $\simeq 1000$ per order of magnitude with $\gamma \simeq 3.0$.

Due to this sharp decline, different detection techniques are required for measurements of the cosmic ray flux in the low respectively the high energy range. Therefore, a complete spectrum has to be compiled with data from direct and indirect measurements.

Knee The first structure in the energy spectrum is the knee at an energy of around $5 \cdot 10^{15}$ eV. Here, the slope of the spectrum becomes even steeper with a spectral index of $\gamma \simeq 3.0$ corresponding to an integrated flux of $1\,\mathrm{m}^{-2}\,\mathrm{year}^{-1}$ [62]. It is believed to be a rigidity-dependent feature. The rigidity $R = pc/Ze$ is characterised by the ratio of the momentum of a cosmic ray particle to its electric charge. There are two general theoretical ideas to explain the origin of the knee. On the one hand, the maximal energy for the acceleration in galactic sources can be reached. On the other hand, the knee refers to the leakage of particles from the Galaxy. Particles with smaller rigidity are more confined in the Galaxy and escape later, which leads to a smooth transition to a steeper spectrum above the knee [56].

Second Knee At an energy of $4 \cdot 10^{17}$ eV the spectrum steepens and has a slope with a spectral index of $\gamma \simeq 3.1$.

Ankle It is not obvious how particles in this energy region are accelerated ($E = 4 \cdot 10^{18}$ eV). Certain models suggest that at the ankle, extragalactic acceleration becomes the significant process [15]. Above the ankle the spectrum flattens again to the same spectral index as below the knee.

Cutoff Large scale experiments measure a rapid drop of the flux above $E > 10^{19}$ eV. The integrated flux at the highest energies is about one cosmic ray per km^2 and century. This absence of the flux is commonly interpreted by two alternative models. The structure can be described by assuming the cutoff as the upper end of the source energy spectrum. Indeed, including propagation of the primary particles through the extragalactic medium would lead to an unfavoured injection spectrum at their origin of $dN/dE \sim E^{-1.6}$ [12], [11] which is difficult to reconcile with common acceleration mechanisms (cf. chapter 2.2). Another commonly accepted explanation of the drop is the theoretical GZK (Greisen-Zatsepin-Kuzmin) cutoff: At an energy of $E \sim 6 \cdot 10^{19}$ eV protons start to interact with photons of the cosmic microwave background (CMB).

$$p + \gamma_{\mathrm{CMB}} \rightarrow \Delta^{+} \rightarrow \begin{cases} p + \pi^{0} \\ n + \pi^{+} \end{cases}$$

The proton loses energy, while pions are produced. This leads to a maximal distance (GZK horizon) which an ultra-high-energetic proton can travel. This GZK horizon is strongly energy-dependent. Protons, reaching the Earth with an energy above 10^{20} eV, have to originate from very near sources within maximal 100 Mpc.

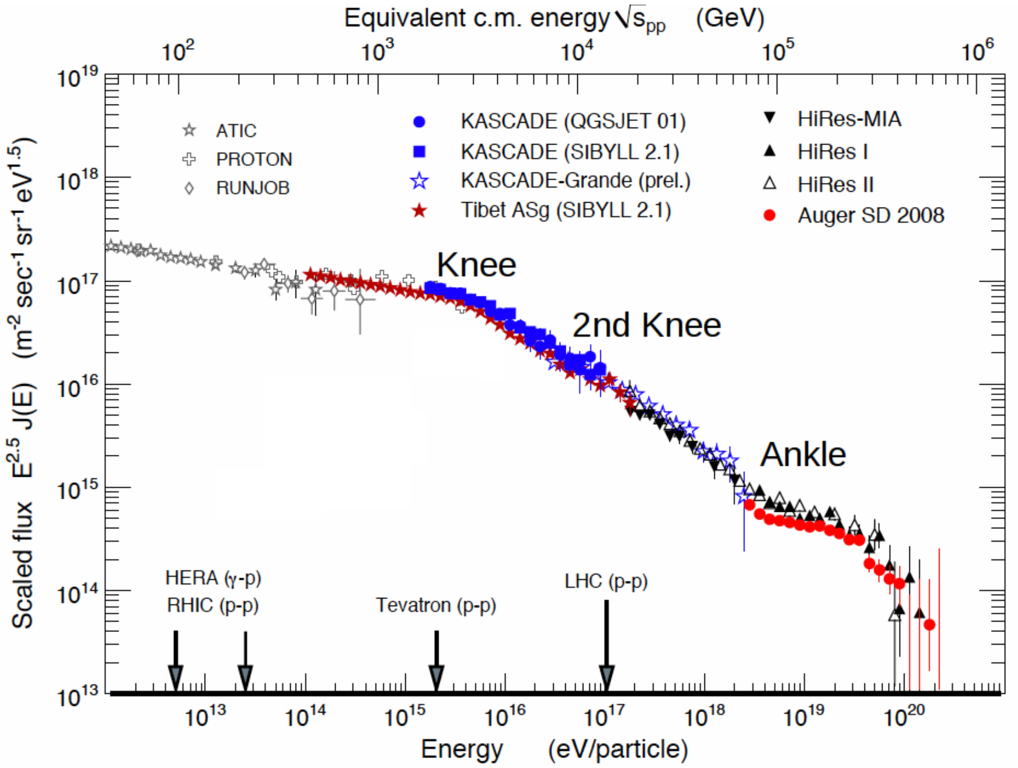

Figure 2.1: The differential flux of cosmic rays as a function of their energy. For a better illustration of the shape, the differential flux is multiplied by $E^{2.5}$. The spectrum is measured by several experiments, below $10^{14}\,\mathrm{eV}$ by direct observation (Atic, PROTON, RUNJOB), above by indirect detection of air showers. Four general features can be observed: the knee ($E = 5 \cdot 10^{15}\,\mathrm{eV}$), the second knee ($E = 4 \cdot 10^{17}\,\mathrm{eV}$), the ankle ($E = 4 \cdot 10^{18}\,\mathrm{eV}$) and a cutoff ($E > 10^{19}\,\mathrm{eV}$). The very low flux at the highest energies leads to limited statistics. Adapted from [28].

2.2 Possible Sources and Acceleration Mechanisms

Candidates for the sources of cosmic rays (CR) can be identified by understanding the possible acceleration processes or by constraints due to the features in the energy spectrum (chapter 2.1). However, many source candidates are left and the exact origin of CR is still unknown [49].

Introduced by Enrico Fermi in 1949, stochastic acceleration of charged particles is a commonly accepted acceleration mechanism [46]. The stochastic acceleration in shock fronts turns out to be an efficient process and a smooth power law spectrum is predicted as seen by experiments (depicted in figure 2.1). An acceleration is achieved by diffusion of a particle on the turbulent magnetic fields in the shock region leading to stochastic crossing of the shock front. At each crossing the particle gains energy. The constant energy gain is proportional to the shock velocity $\beta_s = v_s/c$ (first-order acceleration). The total energy gain of a particle is determined by how many times the particle crosses the shock front. At each cycle it is possible for the particle to leave the shock region.

The maximal achievable energy $E_{\max}$ strongly depends on the characteristics of the shock region, the magnetic field B, its size R and the shock velocity β_s referring to the efficiency of the shock acceleration [28]. As acceleration is possible as long as the magnetic fields are strong enough to confine a particle, the maximal energy E_{max} increases for particles with higher charge. Therefore a heavy, charged nucleus can achieve a Z times higher energy than a proton.

$$E_{\text{max}} \simeq 10^{18} eV \cdot Z \cdot \beta_s \cdot \left(\frac{R}{\text{kpc}}\right)\left(\frac{B}{\mu G}\right) \tag{2.1}$$

An illustration of the relations between those quantities is given in figure 2.2 for different astrophysical objects: Particles up to the energy of the knee are believed to be of galactic origin [6]. Supernova remnants (SNR) are attractive candidates for the acceleration of galactic cosmic rays. About 10 % of the entire kinetic energy of an SNR is needed to accelerate the cosmic rays to the required energy. Supernova remnants are characterised by an expanding shock wave developing with a velocity v_s of about 0.1 c.

The Hillas plot (cf. figure 2.2) demonstrates also that for a 10^{20} eV proton other sources than SNR are needed. For UHECR only few possible candidates fulfill the requirements including Active Galactic Nuclei (AGN), colliding galaxies or Gamma Ray Bursts (GRB).

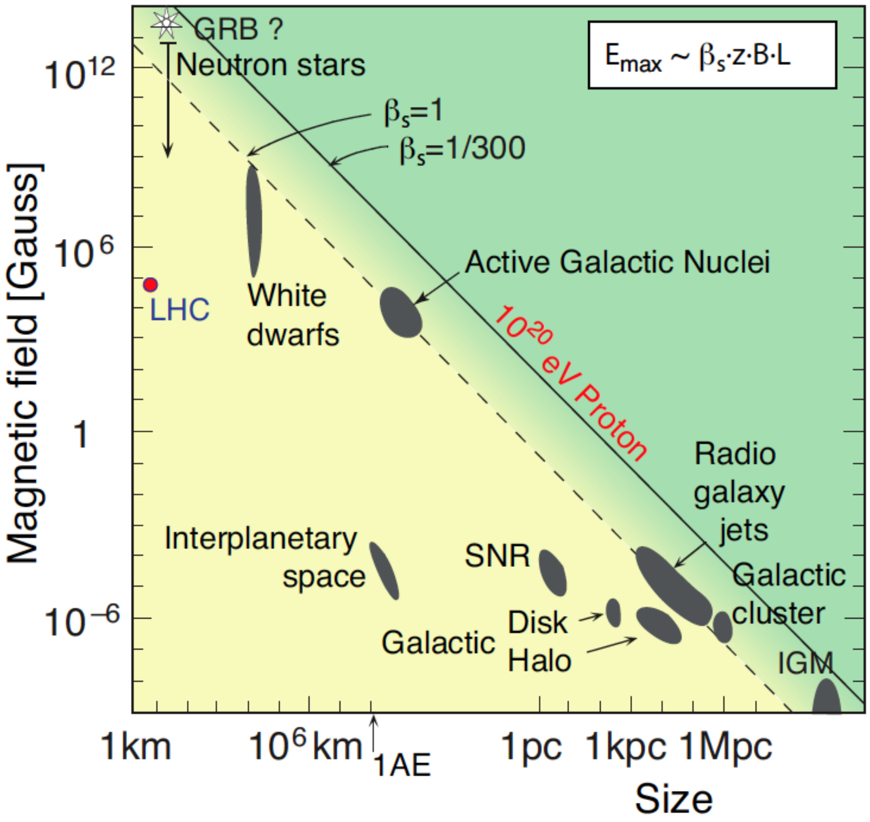

Figure 2.2: Hillas plot giving an overview about candidates for the Fermi acceleration of charged particles depending on their magnetic field B and size R. Objects which can accelerate protons up to an energy of 10^{20} eV have to lie above the lines. The dashed line corresponds to the acceleration in relativistic shocks $\beta_s \simeq 1$. Taken from [28], original Hillas plot from [54].

2.3 Extensive Air Showers

An extensive air shower (EAS) initiated by a single cosmic particle can be described as a cascade of secondary particles which travels through the atmosphere towards the ground (for more details see [22]). Along the cascade more interactions will take place, producing not only millions of particles, but also radio emission, Cherenkov radiation and fluorescence light. In the scope of this thesis, the fluorescence light is particularly relevant. Its production mechanism due to energy losses during the EAS and its detection principle will be clarified in more detail in chapter 3.1.

A schematic of the development of an EAS is shown in figure 2.3. A shower can be classified by three parts which contribute mainly to the cascade: An electromagnetic, an hadronic and a muonic part. After the first interaction the EAS consists mainly of hadrons like pions and kaons decaying or interacting during the further development of the air shower. At the ground, a shower leaves a footprint consisting mainly of photons, electrons/positrons, and of muons originating from the decay of kaons and pions.

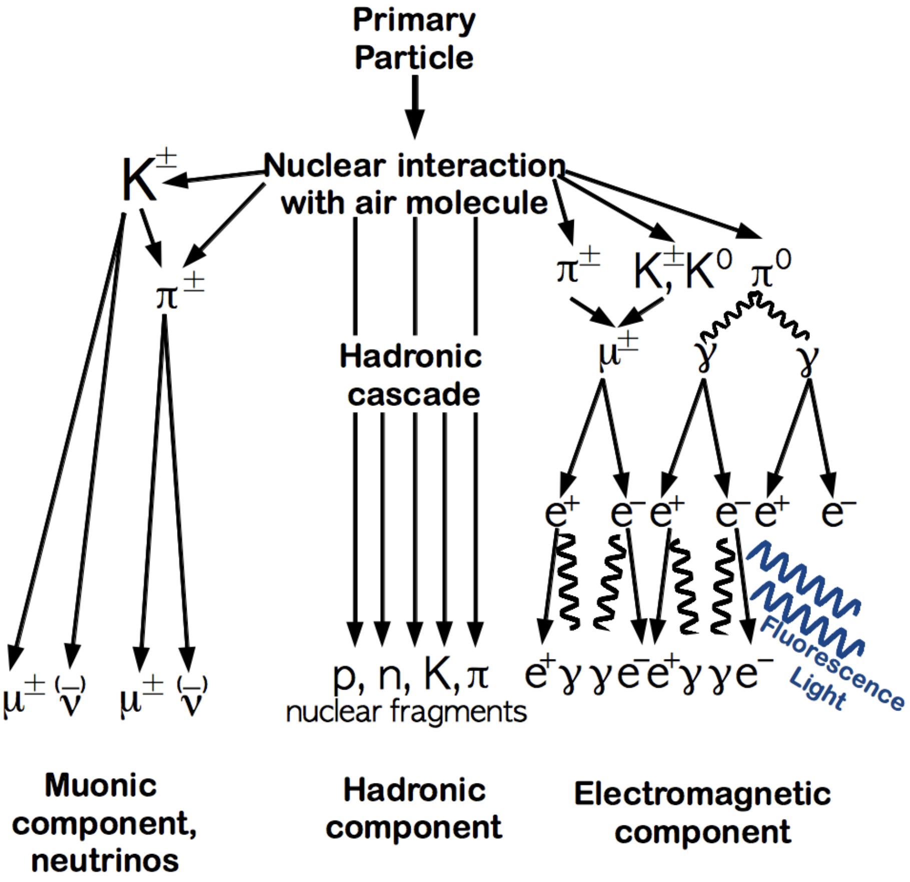

Figure 2.3: Scheme of the three main components of an extensive air shower initiated by an energetic primary of the cosmic rays. Adapted from [25]. Secondary particles are produced, but also fluorescence light is radiated. Fluorescence light is caused by the energy deposit of charged particles, mainly electrons/positrons, in the shower. The main part of the fluorescence light originates thus from the electromagnetic component of the shower [74]. Thereby, the electromagnetic component is fed by the hadronic component as a large part of the energy of the latter goes into new electromagnetic showers.

A simple model for the description of the electromagnetic component is the Heitler model [65]. The cascade is described by a pure electromagnetic shower for which the atmosphere acts like a calorimeter with a vertical thickness of more than 11 interaction lengths [62].

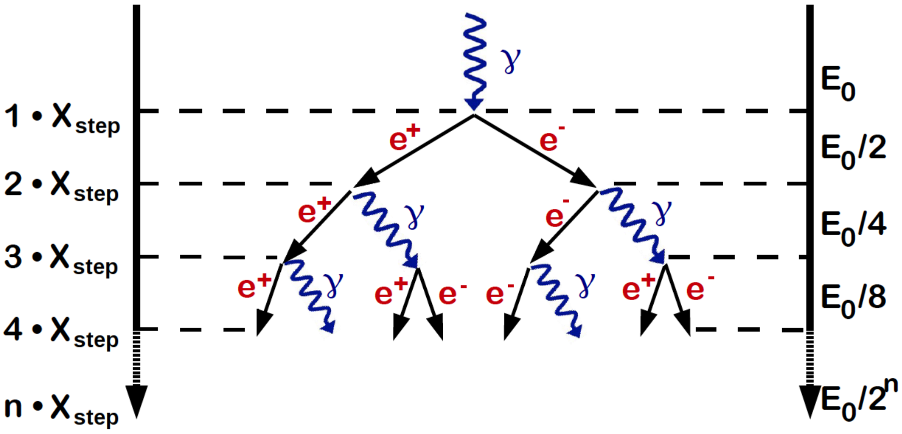

Figure 2.4: Schematic diagram of Heitler's model of an electromagnetic shower development. After each interaction step length X_{step} two secondary particles are generated via bremsstrahlung or pair production. Thereby, each secondary carries half of the energy. The energy of a particle after n steps of interaction corresponds then to $E = E_0/2^n$ whereby E_0 refers to the energy of the particle initiating the shower. Adapted from [65].

Heitler's model of an electromagnetic shower is shown in figure 2.4. The cascade develops like a tree whereby at each interaction two secondary particles for each particle are produced. Interactions take place after equal step lengths X_{step}. Thus, the number of particles N at a step n can be described by

$$N = 2^n \qquad . \tag{2.2}$$

Two possible interactions are assumed: An electron emits a photon via bremsstrahlung carrying half of the energy of the electron. The photon in turn can interact with a nucleus and create a pair of electron and positron via pair production whereby both have equal energy. Taking only these two interactions into account, the step length is given by the radiation length of the medium λ_r, leading to a step length of $X_{\text{step}} = \lambda_r \cdot \ln 2$ corresponding to about $26\,\text{g/cm}^2$ [62] in air.

This simplification can be maintained only as long as the energy loss of electrons via bremsstrahlung dominates over the energy loss by ionisation. When ionisation becomes the more likely process the shower has reached its maximum and the shower will die out. In air, the maximum of the shower is reached when the energy of the particles drop below the critical energy of approximately $E_c = 80\,\text{MeV}$ [62].
At the critical energy E_c, the two components of the energy losses are the same: It depends thus on the radiation length λ_r characterising radiation losses and the Bethe-Bloch formula $\alpha(E)$ characterising ionisation losses at a certain energy [27]

$$E_c = \alpha(E_c) \cdot \lambda_r \qquad . \tag{2.3}$$

The energy losses of the particles is determined by the amount of matter they pass through. Taking inclined air showers into account, the amount of traversed matter $X(\theta, h)$ as a function of the altitude h increases for higher incidence angles θ regarding the normal to the ground. The slant depth can expressed by the product of the atmospheric depth for vertical shower $X_v(h)$ and a geometrical factor:

$$X(\theta, h) = X_v(h) \cdot \frac{1}{\cos(\theta)} \quad . \tag{2.4}$$

The atmospheric depth is calculated by integrating the density of air along the trajectory of the shower.

$$X_v(h) = \int_h^\infty \rho(h)\,\mathrm{dh} \tag{2.5}$$

Most interactions take place in the stratosphere ($\rho_0 = 1.35\,\mathrm{kg\,m^{-3}}$, $h_0 \simeq 7250\,\mathrm{m}$), here the density is approximately given by the barometric formula

$$\rho(h) \simeq \rho_0 \cdot \exp\left(-\frac{h}{h_0}\right) \quad , \tag{2.6}$$

which leads to a vertical depth of

$$X_v(h) \simeq 1000\,\mathrm{g\,cm^{-2}} \cdot \exp\left(-\frac{h}{h_0}\right) \quad . \tag{2.7}$$

Although the description of an extensive air shower by Heitler's model is very simple, some important facts for the observation of EAS can be concluded.
The depth of the first interaction point of the EAS is defined as X_1. The energy of the original cosmic ray can be deduced either by measuring the slant depth of the shower maximum $X_{\max}$ and the number of particles at the maximum $N_{\max}$, or by counting particles reaching the ground:

$$N_{\max} = \frac{E_0}{E_c} \quad , \tag{2.8}$$

$$X_{\max} = X_1 + \lambda_r \cdot \ln \frac{E_0}{E_c} \quad . \tag{2.9}$$

A good approximation to describe the longitudinal profile of an electromagnetic shower is given by the 4-parameter-Gaisser-Hillas function [48]. The number of particles as a function of the slant depth X is given by

$$N(X) = N_{\max} \left(\frac{X - X_1}{X_{\max} - X_1}\right)^{\frac{X_{\max} - X_1}{\lambda}} \exp\left(\frac{X_{\max} - X}{\lambda}\right) \quad , \tag{2.10}$$

parametrised by the depth of the first interaction X_1, the depth of the shower maximum $X_{\max}$, the maximum number of particles $N_{\max}$ and a shape parameter $\lambda \simeq 70\,\mathrm{g/cm^2}$ [88]. The development of the shower strongly depends on the primary particle as heavier

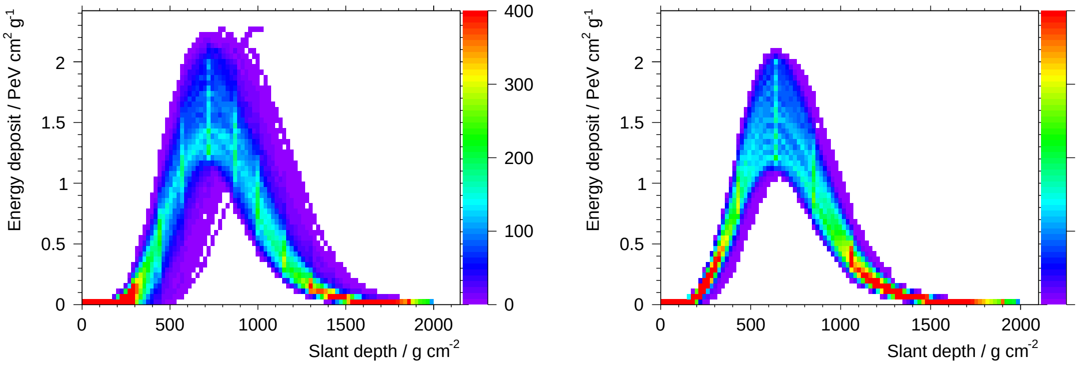

(a) Proton (b) Iron

Figure 2.5: Shower-to-Shower fluctations for different primaries. Shown is the energy deposit as a function of the slant depth for 1000 CONEX [71] simulations per primary at an energy of $E = 10^{18}\,\mathrm{eV}$.

particles interact higher in the atmosphere.
Studying the longitudinal profile allows a distinction between heavy and light primaries, respectively to determine the chemical composition of UHECRs.

A method for the measurement of this Gaisser-Hillas profile is thereby the fluorescence detection technique employed at the Pierre Auger Observatory as presented in the next chapter.

2.4 Chemical Composition

Cosmic rays are studied by different detection techniques in the low and the high energy regime. In the lower energy range up to the knee, the flux is large enough for direct measurements. The abundance of the elements in the CR can be studied in detail by experiments located above the atmosphere. The chemical composition is determined as 79% protons, 15% helium and 2% electrons [45]. The small fraction left is composed of heavier elements whereby the abundance decreases with increasing mass.

For UHECR only indirect measurements are possible. Properties as the longitudinal profile and the density distribution of particles on the ground of the observed extensive air showers theoretically allow to identify the primary particle which triggered the shower. Fluctuations in the shower development, even for one particular type of primary, make a determination of the initiating particle in a single event very difficult. Hadronic interactions lead to large shower-to-shower fluctuations. In figure 2.5 shower-to-shower fluctuations for two types of primaries, proton and iron, are shown. A shower of a heavier particle develops faster and higher in the atmosphere leading to less fluctuations. Conclusions on the particle properties have to be drawn from statistical properties of a large data set of air showers. Therefore, only the average mass composition and the variance of the distribution can be determined.

In an air shower an enormous amount of secondary particles is produced, and thus, after few interaction lengths, the shower development can be described as a function of a small set of parameters. This universality leads to an average description of an air shower development. Common parameters used for this description are the total energy of the shower, the depth of the shower maximum X_{max}, the stage of shower evolution and the number of muons at a particular reference point [24].

Around the knee, the main parameter to distinguish between primaries is the muon component. The ratio of the electron to muon component at ground decreases with increasing primary mass as more high energetic muons are produced in the first hadronic interaction. At the same time, the first interaction will take place earlier in the atmosphere and the electromagnetic component will die out. Thus, less electrons will reach the ground. This effect is used as a discriminator by several experiments, along them KASCADE (KArlsruhe Shower Core and Array DEtector) [18] and KASCADE-Grande [19] in Karlsruhe. Generally, it can be observed, that the knee occurs at higher energies for an increasing mass of the primary particle. This behaviour is expected, if the steepening of the energy spectrum at the knee is a rigidity-dependent effect.

The observation of the depth of the shower maximum X_{max} is another potential discriminator. It characterises the longitudinal shower development. For instance, it can be measured by fluorescence detectors by the amount of emitted fluorescence light (for more details see chapter 3.1).

As already mentioned, the first interaction point of heavier elements takes place earlier in the atmosphere. Therefore, the depth of the shower maximum is expected to be smaller for heavy particles (determined by the average of the simulations shown in figure 2.5):

$$\left\langle X_{\mathrm{max,\,p}}(10^{18}\,\mathrm{eV})\right\rangle \simeq 749\,\mathrm{g/cm^2}, \quad \left\langle X_{\mathrm{max,\,Fe}}(10^{18}\,\mathrm{eV})\right\rangle \simeq 643\,\mathrm{g/cm^2} \quad . \tag{2.11}$$

An analysis at the Pierre Auger Observatory (introduced in the next chapter 3.2) of the mean depth of shower maximum, $\langle X_{\mathrm{max}}\rangle$, at the highest energies indicates a change to a heavier composition (see figure 2.6).

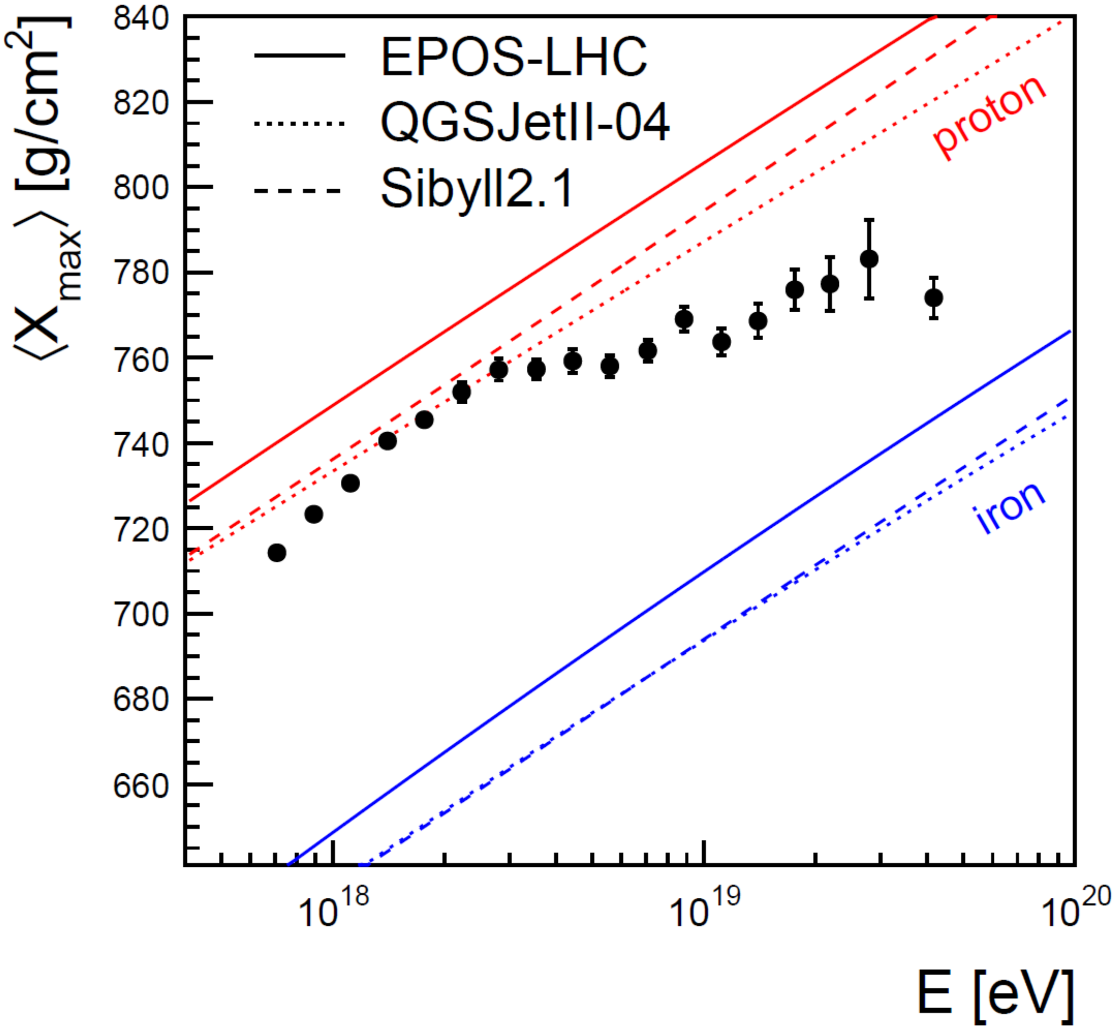

Figure 2.6: Average depth of shower maximum as a function of energy. Measurements of the Pierre Auger Observatory of UHECR are shown compared with three hadronic interaction models for two primary particles, p and Fe. Figure is taken from [42].

Chapter 3

Detection of Ultra High Energy Cosmic Rays at the Pierre Auger Observatory

For the detection of ultra-high-energy cosmic rays (UHECRs) large experiments are needed due to the very low flux at the highest energies. Space experiments are limited in weight and size, therefore only an indirect measurement of UHECRs at ground or from satellites [36] is possible. The atmosphere of the Earth is opaque for cosmic rays (CR). When one of its particles hits the atmosphere, it will interact with an air nucleus and an extensive air shower (EAS) is initiated. Studying the development of EAS by detection of the secondary particles on the ground (chapter 3.2.2) respectively the radiated fluorescence light (chapter 3.1), it is possible to draw conclusions on the original cosmic ray properties.

3.1 Fluorescence Light Emission from Atmospheric Nitrogen

The detection of fluorescence light is one of the most sensitive detection techniques to study the longitudinal profile of extensive air showers (for more details see chapter 2.3). The fluorescence light is produced by charged secondary particles in particular electrons/positrons in the electromagnetic component of the cascade. Travelling through the atmosphere towards the ground, the charged particles excite the molecules in the air. By de-excitation the molecules emit isotropically photons in the ultraviolet wavelength regime which allows a three dimensional observation of the shower. The fluorescence light spectrum is composed of several spectral bands extending from 290 nm to 440 nm and depends on the humidity and pressure of the atmosphere. In principle, all kind of molecules of the air may be excited and emit fluorescence light. The main component of the atmosphere are thereby nitrogen $\sim 78\,\%$, oxygen $\sim 21\,\%$ and argon $\sim 1\,\%$. As the transition from the excited state to the ground state is strongly forbidden for the most excited states of oxygen [37] and most of its emission lines have a wavelength not included in the wavelength regime of fluorescence light, only few and weak emission lines occur in the fluorescence light spectrum. Therefore, the spectrum is dominated by the emission of nitrogen molecules [21].

At the same time, ultraviolet Cherenkov radiation is emitted by polarisation of the medium during the development of the EAS [30]. In contrast to the fluorescence light, the Cherenkov emission shows a continuous wavelength spectrum and is strongly beamed: It propagates as a shock cone along the shower axis. It is possible to study cosmic rays by their Cherenkov radiation, however due to the strong focusing of the light the observation of UHECR by Cherenkov emission is not efficient and is usually considered as background.

The number of the generated fluorescence photons N_γ reaching the aperture of the telescope and being detected by the camera can be described as a function of atmospheric depth X [21]:

$$\mathrm{d}N_\gamma = \int \frac{\mathrm{d}N_\gamma}{\mathrm{d}X}\,\mathrm{d}X \qquad , \tag{3.1}$$

whereby the number of fluorescence photons generated in a layer of the atmosphere with a thickness $\mathrm{d}X$ is expressed by

$$\frac{\mathrm{d}N_\gamma}{\mathrm{d}X} = \int\int \underbrace{Y(\lambda,P,T,u,E)\cdot\frac{\mathrm{d}N_e(X)}{dE}\cdot\frac{\mathrm{d}E_{\mathrm{dep}}}{\mathrm{d}X}}_{\text{fluorescence emission}}\cdot\underbrace{\tau_{\mathrm{atm}}(\lambda,X)\cdot\varepsilon(\lambda,r)}_{\text{detection properties}}\,\mathrm{d}E\,\mathrm{d}\lambda \qquad . \tag{3.2}$$

Two main parts contribute to formula (3.2). The first part describes the production mechanism of fluorescence light. Electrons/positrons excite the nitrogen in the air, their energy spectrum at a specific slant depth is denoted by $\mathrm{d}N_e(X)/dE$. The number of emitted fluorescence photons by de-excitation depends then on the deposited energy $\mathrm{d}E_{\mathrm{dep}}/\mathrm{d}X$ per atmospheric depth and on the fluorescence yield $Y(\lambda,P,T,u,E)$, which depends in general on the wavelength λ, atmospheric pressure P, temperature T, humidity u and energy of the primary E [60], [21]. The second part expresses the transmission losses during the propagation of the photons to the aperture, $\tau_{\mathrm{atm}}(\lambda,X)$, and the detection efficiency of the telescope $\varepsilon(\lambda,r)$.

Fluorescence Yield

The fluorescence yield Y denotes the efficiency of the fluorescence process and is defined as the number of emitted photons per deposited energy.

The fluorescence yield in the atmosphere at the prominent peak in the spectrum (shown in figure 3.1) at 337 nm has been studied by several experiments and the absolute value of Y differs strongly. The AIRFLY (AIR FLuorescence Yield) experiment [23], [29] measured an absolute yield of

$$Y_{337\,\mathrm{nm,absolute}} = 4.12\,\mathrm{photons/MeV} \tag{3.3}$$

while exciting the dry air ($P = 993\,\mathrm{hPa}$, $T = 291\,\mathrm{K}$) by electrons with an energy of $E = 350\,\mathrm{MeV}$.

In spite of deviations between the absolute values, all experimental data, but also theoretical calculations and simulations are consistent with a negligible energy dependence of the yield. Assuming the fluorescence yield as energy independent leads to a number of detected photons proportional to the total energy deposit in the atmosphere $\mathrm{d}E_{\mathrm{dep,\ tot}}$:

$$\frac{\mathrm{d}N_{\gamma,\mathrm{detected}}}{\mathrm{d}X} \propto \frac{\mathrm{d}E_{\mathrm{dep,\ tot}}}{\mathrm{d}X} \qquad . \tag{3.4}$$

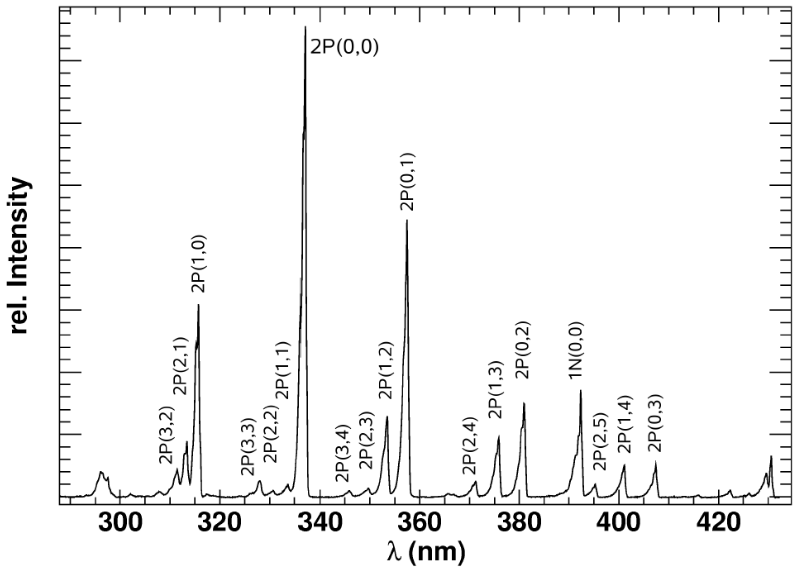

Figure 3.1: Air fluorescence spectrum measured by the Airfly experiment. Atmospheric nitrogen has been excited by $3\,\mathrm{MeV}$ electrons at a pressure of $800\,\mathrm{hPa}$. The major transitions are marked. The $337\,\mathrm{nm}$ band is commonly used as reference peak [23].

Thus, the longitudinal profile of the air shower can be directly determined by the number of observed photons at the detector.

3.2 Hybrid Design of the Pierre Auger Observatory

The Pierre Auger Observatory is the world largest experiment studying ultra-high-energy cosmic rays. It covers an area of around $3000\,\mathrm{km}^2$ of the Argentinian Pampa. The observatory is located near Malargüe, in the province of Mendoza. A map of the area is shown in figure 3.2.

Construction was completed in 2008. Data taking started already 2004 during the construction period. The main concept of the Pierre Auger Observatory is a hybrid detection principle. Two complementary detection techniques are used to successfully observe extensive air showers: the fluorescence detector (FD) and the surface detector (SD) [34], [35].

The fluorescence detector observes the longitudinal development of the air shower and is able to accurately determine the energy deposit. The surface detector measures lateral development, thus the density of secondary particles on the ground. Thereby, the complete shower can be studied in detail to determine important properties of the primary particle. The idea is depicted in figure 3.3.

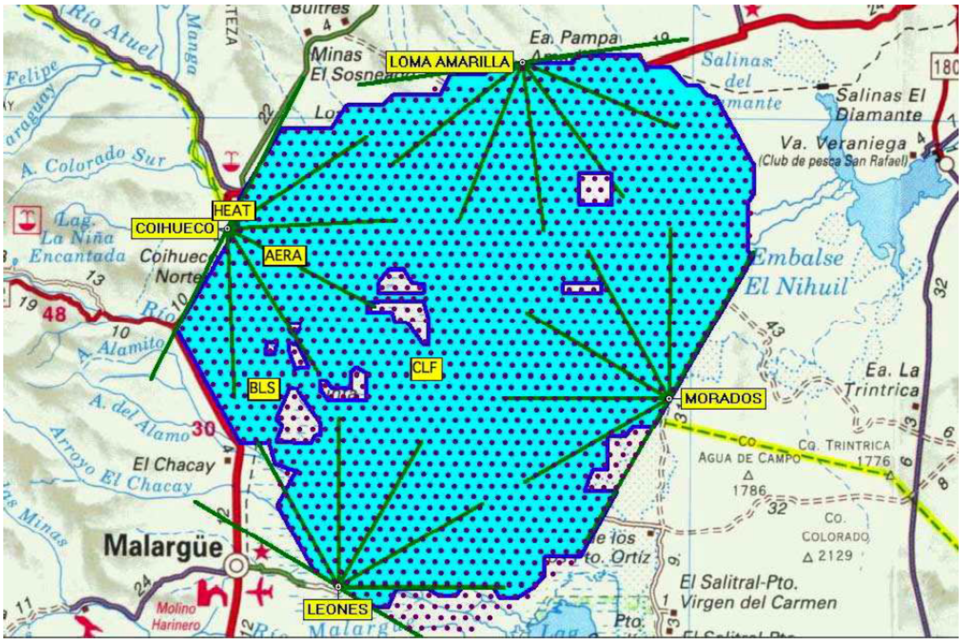

Figure 3.2: Map of present status of the Pierre Auger Observatory. The array is covered by stations of the surface detector (Blue dots). Four fluorescence stations are located at the border of the array. Each station consists of six telescopes, the field of view is indicated by green lines. In addition, extensions of the detectors are shown. Taken from [8].

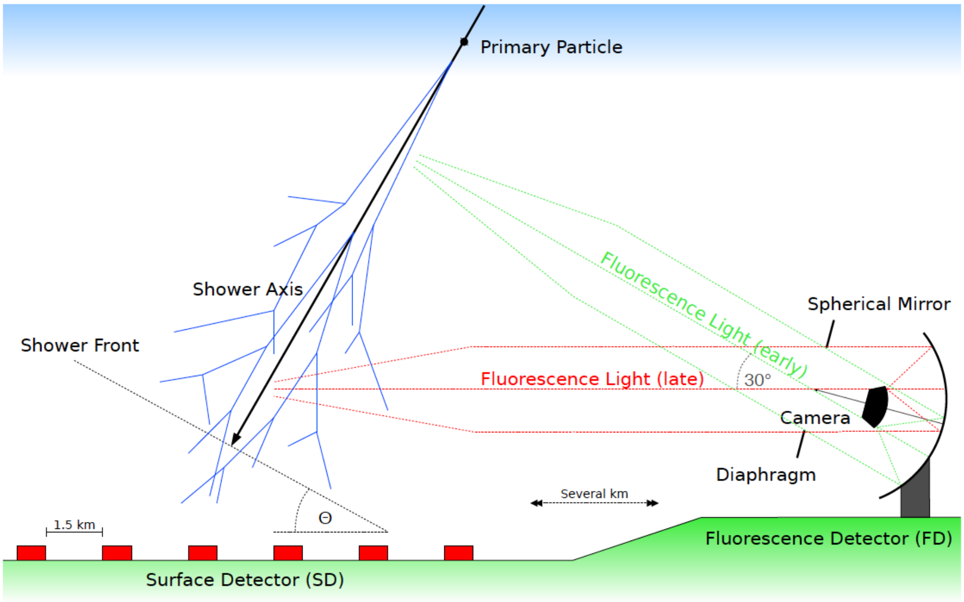

Figure 3.3: Schematic view of an air shower seen by a fluorescence telescope and SD tanks at the ground level. The detection of cosmic rays at the Pierre Auger Observatory is based on a hybrid detection principle. The fluorescence detector allows an observation of the complete longitudinal shower development. The surface detector measures the particle density distribution on the ground. Taken from [82].

3.2.1 The Fluorescence Detector

The fluorescence detector of the Pierre Auger Observatory is composed of four sites located at the borders of the array.

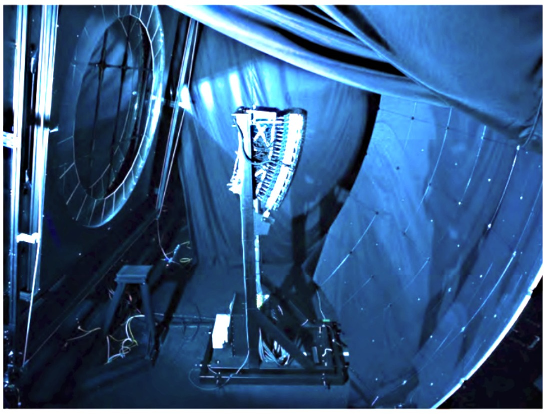

Figure 3.4: A photo of a fluorescence telescope at the Pierre Auger Observatory. In the middle of the frame the camera is visible consisting of photomultiplier tubes. At the right side the spherical mirror is located [33].

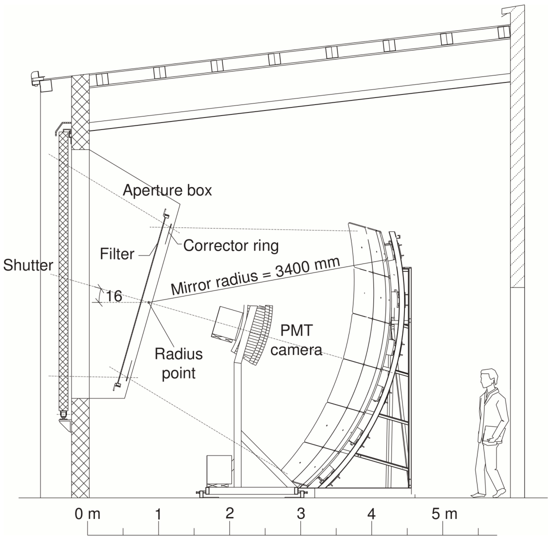

Figure 3.5: A schematic sketch of the fluorescence telescope at the Pierre Auger Observatory. See text for a detailed description. Taken from [5].

Each site contains 6 telescopes whereby each telescope has a field of view (FoV) of 30 ° × 30 °. An observation of the atmosphere over the entire surface array is possible for showers with an energy of approximately 10^{19} eV.
The optical design of the fluorescence telescopes is based on a Schmidt-camera (a picture is given in figure 3.4, a sketch is shown in figure 3.5). The incoming light is focused by a segmented spherical mirror with a diameter of 3.6 m onto the focal plane. The light is detected with a camera consisting of 440 PMT each with a FoV of 1.5 ° × 1.5 ° and a maximal quantum efficiency of approximately 25% in the fluorescence wavelength regime [5].

To reduce the spherical aberration introduced by the spherical mirror a corrector ring is installed at the aperture. The corrector ring has an outer radius of 1100 mm and an inner radius of 850 mm leaving the middle of the aperture free.

The fluorescence light is faint with respect to the night-sky background light from the environment like the moon, stars and artificial light sources. Therefore, the fluorescence detector takes data only in dark moon- and cloudless nights inducing a duty cycle of approximately 10%. For the effective suppression of background light in a different wavelength regime than the fluorescence light, an UV pass filter is integrated at the entrance of the telescope.

The reconstruction principle of the fluorescence telescope is illustrated in figure 3.6 by an event example of the Pierre Auger Observatory.

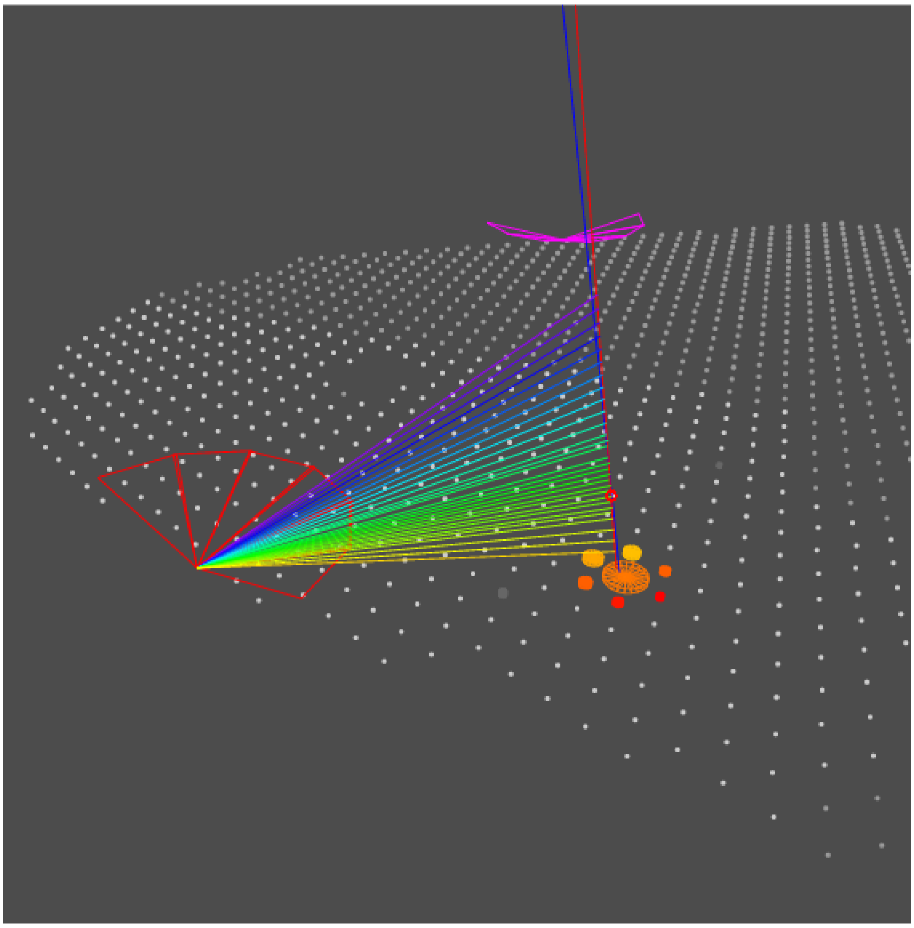

Figure 3.6: Event 201100102713 from February 1, 2011. Hybrid event with an energy of $E \simeq 6{\cdot}10^{18}\,\mathrm{eV}$ seen by fluorescence telescopes in the eye Loma Amarilla and seven surface detector (SD) tanks. The red (fluorescence detector (FD)) and the blue (SD) line indicates the reconstructed axis of the shower. The lines from the FD to the shower axis represents the time arrival of the fluorescence light. The dots mark the triggered SD tanks with color-coded timing information. The size of the dot demonstrates the signal strength recovered by a single SD tank.

When an air shower passes through the field of view of the telescope, the emitted fluorescence light triggers the pixels of the camera (cf. figure 3.7). The arrival time and the amount of light along the track allow to reconstruct the shower axis, the observation angle and the energy deposit (according to equations (3.2) and (3.4)). Therefore, the depth of the shower maximum X_{max} and the energy of the primary particle can be reconstructed by fitting the Gaisser-Hillas formula (equation (2.10)) to the recorded data (figure 3.8).

3.2.2 The Surface Detector

The whole array of the Pierre Auger Observatory is covered by 1660 water Cherenkov tanks in a triangular grid [13]. The distance between two tanks is 1500 m. A sketch of the tank layout is depicted in figure 3.9. Each cylindrical tank covers a $10\,\mathrm{m}^2$ area and is 120 cm

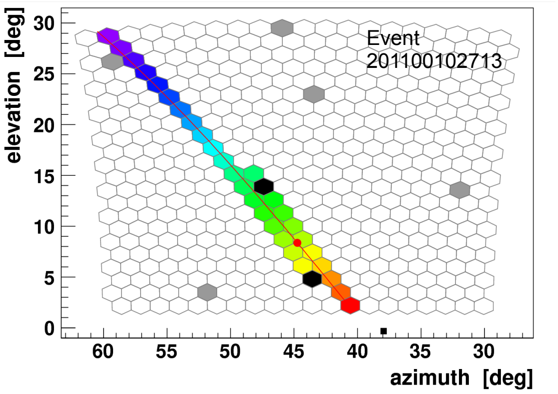

Figure 3.7: Event 201100102713 from February 1, 2011 seen in the camera of Loma Amarilla. The light track is demonstrated by coloured pixels. The time of arrival of the fluorescence light increases from red to blue pixels.

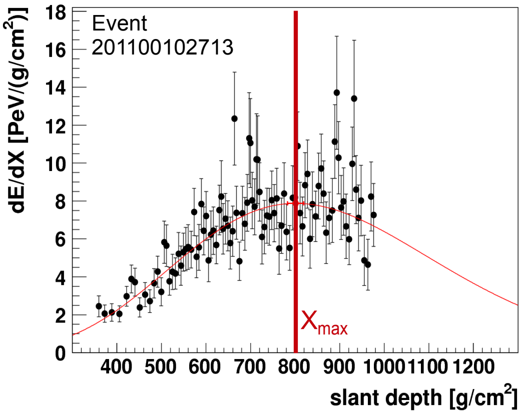

Figure 3.8: Reconstructed longitudinal shower profile (event 201100102713) shown as energy deposit versus atmospheric depth. The Gaisser Hillas fit (red fit) on the FD data (black dots) determines $X_{\text{max}} \simeq 800\,\text{g}/\text{cm}^2$ (red vertical line).

high. The tanks are self-sustaining due to a solar panel and two batteries. Also a GPS receiver and devices for data acquisition, power control and data transfer are installed.

Charged, energetic particles and photons of the extensive air shower reaching the ground are detected in the tanks. Each tank includes three 9-inch photomultiplier tubes (PMT) which detect the Cherenkov light emitted by charged particles travelling through the water. Thereby, the lateral distribution of the particle density on the ground can be determined.

The lateral distribution is linked to the transverse momentum of the scattered particles of the extensive air shower. A commonly used parametrisation of the average lateral distribution is the Nishimura-Kamata-Greisen (NKG) formula [59], [52]:

$$S(r) \propto \left(\frac{r}{r_0}\right)^{-\alpha} \cdot \left(1 + \frac{r}{r_0}\right)^{\alpha-\gamma} \quad . \tag{3.5}$$

$S(r)$ represents the particle density on the ground, dominated by electrons. The parameter r is the distance to the shower core. α, γ and r_0 are shower parameters determined by measurements.

As an energy estimator of the surface detector of the Pierre Auger Observatory $S(1000)$ is well established and refers to the signal measured in the SD tank at a distance of 1000 m from the shower core or interpolated to this distance.

Advantages of the SD are its duty cycle of nearly 100% and a large, uniform exposure. Thus, events can be studied with high statistics. However, the interpretation of the lateral distribution depends strongly on the chosen hadronic interaction model of the air shower simulations for the determination of the energy estimator. This leads to relatively large systematic uncertainties on the energy.

A big advantage of the Pierre Auger Observatory is the possibility to reduce systematic uncertainties of the SD measurements by using the complementary detection technique of the FD. The FD is able to observe the whole development of the shower using the atmosphere as a calorimeter measurement and is less model-dependent. Therefore, the energy of the air shower can be well determined. For hybrid events, the energy measured

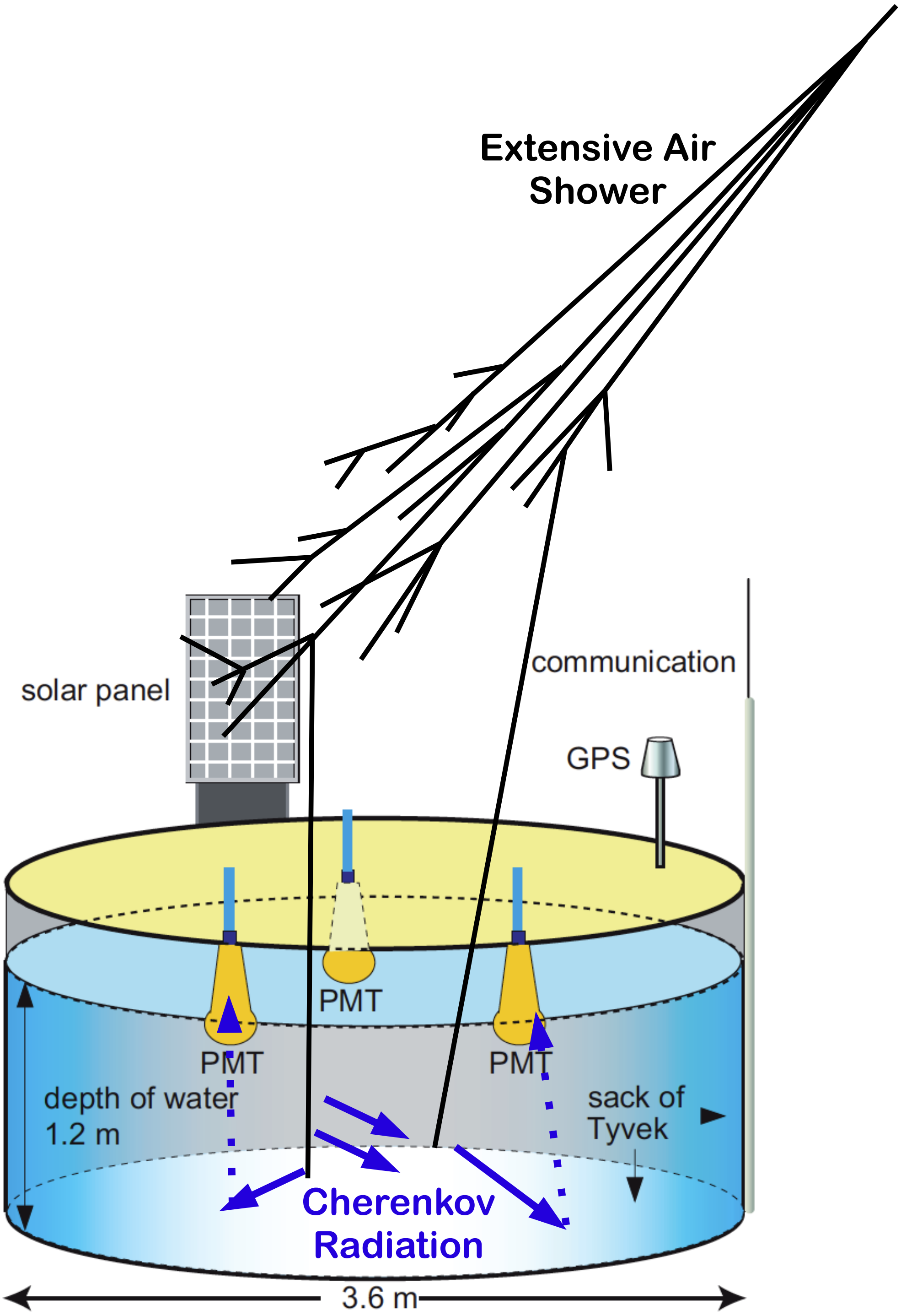

Figure 3.9: Scheme of a surface detector station of the Pierre Auger Observatory. During the development of an extensive air shower millions of secondary particles are produced. Reaching the ground, they can be observed by the tanks of the surface detector. Travelling through the water, charged particles emit Cherenkov radiation which is detected directly or after reflections by photomultiplier tubes. Adapted from [25].

independently by FD and SD can be compared. Thereby, the energy determination of the SD can be calibrated by the energy determination of the FD leading to a better energy resolution of the surface detector.

3.3 Extensions

The Pierre Auger Observatory was built to study the properties of cosmic rays in an energy range above 10^{18} eV. Besides the two main detectors, further extensions have been integrated in the array (more details in [9]).

In 2009, the FD has been extended. The main goal of the High Elevation Auger Telescopes installed near the standard FD site Coihueco is the extension of the energy range to lower energies [66]. Lower energy cosmic rays have a fainter light production and thus lower X_{max} in the atmosphere. Therefore, HEAT is tilted upwards leading to an elevation of $30\,^{\circ} - 60\,^{\circ}$ in field of view (FoV) to increase its efficiency for the corresponding energy regime. A simultaneous observation of the atmosphere by HEAT and the fluorescence site Coihueco provides an elevation angle from the horizon up to $\simeq 60\,^{\circ}$.

Additionally, an infill was deployed in the surface array located in the FoV of HEAT. The smaller distance between the SD tanks in the infill is optimized for the detection of cosmic rays with an energy according to the energy range of HEAT.

The basic concept of the Pierre Auger experiment is the hybrid technique. Apart from fluorescence light and secondary particles, radio pulses are generated in an extensive air shower. The radio emission in the MHz regime is mainly produced by effects of charge separation in the atmosphere as the geo-magnetic effect [76]. The signal strength increases with the square of the energy and is sensitive to the longitudinal profile of the shower. In combination with a duty cycle of nearly 100% the measurement of the radio emission promises an efficient observation of CR.

The Auger Engineering Radio Array (AERA) uses this detection technique to study the properties of EAS by antennas [7]. AERA has been successfully operated with 21 antennas since 2011. At the beginning of 2013, AERA has been expanded to its full size and operates with 124 stations.

Chapter 4

The Fluorescence Telescope FAMOUS

FAMOUS is a novel fluorescence telescope prototype designed and built in Aachen (RWTH Aachen), Lisbon (LIP) and Granada (Universidad de Granada). The acronym stands for First Auger Multi-pixel photon counter camera for the Observation of Ultra-high-energy-cosmic-ray air Showers.

The prototype is based on a refractive optical system which is introduced in the second section of this chapter 4.2. The camera is instrumented with silicon photomultipliers (SiPMs), a relatively new and promising solid-state device for light detection.

4.1 Silicon Photomultiplier Camera

At the moment, the CMS detector collaboration at the Large Hadron Collider inquires into the merits of SiPMs for a possible upgrade of the detector [57]. SiPMs are promising devices due to their immunity to powerful magnetic fields ($B_{\mathrm{CMS}} \simeq 4\,\mathrm{T}$ [32]) and its compactness.

In high energy astroparticle physics, silicon photomultipliers are discussed as a possible replacement of the currently used photomultiplier tubes (PMT) [81]. In contrast to PMTs, SiPMs need a moderate bias voltage of around $30 - 150\,\mathrm{V}$, which could lead to an inexpensive handling in the future.

Experiments in astroparticle physics which detect emitted, faint light with telescopes often have to cope with a very low duty cycle. The currently used PMTs have to be protected against moonlight or direct light of bright stars to guarantee a reliable light measurement and long life time. Illuminated by sunlight the PMTs require very long recovery times. Therefore, the telescopes only take data around moonless nights. The more light-robust SiPMs could allow measurements in a brighter environment yet to the point of dawn. However, the ability of SiPMs to distinguish between the high background and the signal has to be proven first.

Additionally, SiPM prototypes show a very high photon detection efficiency (PDE) up to $60\,\%$ in the UV range compared to $\sim 35\%$ for currently available PMTs (for more details see [1],[2]). A higher PDE increases the sensitivity to detect more distant and lower energy showers. The high-sensitive SiPM types are not yet commercially available, but it is still interesting to build telescope prototypes based on SiPMs to understand the technical challenges.

Apart from the FAMOUS prototype and the research area of UHECR detection, there is also an expanding research on SiPMs in the section of ground-based gamma ray astronomy. For the next generation of Imaging Atmospheric Cherenkov Telescopes (IACTs) [83] a higher sensitivity to detect the faint flushes of Cherenkov light emitted by gamma ray induced air showers is needed. The expected high photon detection capability of future SiPM types offers such an improvement. Based on this new technical device, the prototype gamma ray telescope FACT (First G-APD Cherenkov Telescope) was built. The baseline design of the telescope is a reflective design. The incoming Cherenkov light is focused by a hexagonal mirror of $9.5\,\mathrm{m}^2$ onto the focal plane of the camera consisting of 1440 pixels. The field of view (FoV) of the telescope is $4.5\,°$. The prototype will indicate future developments regarding IACTs using an SiPM camera for light detection. FACT has been already installed at the MAGIC site, La Palma, and first showers have been successfully detected [16], [17].

4.1.1 Geigermode Avalanche Photodiode

Silicon photomultipliers consist of a cellular substructure whereby each cell corresponds to a Geiger-mode avalanche photodiode (G-APD). The cells are connected in parallel on a common silicon substrate.
A photodiode is a semiconductor device with a p-n junction. The topology of an avalanche photodiode is shown in figure 4.1. The device is operated with a reverse bias as the p-doped layer is connected to the anode and the n-doped layer to the cathode. The width of the depletion zone - containing no free charge carriers and formed out between the heavily doped n and p regions - widens by applying a reverse voltage V_{bias}. A high electric field is created.

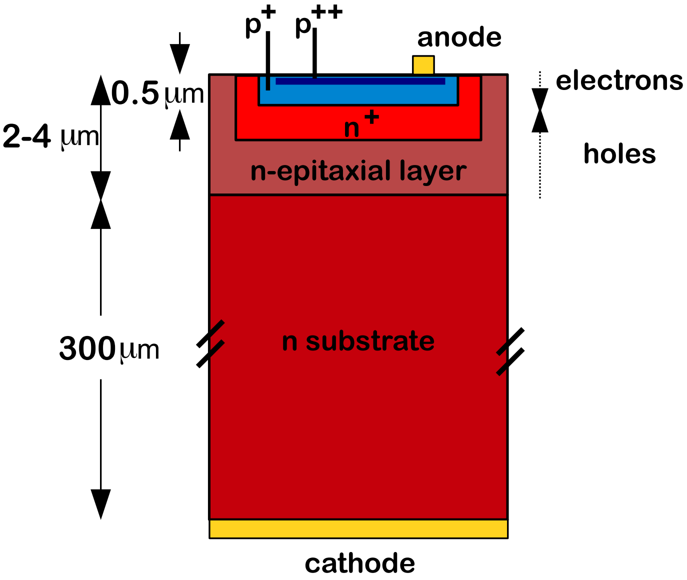

Figure 4.1: Schematic view of the topology of a Geiger-mode avalanche photodiode. Adapted from [26].

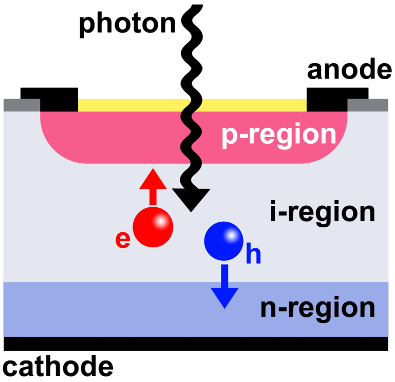

Figure 4.2: Illustration of the detection principle of a photodiode. An incident photon is absorbed in the depletion zone and an electron-hole pair is generated. Due to the drift of the charge carriers in opposite directions, a current is induced. Adapted from [3].

In the depletion zone a free electron-hole pair is generated according to the photoelectric effect when a photon is absorbed (depicted in figure 4.2). The electron and hole carriers drift in opposite directions. This transport process induces an electric current in the

external circuit.
The internal amplification of the photon signal depends strongly on the strength of the electric field. An avalanche photodiode takes advantage of the acceleration of the charge carriers by the field.
If the carriers gain enough energy to create further electron-hole pairs by impact ionization, an avalanche breakdown can occur. An applied voltage V_{bias} larger than the minimal needed voltage for a breakdown of the diode V_{break} is therefore required: The photodiode operates in Geiger-mode.

A G-APD has to be connected in series with a quenching resistor. The avalanche by a cell breakdown is a self-sustaining process and would destroy the photodiode thermally. An additional resistor causes the voltage to drop below the minimal breakdown voltage V_{break} when an avalanche was triggered: the breakdown of the G-APD is terminated. The photodiode then recharges to its initial voltage V_{bias}.

4.1.2 Silicon Photomultiplier

The mechanism of the G-APD is used by silicon photomultipliers. The signal of a single G-APD does not depend on the number of incident photons due to the avalanche process and has a gain of about 10^6. Thus, each G-APD is only a binary device.

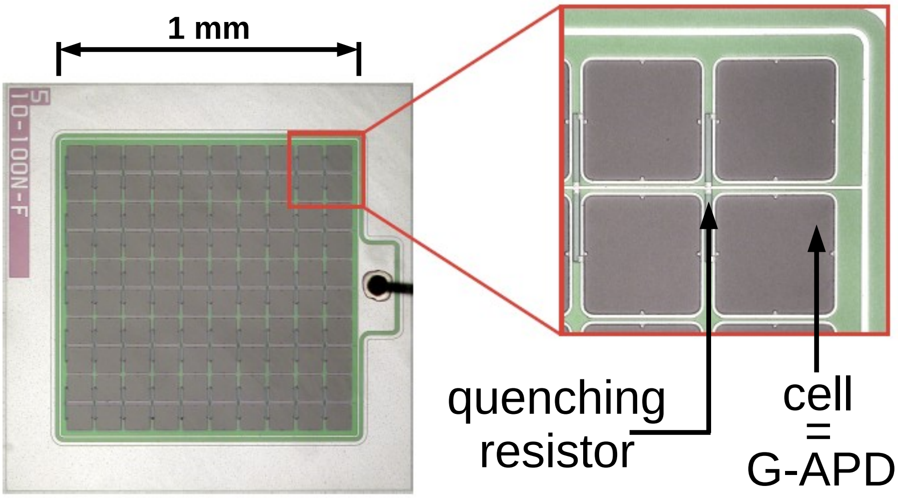

Figure 4.3: Macro-photo of an SiPM. The SiPM has a total area of $1\,\text{mm} \times 1\,\text{mm}$ and consists of 100 cells. Each cell represents a Geiger-mode avalanche photodiode whereby the active area is indicated by the grey squares. The space between the cells is not sensitive. Taken from [57].

The ability to detect multiple photons at once is assured by the arrangement of identical and independent G-APDs in one array as the cells of an SiPM. Thus, the signal of the SiPM is the sum of signals produced by all triggered cells (cf. figure 4.4).
According to the state of the art, SiPMs are available in small sizes of typically $1 - 100\,\text{mm}^2$ consisting of typically $100 - \mathcal{O}(10000)$ cells. A macro-photo of an SiPM is shown in figure 4.3.

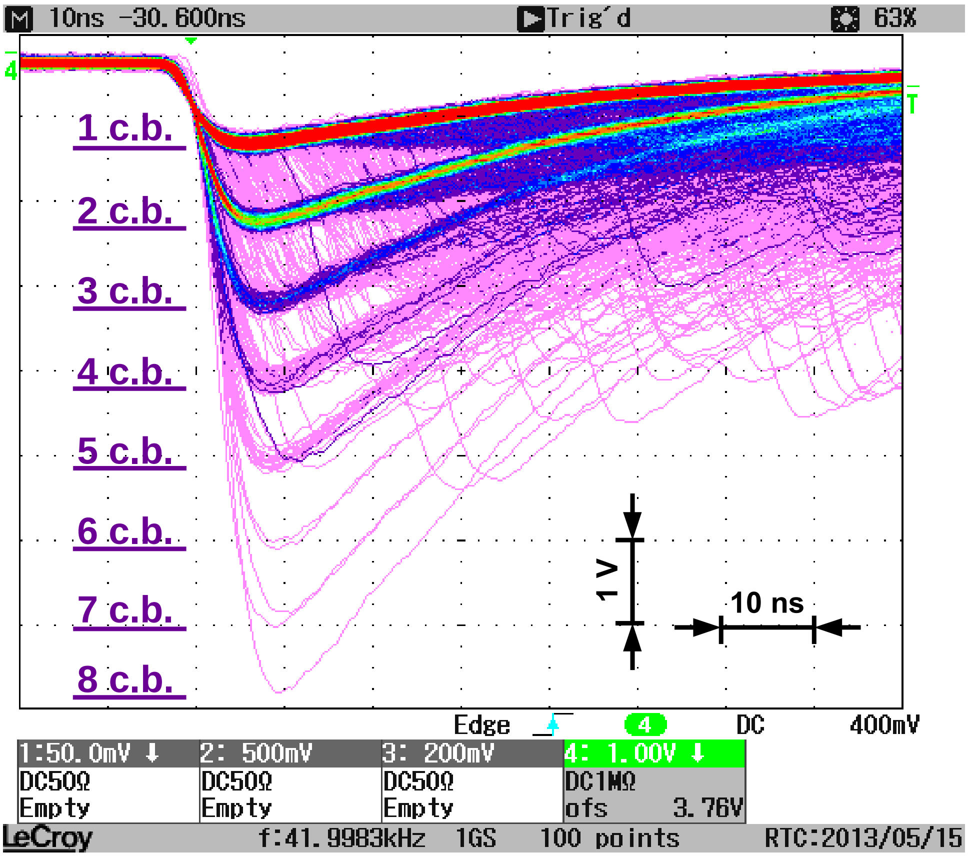

Figure 4.4: Screenshot of an oscilloscope reading. The pulse height depends on the number of cell breakdowns (c.b.). The measurement was performed in darkness with an $1\,\mathrm{mm} \times 1\,\mathrm{mm}$ Hamamatsu [3] SiPM with $100\,\mu\mathrm{m}$ cell pitch defining the length of each cell.

Photon Counting Capability

A high photon detection efficiency (PDE) is a prerequisite for SiPMs as a promising light detection device. The PDE is defined by the quantum efficiency QE, a geometrical factor f_{geom} and the probability to trigger an avalanche by the charge carriers $P_{\text{avalanche}}$ (see figure 4.5):

$$\mathrm{PDE}(\lambda, T) = QE(\lambda, T) \cdot f_{\text{geom}} \cdot P_{\text{avalanche}} \quad . \tag{4.1}$$

The entire SiPM is illuminated by photons. The geometrical fill factor f_{geom} defines the fraction of the SiPM area which is sensitive to light. Dead space is caused by connection electronics and the series quenching resistor which is located on top of the G-APD (cf. figure 4.1). For common SiPM types the fill factor is about 80%. The quantum efficiency QE describes the probability that a single photon incident on the active area of the SiPM generates an electron-hole pair. The probability of the absorption of a photon depends strongly on its wavelength λ, the temperature T and on material properties. The generated charge carriers can than initiate with a probability $P_{\text{avalanche}}$ an avalanche of further electron-hole pairs. The SiPM is operated with a $10-20\%$ higher voltage than the minimal needed voltage V_{break} to ensure that each cell works in Geiger-mode. Therefore, the probability to trigger a cell breakdown is approx. 100% if a photon is absorbed.

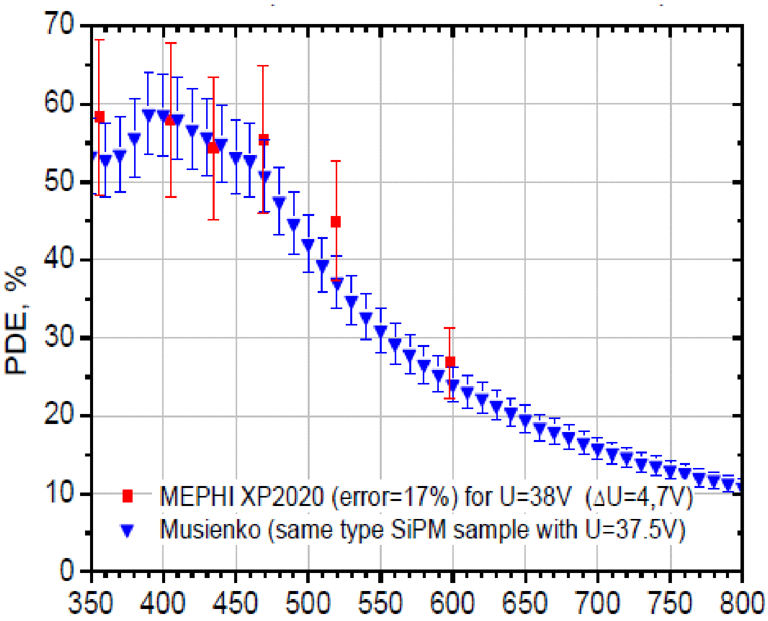

Figure 4.5: The photon detection efficiency (PDE) for a SiPM prototype (XP2020) determined at MEPHI and at CERN by Y. Musienko [43]. A high PDE up to 60% in the UV region is measured. The prototype is not yet commercially available.

Noise Phenomena of SiPMs

The noise of an SiPM is defined by cell breakdowns initiated not by absorbed photons but from other effects. Noise phenomena can be distinguished between thermally generated noise and correlated noise. The latter includes optical cross-talk by self-emitted photons and after-pulsing by delayed release of trapped charge carriers. Noise phenomena are highly temperature- and voltage-dependent as shown in figure 4.7. The noise probability increases also with the number of cells.

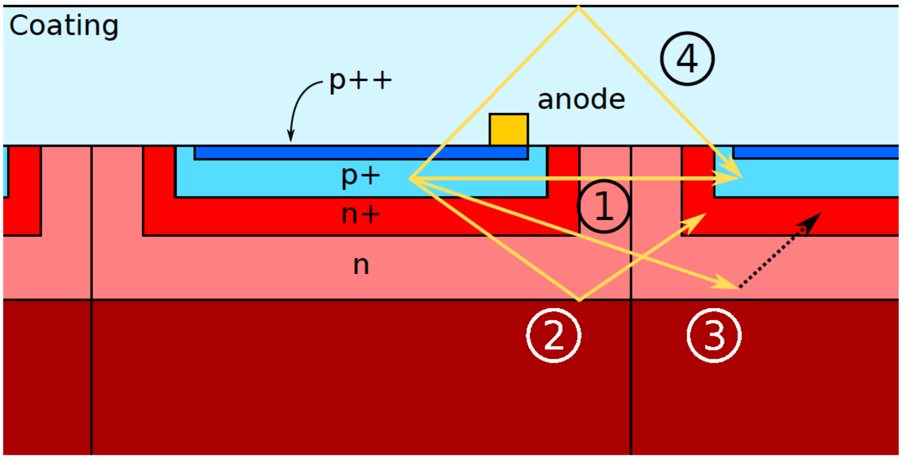

Figure 4.6: Scheme of different optical crosstalk processes: ① direct transmission; ② reflection at boundaries; ③ generation of charge carriers drifting into depletion zone and triggering a breakdown; ④ reflection at inner boundary of the coating layer [82].

Optical Crosstalk

During the avalanche breakdown free charge carriers can recombine and photons are emitted. The optical cross-talk between cells causes adjacent cells to be fired. In figure 4.6 the different processes of cross-talk are depicted: ① direct transmission and absorption in the neighbouring cell; ② photon is reflected at the inner boundaries of a G-APD; ③ photon cross over in the n-doped layer of the adjacent cell, generates an electron-hole pair drifting into the depletion zone and triggers an avalanche; ④ photon leaves the active area of the G-APD and is reflected at the inner boundary of the coating layer onto the neighbouring cell. For an efficient suppression of cross-talk, trenches can be used as an optical separation between cells [61], but also leading to a smaller geometrical fill factor. A determination of the cross-talk probability to $P = 10 - 30\,\%$ depending on SiPM characteristics and temperature has been performed by [64].

After-pulsing

Free charge carriers can be trapped at impurities of the semiconductor during the avalanche discharge. After they are released, they can trigger with a probability of $P \approx 10 - 40\,\%$ a new breakdown in the same cell during a period of several 100 ns. Thereby, two characteristic time constants $\mathcal{O}(10\,\mathrm{ns})$ and $\mathcal{O}(100\,\mathrm{ns})$ have been identified from measurements (studied by [64]).

Thermal Noise

Thermal noise results from random electron-hole pairs generated thermally in the depletion region of the G-APD structure. The thermal noise rate is $f \approx 1\,\mathrm{kHz\,cell}^{-1}$ and increases strongly with increasing temperature. The probability for two coincident thermal noise events in one SiPM depends strongly on the time gate of the readout electronics, the number of cells of the SiPM and the ambient temperature. The estimated probability for a $1\,\mathrm{mm} \times 1\,\mathrm{mm}$ SiPM with 100 cells ($f \approx 100\,\mathrm{kHz} \Rightarrow \tau = 10000\,\mathrm{ns}$) to trigger two coincident thermal noise events in a time gate $t = 20\,\mathrm{ns}$ is thus about $P_{2\,\mathrm{th}} = 1 - e^{-t/\tau} \approx 0.2\,\%$. Contrary to correlated noise, thermal noise does not need a trigger by a previous cell breakdown. Thereby, the signal produced by incoming light or thermal noise is nearly without distinction.

By dark count measurements noise effects can be studied in detail. Therefore, an SiPM is operated in total darkness. The signal is dominated by thermal noise. Additionally, correlated noise can occur triggered by a previous, thermally or correlated noise generated breakdown. A scheme of a trace (figure 4.8) illustrates the correlation between the three noise effects. An in-depth understanding of all noise effects and dependencies allows to reconstruct the initial photon flux onto the SiPM from measurements of the output signal.

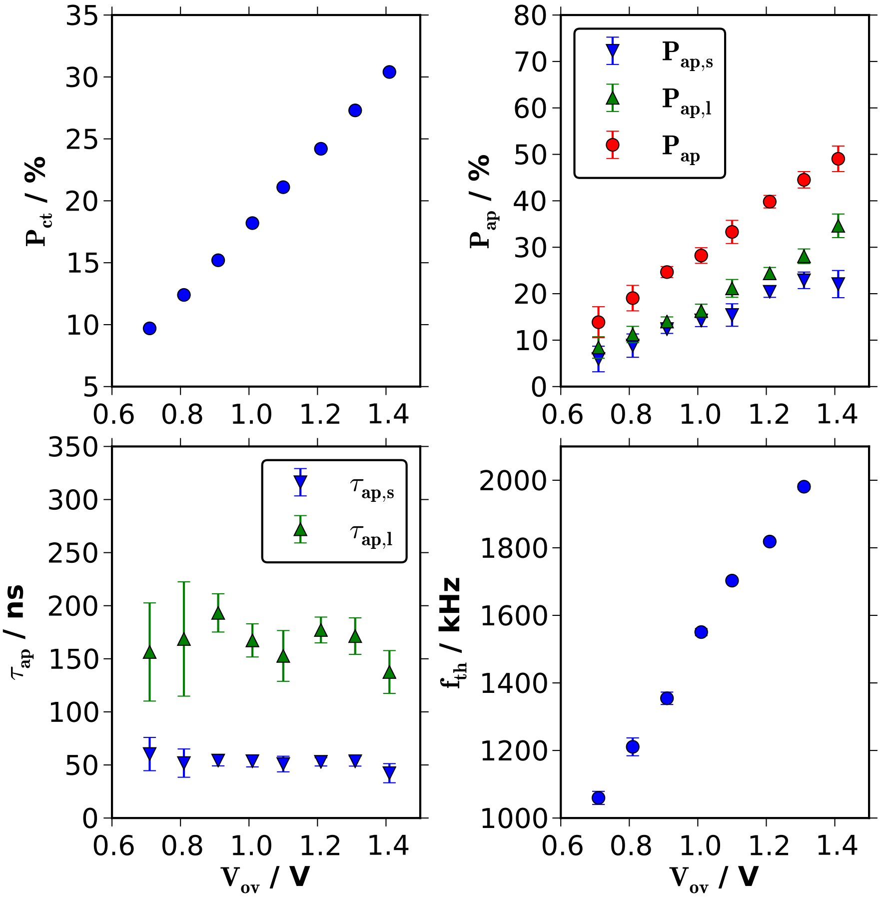

Figure 4.7: SiPM operation parameters as a function of the overvoltage V_{OV}. Shown are measurements for a Hamamatsu S10362-33-100C SiPM with 900 cells at an ambient temperature of $T = (3.76 \pm 0.03)\,^\circ C$ of the crosstalk-probability P_{ct} (top left) and the afterpulse-probability P_{ap} for the two characteristic time constants and the combinated probability (top right). Also, measurements of the two afterpulse time constants $\tau_{ap,s}$ and $\tau_{ap,l}$ (bottom left) and the thermal noise rate f_{th} of the entire SiPM (bottom right) are depicted [68].

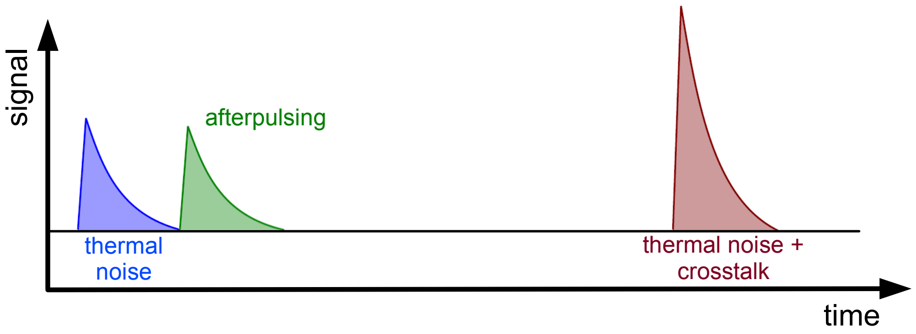

Figure 4.8: Scheme of correlation between noise effects and their influence on the trace of an SiPM. Thermal noise occurs randomly and produces a signal-like pulse. If optical crosstalk appears, an additional cell is triggered immediately. After-pulsing induces with delay an additional pulse with slightly variable height depending on the recovery status of the cell.

4.2 Baseline Design

The FAMOUS prototype is based on a refractive optical design (cf. figure 4.9). A Fresnel lens focuses the incoming light onto a focal plane consisting of 64 pixels hexagonally arranged. Each pixel consists of a Winston cone concentrating the incoming light onto the light detector device (SiPM). FAMOUS will observe cosmic rays induced air showers by detection of the emitted fluorescence photons. Therefore, a UV pass filter, optimised for the wavelength regime of the fluorescence light, is mounted between the light concentrator and the SiPM. In the following sections, each optical component of the prototype is reviewed in detail.

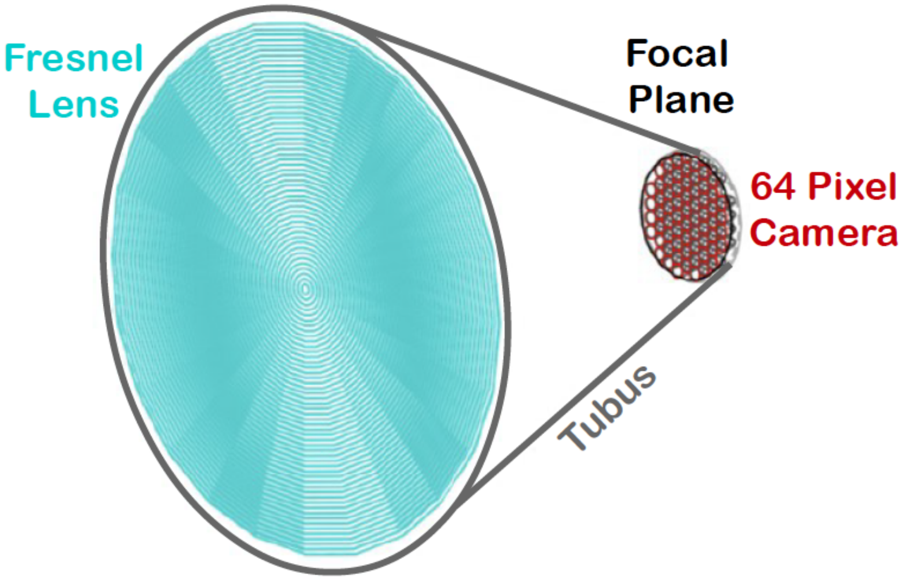

Figure 4.9: Baseline design of FAMOUS. It is based on a refractive optical system using a Fresnel lens to focus the light onto the 64 pixel camera. Each pixel consists of a Winston cone, a UV pass filter and a silicon photomultiplier. Shown is the screenshot of a Geant4 simulation.

This refractive design allows a high transmission of the whole optical system as no detection unit obstructs the light beam as for example in a Newton telescope or in the Schmidt optics used at the Pierre Auger fluorescence detector. The important quantities are presented in figure 4.10: The aperture with diameter D, the focal length f, the radius of the focal plane r_{fp}, the total field of view (FoV) α_{FoV} of the telescope and the incident angle β of the focused beam on the focal plane.

These quantities have to be determined for the specific design of FAMOUS.
The focal length f is thereby defined as:

$$f = \frac{r_{\mathrm{fp}}}{\tan\left(\frac{\alpha_{\mathrm{FoV}}}{2}\right)} \quad . \tag{4.2}$$

The radius of the focal plane r_{fp} is defined by the number of pixels N_{px} and the size of each pixel referring to the entrance radius r_1 of the used Winston cone as light concentrator (detailed information in chapter 4.2.2):

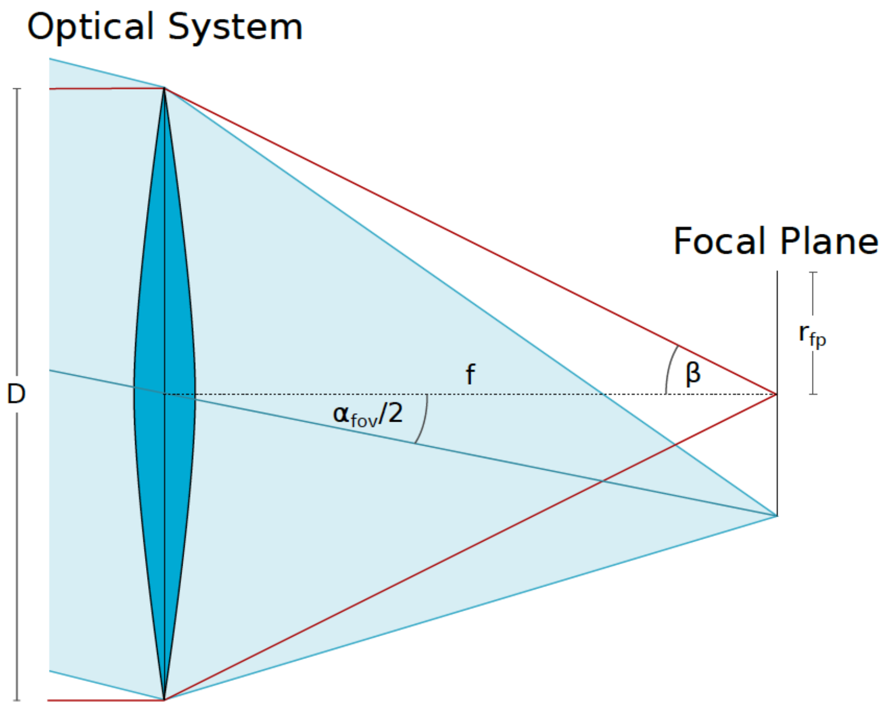

Figure 4.10: Sketch of an unspecific refractive optical design [82]. Presented are the important quantities of a baseline design: The aperture diameter D, the focal length f, the focal plane radius r_{fp}, the total field of view (FoV) α_{FoV} of the telescope and the incident angle β of the focused beam on the focal plane.

$$r_{\mathrm{fp}} = \sqrt{N_{\mathrm{px}}} \cdot r_1 \qquad . \tag{4.3}$$

Winston cones accept angles up to a certain angle θ_{max}. The incident angle onto the focal plane is therefore limited and corresponds for an incident angle of $\theta_i = 0$ on the lens to

$$\tan(\beta) = \frac{D/2}{f} \quad \leq \quad \tan(\theta_{\mathrm{max}}) \qquad . \tag{4.4}$$

There are fixed parameters for the FAMOUS baseline design: the number of pixels $N_{\mathrm{px}} = 64$ as well as the FoV per pixel $\alpha_{\mathrm{px}} = 1.5^\circ$ which has been chosen to be the same as for the Auger FD telescope (cf. chapter 3.2.1).
The size of the prototype compromises between being inexpensive, mobile, compact, built out of commercially available components and a high signal sensitivity. A compact telescope can be achieved by requiring a focal number $N_f = f/D \simeq 1$.

The optimisation of the optical design has been performed by ray-tracing simulations [82]. ZEMAX [4], a commercial optical software program often used by optical engineers, allows a fast determination of an optimal setup.
A more in-depth study and a possible integration into a complete detector response simulation program of experiments are given by the Geant4 toolkit [10], [14]. The software based on object-oriented programming is used in a variety of experimental research areas including high energy, medical or astrophysics. The tracking of particles through matter

includes all relevant physical processes and interactions. The three dimensional geometry allows the construction of highly complex structures.
The FAMOUS design is fully simulated using the Geant4 simulation tool and enables a response simulation of the entire detector (discussed later in chapter 4.3).

4.2.1 Fresnel Lens

Developed in 1822 by Augustin Jean Fresnel, a Fresnel lens is able to reduce weight, absorption and cost of a conventional bulky lens by basically preserving its refractive power. The Fresnel lens is versatile and is commonly used in light houses and photovoltaic systems ([63] gives a review). The basic principle and structure of a Fresnel lens is summarised, then the design and optimisation of the FAMOUS Fresnel lens is described in the following section.

Construction of Fresnel lens

A Fresnel lens is designed by dividing a conventional lens into concentric annular zones („grooves“) of same height maintaining the surface curvature of the original lens [40]. The lens surface curvature can thereby be described by the profile equation $s(r)$ depending on the radial distance r from the lens surface to the centre of the lens

$$s(r) = \frac{c \cdot r^2}{1 + \sqrt{1 - (k+1) \cdot c^2 \cdot r^2}} + \sum_{i=1}^{\mathcal{O}(j)} A_{2i} \cdot r^{2i} \qquad . \tag{4.5}$$

The curvature c corresponds to the inverse of the bending radius and k is the conic constant describing the geometrical shape:

$k = 0$ sphere
$k = -1$ parabola

The surface profile is extended by perturbation terms describing aspherical deformation. It is expressed by a sum of even polynomials of aspheric constants A_i and the radial distance r.

The Fresnel lens is built out of a light, but also robust material. A long lifetime, an inexpensive production and a high concentration power is desired. UV transparent acrylic (polymethylmethacrylate, PMMA) is thereby the commonly used lens material.

For FAMOUS a powerful and highly efficient concentrator is needed and Fresnel lenses are promising candidates. Important parameters are the focal length f and the size of the lens D, which are usually fixed by the baseline design, as well as the granularity. The granularity refers thereby to the number of grooves per mm. The focal length defines the distance between the lens and the point where a perfectly collimated beam converges. The size of the lens determines the aperture of the whole telescope.

A ray-tracing simulation of a Fresnel lens based on a parabolic shaped bulky lens to avoid spherical aberrations has been performed to optimise the design for the requirements of the telescope [82], [38]. Each groove has a conical instead of a parabolic shape, which is for a sufficiently large set of grooves a good approximation. The conical shape reduces also the needed calculation time and power and refers to the commonly applied shape of grooves for available Fresnel lenses. The grooves are located onto a common base plate and are orientated towards the source.

An illustration, how a Fresnel lens is constructed from an aspheric lens, is shown in figure 4.11: The bulky lens is divided into grooves with equal width. The height of each groove is calculated according equation (4.5). The thickness of the Fresnel lens d_{thick} is then defined by summing up the height of the highest groove and the thickness of the base plate.

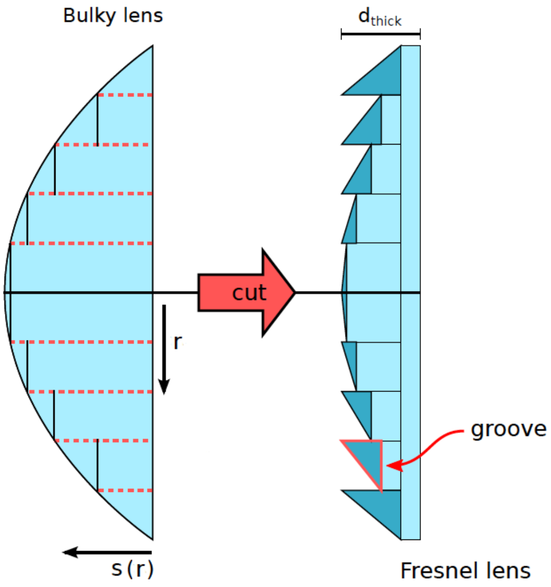

Figure 4.11: Illustration of the construction principle of a Fresnel lens. A conventional parabolic lens is divided into grooves reducing the thickness and therefore weight and absorption of the lens to a minimum. All grooves are located onto a common base plate and are orientated towards the source. The sum of the height of the highest groove plus the thickness of the base plate defines d_{thick}. Taken from [82].

Dividing a lens into grooves introduces sharp edges which increases the probability of reflections and disturbances of the beam. Furthermore, Fresnel lenses suffer from optical aberrations, also reducing the image quality. Therefore, the image quality is the most crucial parameter.

Image Quality Criterion - Point Spread Function

Light passing through an optical system is detected on a focal plane. The intensity distribution of the light on the plane is defined by the point spread function (PSF). The degree of blurring of an ideal point source at the plane can be used to evaluate the image quality of the system. For FAMOUS, the incoming light has to be focused into one camera pixel. Also a sharp and homogeneous image is necessary.
A commonly used quality criterion is the aberration radius r_{90}. The radius refers to the

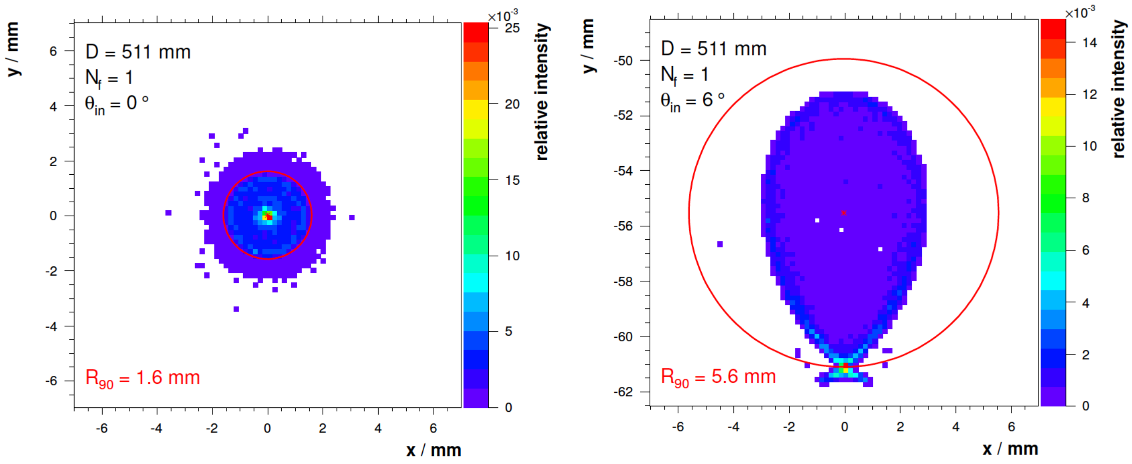

(a) incident angle $\theta_{in} = 0\,^\circ$ (b) incident angle $\theta_{in} = 6\,^\circ$

Figure 4.12: Simulated sampled point spread function for two different incident angles on the lens θ_{in} covering the complete angular range of the FAMOUS prototype [82]. Influences of optical aberrations become more obvious for larger incident angles. The distance between the focal plane and the Fresnel lens is $518.6\,\mathrm{mm}$. In red the aberration radius r_{90} is shown encircling $90\,\%$ of the total energy.

radius of a circle including $90\,\%$ of the total amount of energy.
For a better understanding, an illustration of the simulated sampled point spread function is shown in figure 4.12. The r_{90} radius is indicated in red.

For larger incident angles optical aberrations lead to an increased degree of smearing and a decentralisation of the point spread function.
Among optical aberrations, the curvature of the field reduces the image quality by influencing the optimal distance between the lens and the focal plane. The distance decreases by increasing incident angles. This has to be taken into account for the optimisation of the lens design: The minimal aberration radius r_{90} for a fixed Fresnel lens diameter of $511\,\mathrm{mm}$ as a function of the number of grooves per millimetre is illustrated for different angles of incidence in figure 4.13.

Increasing the granularity of the lens improves the image quality due to a better description of the original parabolic curvature of the bulky lens. A good approximation is found for 2 grooves/mm as for a larger amount of grooves per mm no further improvement is ascertained. The r_{90} of the maximal θ_{in} limits the dimensions of the FAMOUS pixel (cf. chapter 4.2.2). The optimal design of the Fresnel lens is therefore determined:

$$
\begin{aligned}
f = D &\simeq 500\,\mathrm{mm} \\
k &= -1 \\
d_{\mathrm{thick}} &= 2.5\,\mathrm{mm} \\
\mathrm{granularity} &= 2\,\mathrm{grooves/mm}
\end{aligned}
$$

Comparison with Conventional Optical Designs

The profile of the Fresnel lens is modeled like a parabolic bulky lens. In figure 4.14 the sampled point spread function (PSF) for a Fresnel lens and a parabolic bulky lens is shown.

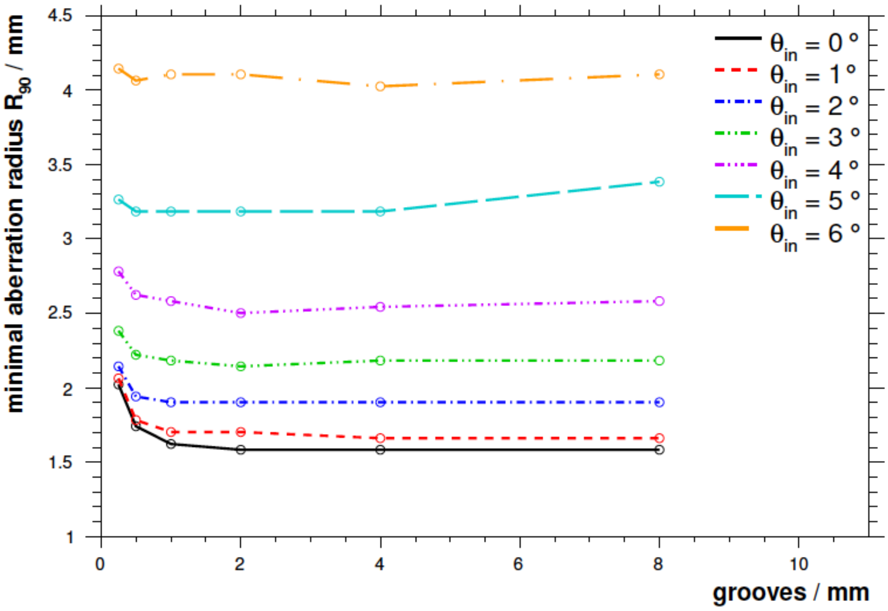

Figure 4.13: Optimisation of the Fresnel lens design using the aberration radius r_{90}. Diameter of the lens is fixed to roughly half a meter. Shown is the minimal achievable r_{90} radius for different incident angles as a function of the amount of grooves per millimetre. Taken from [82].

Both lenses have a diameter of 500 mm and are illuminated by photons with an incident angle of $\theta_{in} = 0\,°$. The PSF of the Fresnel lens is determined by a Geant4 simulation whereas the PSF of the bulky lens is calculated by ZEMAX [4], a commercial ray-tracing program.
Both lens types show a similar distribution with a high concentration of the photons in the very centre of the PSF surrounded by a homogeneous distribution up to a sharp ring.

The fraction of encircled energy is shown in figure 4.15 for different optical design each with an aperture diameter of 500 mm and a focal ratio of $N_f = 1$. A parabolic mirror shows an ideal image quality as the incoming light is focussed into a spot with a radius of several μm. For a refractive design the spot size is strongly increased and the image quality is in the order of several mm.

The image quality of a single lens suffers thereby on the small required focal ratio and on boundary surface effects as the light is deflected at two boundaries.
Comparing a conventional convex-planar parabolic lens to the corresponding Fresnel lens demonstrates an improved aberration radius for the Fresnel lens. The r_{90} radius of the bulky lens is approx. one order of magnitude larger. The increased aberration radius of the bulky lens may occur due to an increased thickness compared to the thickness of a Fresnel lens.

For the detection of the faint fluorescence light a very high transmission efficiency of the telescope is essential. Therefore, as much light as possible has to be included in one pixel and the r_{90} radius is chosen as image quality criterion for this analysis. This criterion is very strict and leads to relatively large pixel dimensions, thus a study of image quality criteria may be useful for future analyses to obtain the optimal criterion for the determination of the optical baseline design.

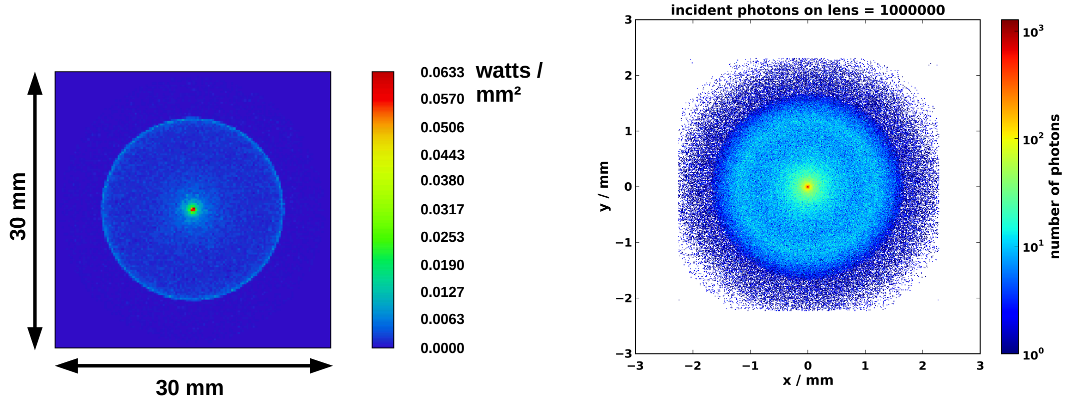

(a) parabolic bulky lens

(b) Fresnel lens

Figure 4.14: Simulated sampled point spread function for a Fresnel lens and a parabolic bulky lens, both with a diameter of $500\,\mathrm{mm}$. The incident angle on each lens is $\theta_{in} = 0\,°$.

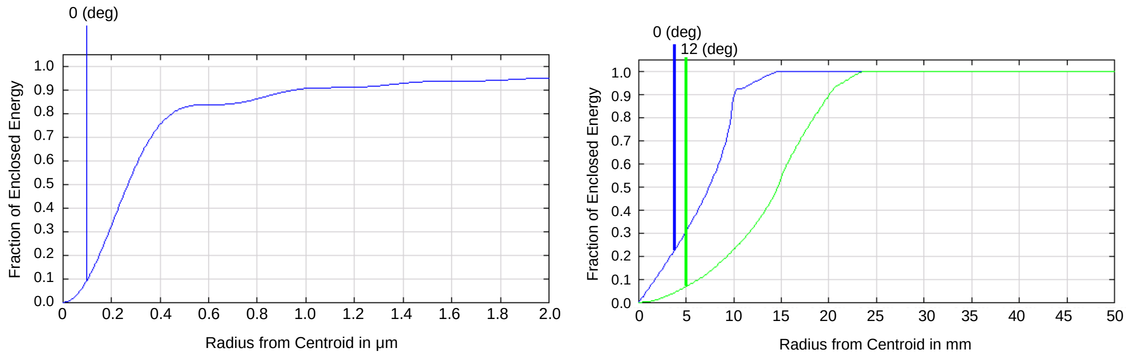

(a) parabolic mirror

(b) parabolic bulky lens

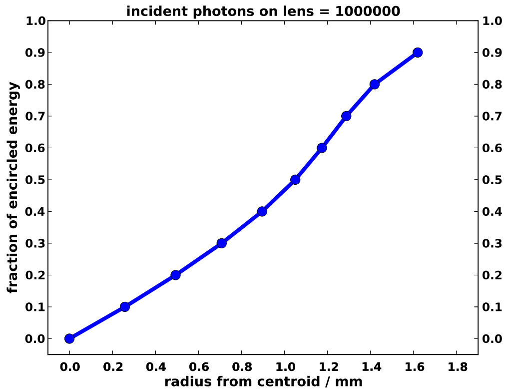

(c) Fresnel lens

Figure 4.15: The fraction of encircled energy as a function of the radius from the centroid of the photon distribution. Shown are simulations for a parabolic bulky lens, a Fresnel lens and a parabolic mirror, each with an aperture with a diameter of $500\,\mathrm{mm}$.

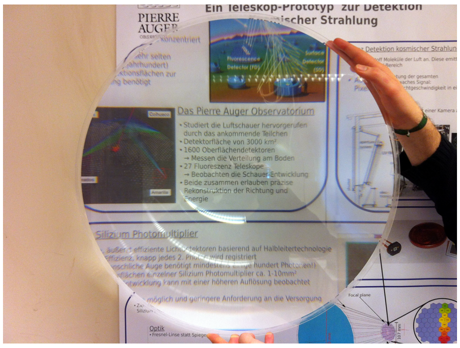

Figure 4.16: Photo of the chosen Reflexite Fresnel lens for the FAMOUS prototype [69]. Diameter and focal length are 502.1 mm.

The FAMOUS Fresnel Lens

As the simulation of a Fresnel lens shows a promising concentration power and a sufficient image quality, a suitable lens has been chosen.
A Fresnel lens of the Reflexite Corporation has been acquired (shown in figure 4.16). The lens has both diameter and focal length of 502.1 mm and is corrected for spherical aberrations (for a detailed description of lens SC943 see the data sheet in Appendix A 1).

Currently, the aberration radius of the chosen Fresnel lens for FAMOUS is investigated by Michael Eichler and an increased r_{90} radius is found as compared with simulations [44]. As for each configuration of a lens individual aspheric coefficients are required, the Geant4 simulations are based on a surface profile neglecting these coefficients. For an optimised determination of the image quality, the calculation of the chosen optimal baseline design may be improved by including the aspherical deformation.

Furthermore, the simulated groove profile of a Fresnel lens is idealised and does not include uncertainties introduced by the manufacturing process. The groove shape of the manufactured lens is also slightly modified for an easier production [41]. However, the simulated aberration radius is a good benchmark criterion to study a baseline design, but the measured aberration radius may be slightly larger.

4.2.2 Winston Cone

Light concentrators are used to collect as much light as possible and to guide it onto a light detection device. The incoming light with incident angles up to a maximum angle $\theta_{\max}$ is focused from a large aperture entry A onto a smaller area A'. This leads to an increased effective light collection area.
The crucial property of a light collector is its concentration ratio C defined as the ratio of the entry aperture radius r_1 to its exit aperture radius r_2 [84]:

$$C = \frac{r_1}{r_2} \tag{4.6}$$

For FAMOUS, Winston cones have been chosen as light collectors due to their theoretically high concentration power of

$$C_{\text{max}} = \frac{1}{\sin(\theta_{\text{max}})} \quad . \tag{4.7}$$

Focusing the photons onto a smaller area leads in accordance with Liouville's theorem to higher transverse momenta of the photons and a broadened angular distribution at the exit [58]. Thus, Winston cones are non-imaging devices. The influence of angles up to nearly 90° on the detection efficiency of SiPMs is studied in [39].

Construction of a Light Concentrator

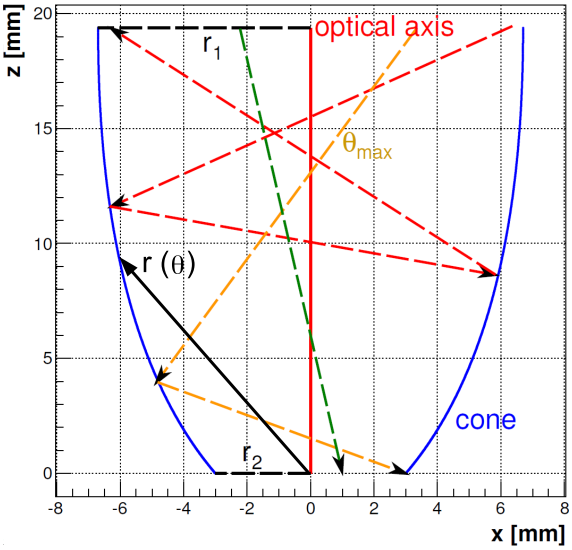

Figure 4.17: Schematic of a Winston cone. The parabolic shape of the cone $r(\theta)$ is tilted by the maximal angle θ_{max} leading to a focal point directly at the exit of the cone. The symmetrical axis of rotation is indicated in red. Light up to θ_{max} is guided directly (green) or by reflections (orange) through the exit of the cone. Other rays (red) are rejected [69].

A Winston cone is based on a reflective, parabolic inner surface. The shape can be described by

$$r(\theta) = \frac{1+\sin(\theta_{\text{max}})}{1-\cos(\theta+\theta_{\text{max}})} \cdot 2\,r_2 \tag{4.8}$$

whereby θ is the incident angle with respect to the optical axis, θ_{max} the maximal allowed angle and r_2 the radius of the output beam [55], [47].

The construction of a Winston cone is shown in figure 4.17. Light rays can traverse the concentrator directly or by reflections on the inner surface. Rays with an angle greater than θ_{max} are reflected back. The maximal allowed angle depends thereby only on the areas of the entrance and the exit of the Winston cone [87].

$$\sin(\theta_{\text{max}}) = \frac{r_2}{r_1} = \frac{1}{C_{\text{max}}} \tag{4.9}$$

$$\Rightarrow \theta_{\text{max}} = \arcsin\left(\frac{r_2}{r_1}\right) \tag{4.10}$$

The length of the Winston cone is determined by the other construction parameters [87]:

$$l = \frac{r_1 + r_2}{\tan(\theta_{\mathrm{max}})} \tag{4.11}$$

The FAMOUS Winston Cone

FAMOUS uses silicon photomultipliers for the detection of the faint fluorescence light. Installing Winston cones in front of the SiPMs increases the effective collection area. The material conditions for the successful use of the light funnel are a high transmission and an angle θ_{max} suitable for the baseline design to avoid loss of incoming light.

Polished aluminium meets the first condition by promising a high reflectivity and is used as material for the FAMOUS Winston cone. The influence of the stage of oxidation has been studied and a stable reflection efficiency $T \approx 70 - 95\,\%$ has been determined for different incident angles on the surface of $45\,°, 60\,°$and $75\,°$ [75]. Ray-tracing simulations (cf. figure 4.18) have led to an optimised design with a high transmission efficiency for the requested wavelength and angular range of FAMOUS. A circular entrance and exit aperture has been chosen for an inexpensive and fast construction in the workshops of the III. Physikalisches Institut, RWTH Aachen.

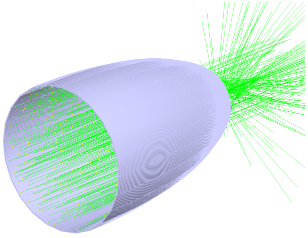

Figure 4.18: Visualisation of a ray-tracing simulation with Geant4 of a FAMOUS Winston cone. The parallel light beam is broadened by its focusing onto a smaller area. The simulation is based on the work of Tim Niggemann [82].

The FAMOUS light concentrators have an entrance radius of $r_1 = 6.71\,\mathrm{mm}$ and an exit radius $r_2 = 3\,\mathrm{mm}$ corresponding to the diameter of the SiPM and the focal plane design of FAMOUS.
The remaining parameters are deduced from equations (4.10) and (4.11):

$$\begin{aligned} r_1 &= 6.71\,\mathrm{mm} \\ r_2 &= 3.00\,\mathrm{mm} \\ l &= 19.6\,\mathrm{mm} \\ \theta_{\mathrm{max}} &= 26.6\,° \end{aligned}$$

To obtain the minimal spot size, the focal plane position is chosen at the entrance aperture of the Winston cones. For a convenient handling, all Winston cones are composed to a focal plane union as shown in figure 4.19.

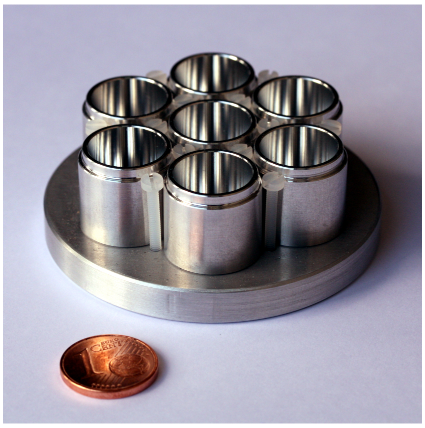

Figure 4.19: Focal plane union of FAMOUS consisting of seven hexagonally arranged Winston cones [69].

4.3 Detector Response Simulation

The optical design simulation of FAMOUS, based on the Geant4 framework, allows to study the response of the complete detector for the observation of extensive air showers. The crucial quality criterion is thereby the trigger probability of the SiPM camera depending on the energy and the distance of a shower.

The complete simulation chain comprises thereby three main parts summarised in figure 4.20.

Extensive air showers	Monte Carlo simulations allow to study the relation between characteristics of the primary particle of the cosmic ray, hadronic interaction models and parameters of EAS measurements. The simulation package CONEX [71] is a hybrid procedure combing an explicit Monte Carlo simulation for the first interactions and therefore most high-energetic part with a numerical parametrisation for the further development of the shower. The simulation of EAS by CONEX leads to a fast and very precise description of the shower quantities and the energy deposit. For the FAMOUS simulation, a library of proton induced, vertical air showers has been composed. It covers an energy regime of $E = \left[10^{15}\,\mathrm{eV}, 10^{21}\,\mathrm{eV}\right]$ splitted up into energy bins of $\log(\Delta E/\,\mathrm{eV}) = 0.25$, each consisting of 100 air showers. The chosen interaction model is EPOS [85], [72].
Fluorescence light	The energy deposit during the EAS development has to be translated to the emission of fluorescence light. The Auger Offline framework [20], [51] is used to calculate the total amount of fluorescence light by tracing the created photons from their origin to the aperture of the telescope. It contains a model of the atmosphere of the Earth, the fluorescence yield (see for more details chapter 3.1), the position of the telescope and the point of origin smeared by the lateral profile.
Detection of photons	Afterwards, the photons are tracked by Geant4 through all optical components of the telescope design. Reaching the camera, the photons have the chance to get detected by the SiPMs.

The decision, if an air shower is considered as detected, is based on the signal-to-noise ratio. Consequently, an important quantity is the amount of noise recorded by the telescope. It is dominated by noise phenomena of the SiPMs (confer chapter 4.1.2) and the night-sky brightness.

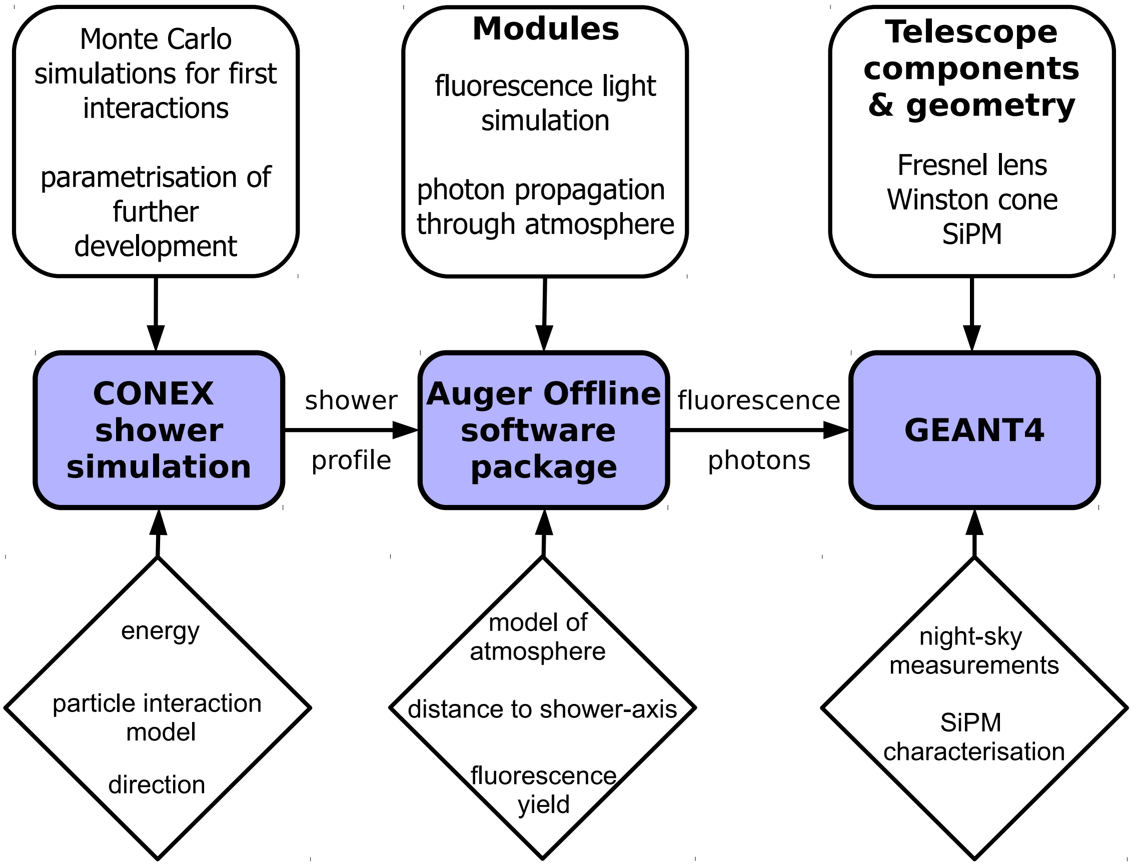

Figure 4.20: Concept of the detector response simulation of FAMOUS. The analysis chain comprises two parts: the simulation of extensive air showers by CONEX, the translation of the shower development into the total amount of fluorescence light by the Auger framework Offline and the detection of the photons simulated by Geant4. The upper boxes represent the used modules of the referring simulation package, the boxes below refer to the important parameters of the simulation. Adapted from [82].

4.3.1 Night-sky Background

The telescopes are based on the detection of light which is faint compared to the background of the night-sky brightness (NSB). The NSB is composed of mainly two parts including artificial light pollution and light from natural sources like stars and the moon. This leads to a continuous light flux reaching the aperture of the telescope. A large part of the light is absorbed by the UV pass filter of FAMOUS, but still the amount of background light is not negligible.

The photon flux expected in the Eifel, near Aachen, has been measured by a one-pixel-SiPM-telescope [73]. The experimental setup has been chosen to improve the understanding of SiPMs.

Observations of apparent dark regions in the sky and very bright and known stars have been performed. Measuring the flux of a known star allows a calibration of the setup, thereby the NSB or rather the amount of NSB photons, which FAMOUS will detect as tested in Aachen, can be determined.

Based on these data, a trigger can be implemented to distinguish between signal events and background, setting a lower boundary to the dynamic range of the telescope.

4.3.2 Trigger Probability

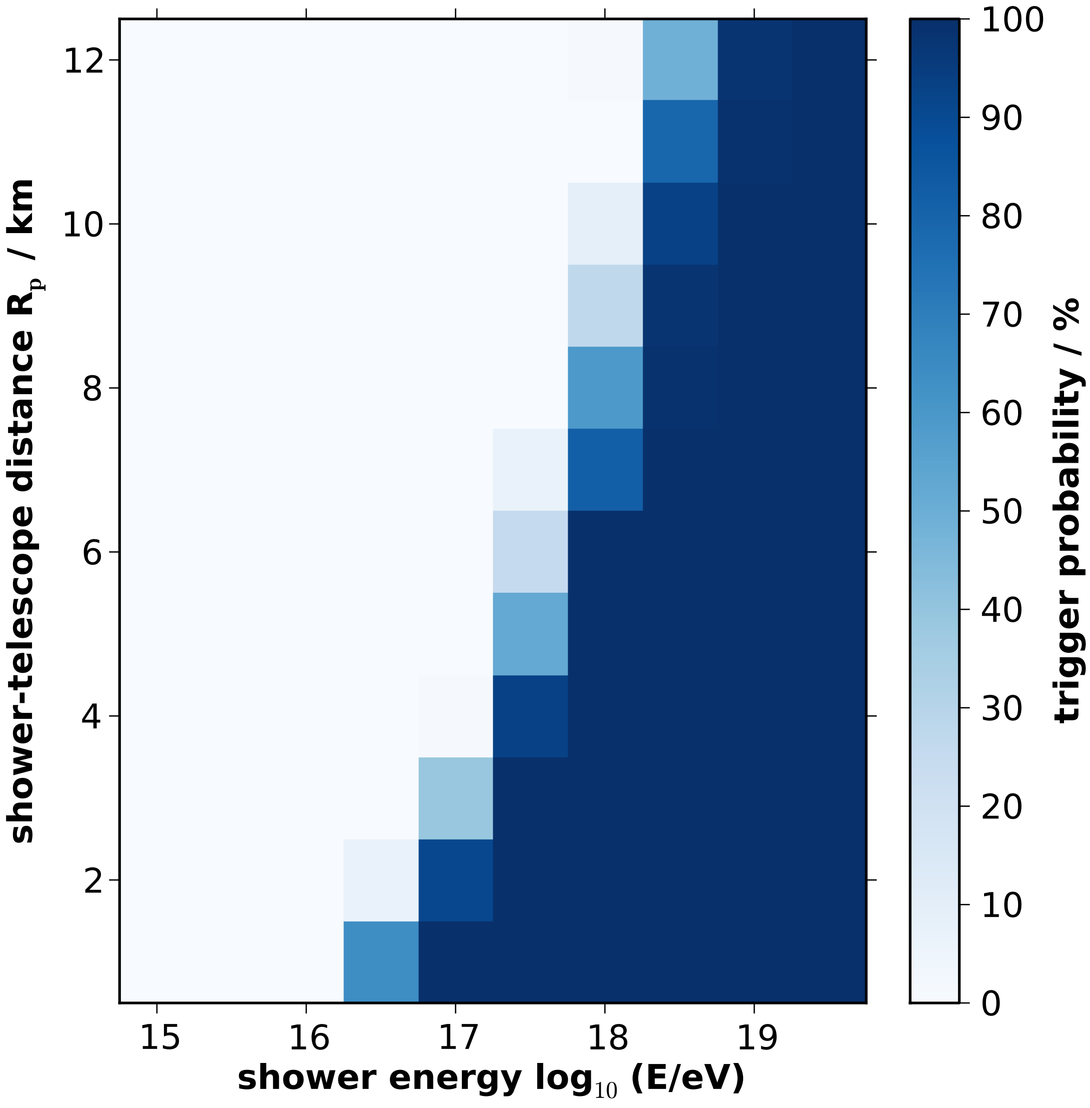

Figure 4.21: Expected trigger probability of the FAMOUS prototype as a function of the energy and the distance of vertical (zenith angle $\theta = 0\,°$) air showers according to simulations. An air shower is considered as detected if the signal exceeds a certain threshold. Taken from [82].

To study the performance of the detector within its application, the trigger probability as a function of the energy and the distance of the air shower can be simulated. The complete detector response is analysed for vertical showers (zenith angle $\theta = 0\,°$) with energies between 10^{17} eV and 10^{20} eV in a distance of 2 km. A shower is detected if the signal exceeds the noise by a certain threshold.

The simulated trigger probability is presented in figure 4.21. The FAMOUS prototype shows a promising capability to observe UHECRs. A $10^{17.5}$ eV shower can be detected at full efficiency up to a distance of $4 - 5$ km.

Furthermore, the amount of fluorescence photons reaching a circular aperture with a diameter of 500 mm is depicted in figure 4.22 for vertical showers with energies $E = [10^{17}\,\text{eV}, 10^{20}\,\text{eV}]$ for different distances R_p between telescope and shower. For low energy showers far away from the telescope, the amount of fluorescence photons reaching the aperture strongly decreases. The telescope aperture has to be increased to detect efficiently those showers.

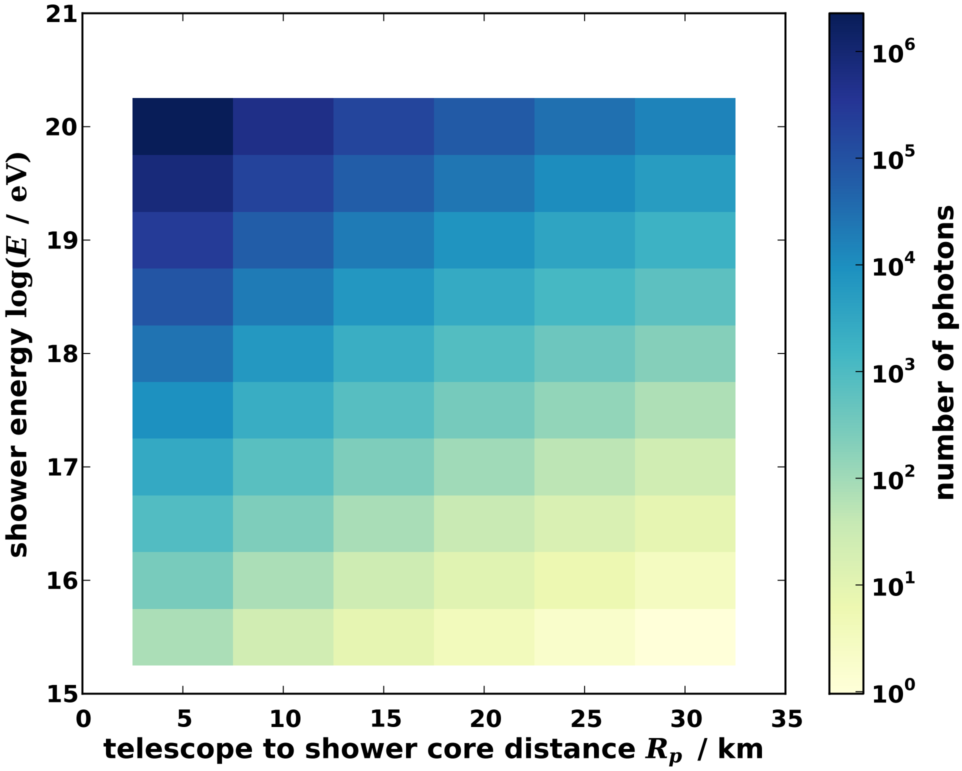

Figure 4.22: Expected amount of fluorescence photons reaching a telescope aperture with a diameter of 500 mm. The amount is simulated for different energies E and distances R_p of vertical ($\theta = 0\,°$) air showers.

4.4 First Measurements

The prototype is built and tested in a first seven pixel version (shown in figure 4.23). Currently, first measurements are performed in Aachen to validate the simulated performance, improve the understanding of all technical devices and determine the dynamic range of SiPMs. As soon as an even more dedicated read-out electronics can be installed, the camera will be extended to the designed 64 pixels.
The main target of FAMOUS will be the demonstration that the detection of extensive air showers is not only possible, but also improved by an SiPM camera.

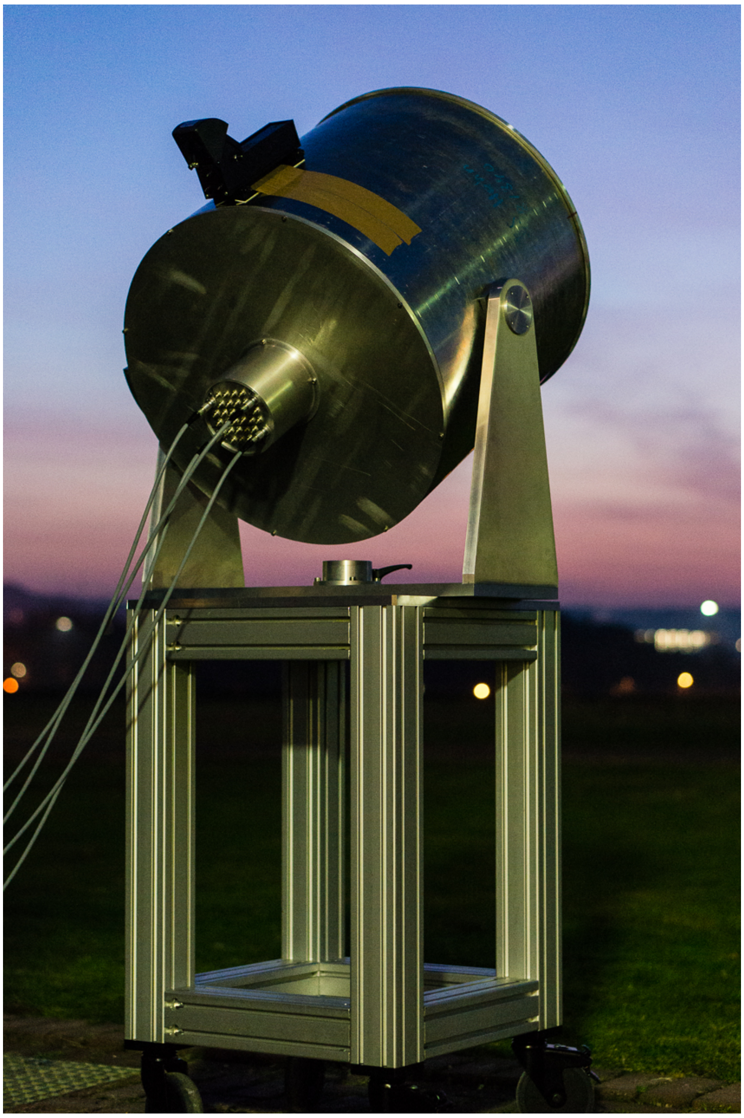

Figure 4.23: The FAMOUS prototype located in Aachen [69].

4.5 Concepts for a Large Exposure Telescope using a FAMOUS Camera

Fluorescence telescopes for the detection of EAS have to be able to detect faint fluorescence light produced in the atmosphere. Its statistics is strongly limited through their low duty cycle. Their sensitivity depends among other quantities on the overall photon detection efficiency, the aperture, the field of view and the signal-to-noise ratio. The next generation of detectors has to increase its trigger probability resulting into higher statistics. The use of silicon photomultipliers is a promising possibility to improve the detection of fluorescence light and to allow precise measurements of the shower development.
The low flux of cosmic rays at the highest energies requires large-exposure ground based experiments. In principle, a large exposure can be reached by a large area covered by large-aperture telescopes with a relatively large spacing, but also by an installation of many

small-aperture telescopes like FAMOUS into an array close together. The first principle is reviewed in this thesis as two different large exposure optical designs are investigated.

4.5.1 Large Aperture Concept

As state of the art, large-aperture reflecting telescopes are used to focus the light onto a photomultiplier camera.
In this thesis, two basic concepts are discussed:
On the one hand, the refractive optical design of the FAMOUS prototype with a large Fresnel lens is studied whereby a compact design without obstruction of the camera could be reached. On the other hand, the reflective optical Schmidt design successfully used in the fluorescence detector of the Pierre Auger Observatory is discussed (more details in chapter 3.2.1 and chapter 6).
Both designs have to be optimised for the detection of air showers by an SiPM camera. The crucial criterion is thereby a good image quality regarding the small dimensions of the FAMOUS pixels.

4.5.2 Small Aperture Concept

The novel idea of a ground-based experiment consisting of small-aperture telescopes is premised on the promising estimated performance of the FAMOUS prototype over a large energy regime (see chapter 4.3). The telescope is inexpensive, compact and mobile. Furthermore, each telescope can be operated in self-sustaining mode due to an expected low supply voltage. Despite these advantages, the best array layout for small telescopes has to be determined and the performance has to be compared to other detectors as the Pierre Auger Observatory.

Chapter 5

Refractive Baseline Design for a Large Aperture Concept

Motivated by the promising simulated performance of the FAMOUS telescope prototype as described in chapter 4, an optical design based on a refractive design with a Fresnel lens is studied. The small fluorescence light fluxes and the small dimensions of the silicon photomultipliers (SiPM) and thus of the focal plane, requires an optical system with a large aperture, a high transmission efficiency and a large field of view (FoV).

For this refractive design, the aperture is defined by the size of the Fresnel lens and the focal ratio $N_f = f_{\text{lens}}/D_{\text{lens}}$ has been fixed to 1 to allow a compact design and a large FoV. The free parameters of this study are thus the radius r of the lens and its granularity respectively the amount of grooves per mm n_{gr}. The Fresnel lens is modeled by the profile of a parabolic bulky lens.

5.1 Conic Fresnel Lens Groove Shape

As the Fresnel lens is a complex optical component, the study of its performance is performed by Geant4 simulations. The discontinuities in the Fresnel lens surface due to its subdivision into grooves influence the image quality. The aberration radius r_{90} is thereby used as the image quality criterion of the optical design as previously discussed in chapter 4.2.1.

Image Quality

The crucial part for an optimal performance of a fluorescence telescope using an SiPM camera is to concentrate the light sufficiently enough to ensure a high granularity and therefore a good angular resolution of the camera and an adequate noise rate of the SiPM unit.

The minimal possible aberration radius is thereby determined by the ray-tracing of photons with a corresponding wavelength of $\lambda = 350\,\text{nm}$ illuminating the whole lens for a certain incident angle θ_{in}. The wavelength of the monochromatic light is included in the fluorescence light regime.

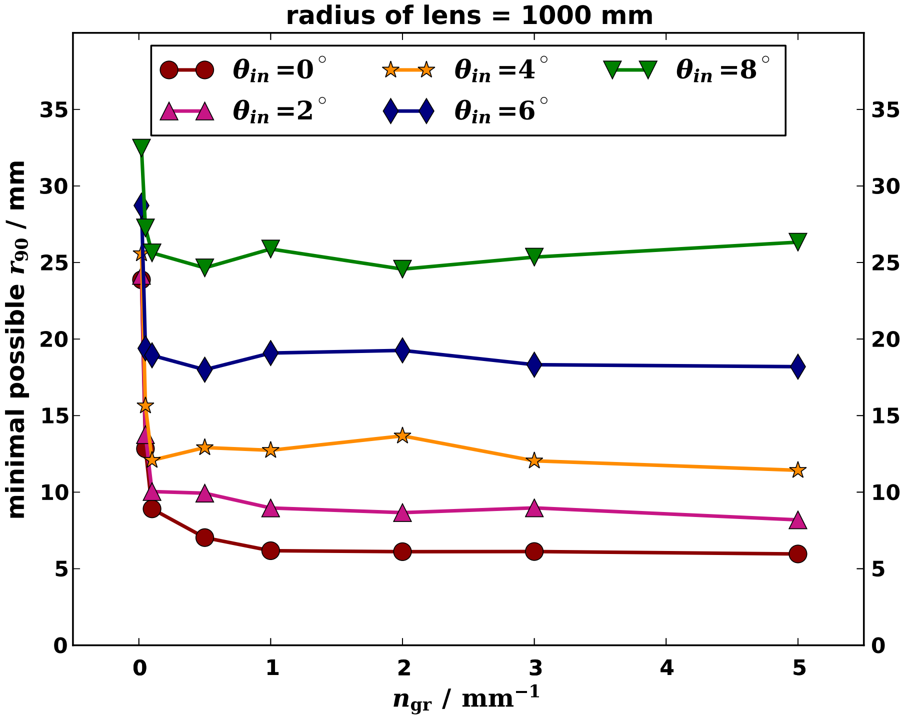

Figure 5.1: Optimisation of the Fresnel lens granularity by the aberration radius r_{90}. Shown is the minimal possible r_{90} for different incident angles with respect to the optical axis as a function of granularity n_{gr} respectively the number of conical shaped grooves per mm for a $2\,\mathrm{m}$ diameter lens.

The simulations for the FAMOUS prototype have been performed for a 511 mm diameter Fresnel lens whereby the shape of each groove is conical. The image quality improves for an increased number of grooves per mm n_{gr} (cf. figure 4.13) as for a larger granularity the shape of the original parabolic bulky lens is approximated more accurately.
The same behaviour is observed for Fresnel lenses with larger radii as shown exemplary in figure 5.1 for a 2000 mm diameter lens. Beyond a granularity of around 2 grooves per mm the image quality remains stable.

Although the focal length of the optical design is defined by the focal ratio as $f_{\mathrm{lens}} = D_{\mathrm{lens}}$, the optimal distance z_{best} between lens and focal plane is larger due to the imperfect imaging characteristics of the Fresnel lens. Also, the optimal distance decreases for higher incident angles on the Fresnel lens due to the effect of curvature of field as shown in figure 5.2. The optimal distance for each individual incident angle is thereby defined as

$$z_{\mathrm{best}} = f_{\mathrm{lens}} + dz_{\mathrm{best}} \qquad . \tag{5.1}$$

However, the lens has to be optimised for all incident angles and the determination of the optimal additional shift has to lead to a minimal r_{90} radius for all field angles. Therefore, for each lens configuration the focal plane is shifted along the optical axis to determine the best image quality. For each shift dz the simulation is performed once.

Two possible determinations of the minimal possible r_{90} radius for the complete lens have been performed as depicted in figure 5.2:

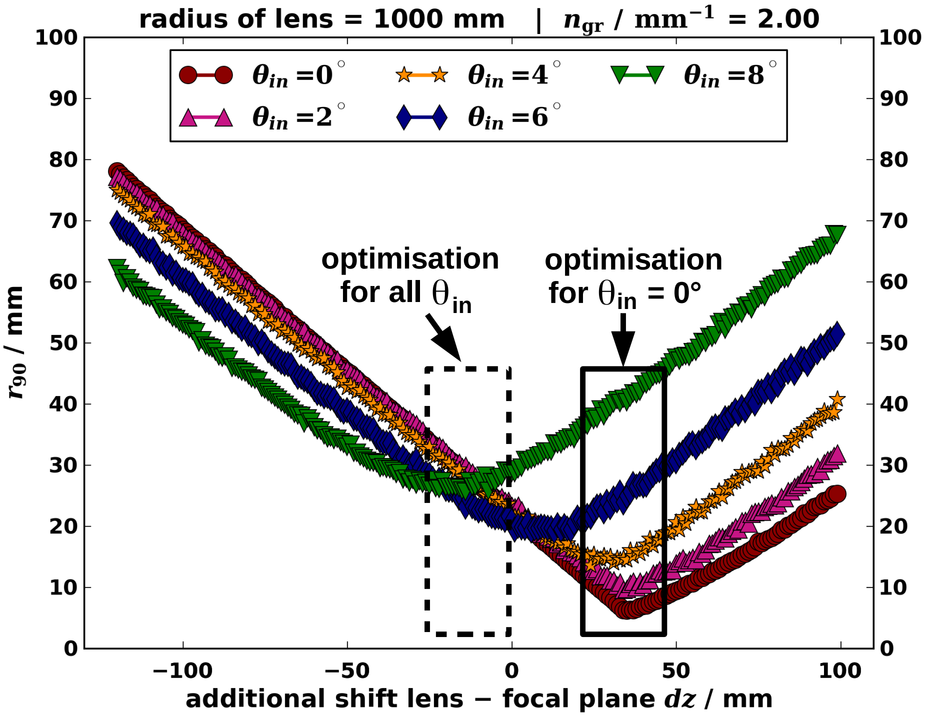

Figure 5.2: Determination of the optimal lens-focal-plane distance. Shown is the r_{90} radius as a function of the additional shift dz for different incident angles with respect to the optical axis as a function of lens radius. The lens granularity is fixed to 2 grooves per mm. Indicated with a dashed box is the shift $dz_{\theta_{\text{all}}}$ where the aberration radius coincides for all incident angles. The solid box refers to the shift dz_{θ_0} where the aberration radius is minimal for the incident angle of $0\,°$.

First, the shift dz_{θ_0} is defined by the minimal aberration radius of the incident angle $\theta_{in} = 0\,°$. For all further incident angles the aberration radius at the fixed shift is determined (cf. figure 5.2, solid box). This determination is designated as the optimisation for $\theta_{in} = 0\,°$ in the following. The image quality decreases strongly with increasing lens radius and incident angle as presented in figure 5.3.

Regarding the strong dependence on the incident angle, the optimal shift can alternatively be calculated by the distance between lens and focal plane $dz_{\theta_{\text{all}}}$ at which the aberration radius coincides for all incident angles (cf. figure 5.2, dashed box). The position of the shift $dz_{\theta_{\text{all}}}$ is thereby strongly influenced by the maximal field angle. A larger field of view of the telescope thus leads to an increased overall spot size.

The determination of $dz_{\theta_{\text{all}}}$ by requiring an aberration radius which coincides for all incident angles leads to an optimisation of the image quality for higher incident angles (cf. figure 5.4). However, increasing the radius of the lens by a factor of 2, still leads to the same increase of the r_{90} radius. Therefore, the aberration radius up to 50 mm exceeds strongly the small size of the Winston cone radius 6.71 mm as used for FAMOUS.

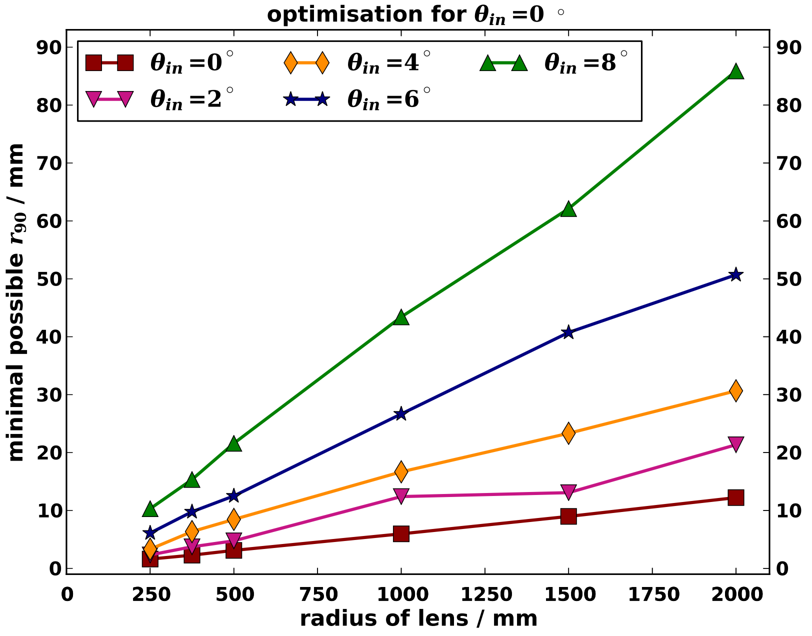

Figure 5.3: Optimisation for $\theta_{in} = 0\,°$ of the Fresnel lens design by the aberration radius r_{90}. Shown is the minimal possible r_{90} for different incident angles with respect to the optical axis as a function of lens radius. The lens granularity is fixed to 2 grooves per mm. The additional shift dz between lens and focal plane is fixed by the optimal shift at an incident angle of $\theta_{in} = 0\,°$.

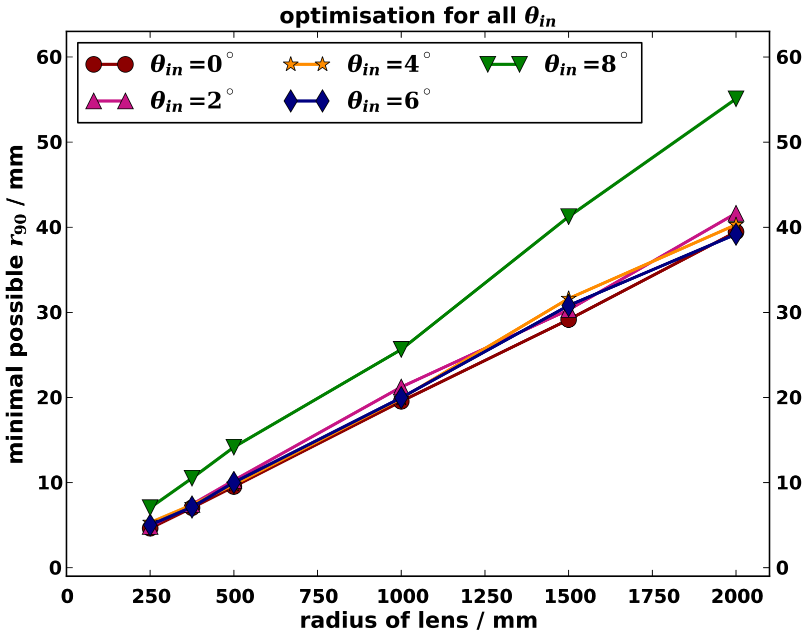

Figure 5.4: Optimisation for all θ_{in} of the Fresnel lens design by the aberration radius r_{90}. Shown is the minimal possible r_{90} for different incident angles with respect to the optical axis as a function of lens radius. The lens granularity is fixed to 2 grooves per mm. The additional shift $dz_{\theta_{\mathrm{all}}}$ between lens and focal plane is fixed by the shift where the r_{90} radius coincides for all incident angles.

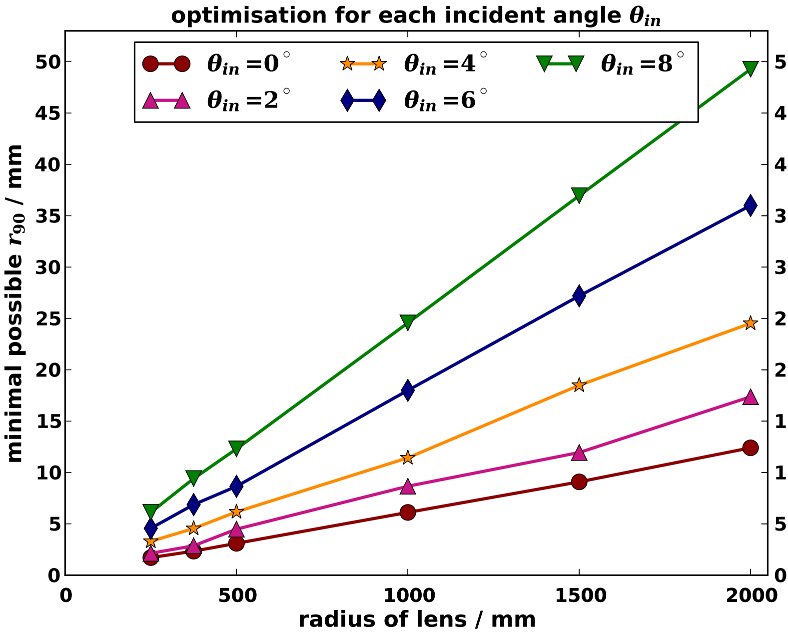

Figure 5.5: Correction of curvature of field. Shown is the minimal aberration radius r_{90} as a function of lens radius for different incident angles. The additional shift dz is individually determined for each incident angle θ_{in}. The granularity is fixed to 2 grooves per mm.

Correction of Curvature of Field

The effect of the curvature of field leads to a different optimal position of the focal plane for each incident angles to obtain a minimal possible r_{90}. As shown in figure 5.2, a change of the position in z direction up to 50 mm is needed for a 2 m diameter Fresnel lens. A correction of the effect is possible by applying a curved instead of a planar focal plane. For an optimal curvature of the focal plane, the fluorescence light will be focused for each incident angle θ_{in} onto the focal plane that the aberration radius becomes minimal.
As an estimation of the possible optimisation, the minimal aberration radius for each θ_{in} is shown as a function of the radius of the aperture 5.5. The image quality is in the same order of the image quality achieved by the optimisation for all incident angle 5.4. The aberration radius increases strongly with the size of the Fresnel lens:

$$r_{90}^{\mathrm{min}} \propto D_{\mathrm{lens}} \tag{5.2}$$

Angular Distribution

The size of the focal plane can be increased by using light concentrators as implemented at the FAMOUS prototype. As the minimal possible aberration radius r_{90} for Fresnel lenses with a radius larger than $r = 500\,\mathrm{mm}$ exceeds the entrance radius $r_1 = 6.71\,\mathrm{mm}$ of the FAMOUS Winston cone entrance (cf. chapter 4), the largest r_{90} radius calculated for all incident angles defines the new pixel size.
While Winston cones concentrate the incident light only up to a maximum angle θ_{max}, the angular acceptance on the focal plane is strongly limited and the angular distribution has

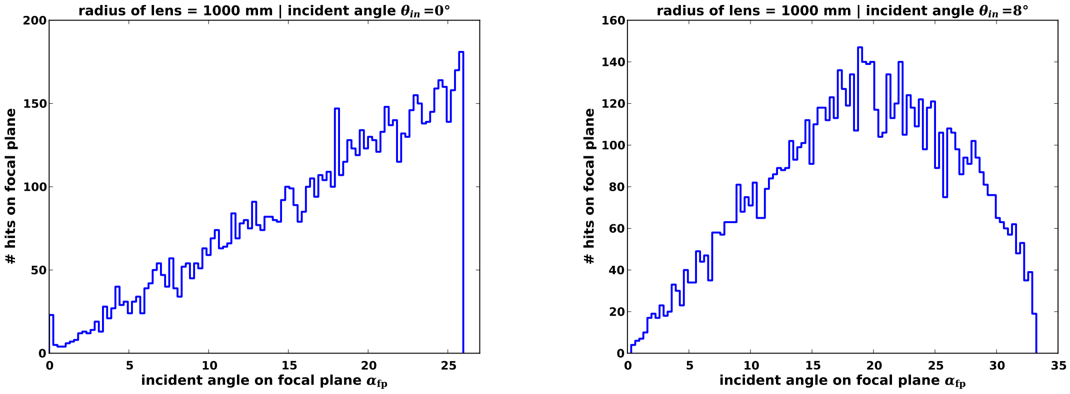

(a) incident angle $\theta_{in} = 0^\circ$ (b) incident angle $\theta_{in} = 8^\circ$

Figure 5.6: Angular distribution on the focal plane for a radius of lens = 1000 mm and 2 grooves per mm for different angles of light incident on the Fresnel lens.

to be analysed to determine the dimensions of the light concentrator as the exit radius r_2 of the Winston cone:

$$\theta_{\max} = \arcsin\left(\frac{r_2}{r_1}\right) \tag{5.3}$$

The angular distributions with respect to the optical axis on the focal plane are shown in figure 5.6. All rays incident on the focal plane within a circle with a radius $r = 2 \cdot r_{90}$ are considered. For larger incident angles the distribution broadens and the mean is shifted to the middle of the distribution.

The fluorescence light emitted from extensive air showers is very faint. Therefore, the overall transmission efficiency of the optical components is crucial and $\theta_{\max}$ accepted by the Winston cone is chosen as the maximal angle of the angular distribution on the focal plane. Thereby only rays incident on the focal plane within a circle with a radius of twice the r_{90} radius are considered.

The maximal angle slightly enlarges for higher granularity regarding small incident angles but becomes stable for all angles at 1 groove per mm (cf. figure 5.7).

The maximal angle as a function of the lens radius is depicted in figure 5.8. While increasing the incident angle on the lens, $\alpha_{\max}$ increases. For each incident angle on the aperture, the maximal incident angle on the focal plane is stable for all radii of the lens.

The minimal dimensions of the Winston cone of the refractive optical design with a Fresnel lens are determined by the spot size for an optimisation for all incident angles (cf. figure 5.4) referring to the Winston cone entrance radius r_1 and the angular distribution (cf. figure 5.8) defining the maximal allowed incident angle $\theta_{\max}$.

For each increase of the aperture of a factor of 2, the exit radius of the Winston cone has to be increased by a factor of 2 (cf. table 5.1). The exit aperture defines the size of the

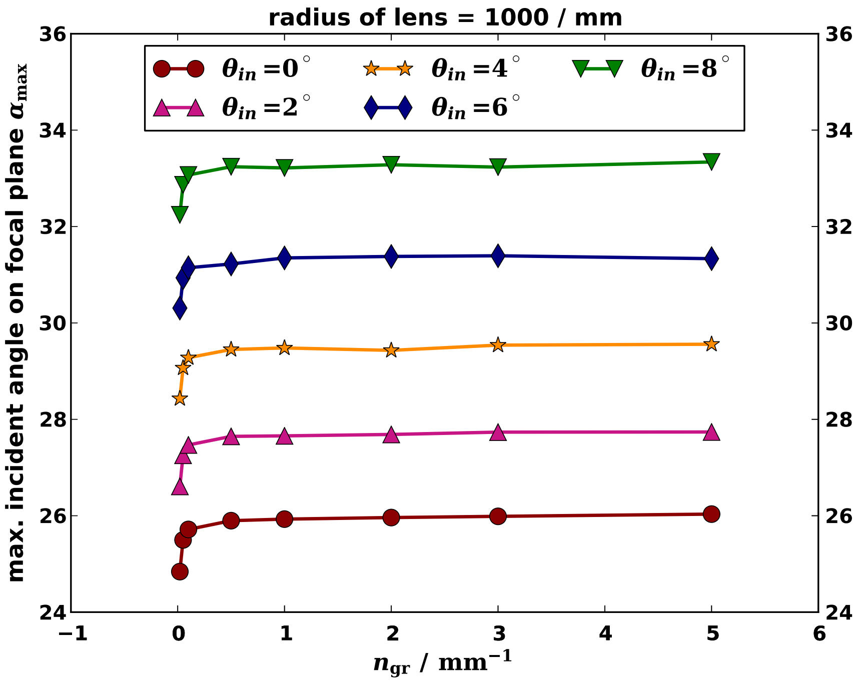

Figure 5.7: Maximum of the angular distribution of the light on the focal plane. Shown is the maximum angle $\alpha_{\max}$ for different incident angles θ_{in} on the $2\,\mathrm{m}$ diameter lens as a function of number of grooves n_{gr}.

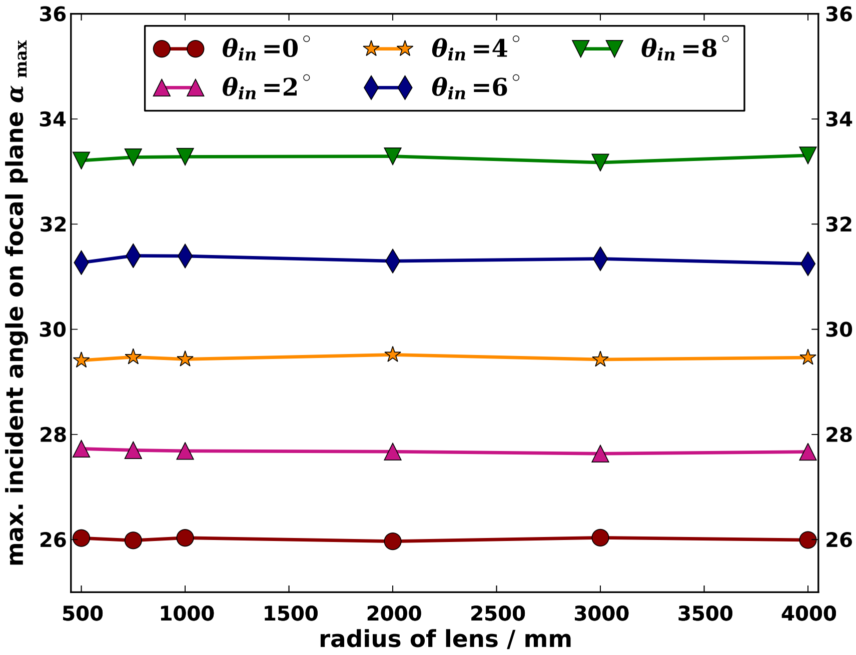

Figure 5.8: Maximum of the angular distribution of the light on the focal plane. Shown is the maximum angle $\alpha_{\max}$ for different incident angles θ_{in} on the lens as a function of the lens radius. The granularity is fixed to 2 grooves per mm.

radius of lens / mm	r_1 **/ mm** $\equiv r_{90}$ **/ mm**	$\theta_{\mathbf{max}}/^\circ$	r_2 **/ mm**
250	7.04	31.27	3.65
375	10.51	31.40	5.48
500	14.16	31.39	7.38
1000	25.63	31.30	13.32
1500	41.23	31.34	21.44
2000	55.08	31.25	28.57

Table 5.1: Dimensions of the Winston cone for different lens radii. The entrance radius r_1 is defined by the corresponding spot size and θ_{max} by the maximum angle of the angular distribution on the focal plane. The radius r_2 of the Winston cone exit aperture is determined according to equation (5.3).

SiPM unit. This leads to an insufficient performance of a refractive design with an SiPM camera for large scale Fresnel lenses.

Transmission

Besides the image quality, a high transmission efficiency of the optical system is required for an efficient detection of the faint fluorescence light. The transmission efficiency is defined by the ratio of the number of photons passing through the plate and the number of photons emitted from the source. The photons are detected on a focal plane with the same dimensions as the Fresnel lens.

As an increased number of grooves introduces more discontinuities on the lens surface, more reflections and scattering of the light can occur. Therefore, the transmission efficiency decreases for higher granularities as shown in figure 5.9 (left) for a 2 m diameter lens.

Although the light has to traverse more material for less grooves per mm and the transmission efficiency suffers from bulk absorption in the grooves, the reflectivity introduced by the grooves is the most crucial part.
This is studied by comparing the transmission efficiency with the efficiency of a Fresnel lens for which bulk absorption is neglected (cf. figure 5.9, right). For a small amount of grooves the transmission efficiency is improved. Therefore, an amount of 2 grooves per mm is preferred compromising between a good image quality and a high transmission efficiency.

The transmission efficiency for different radii of the Fresnel lens is nearly constant for a fixed granularity as depicted in figure 5.10.

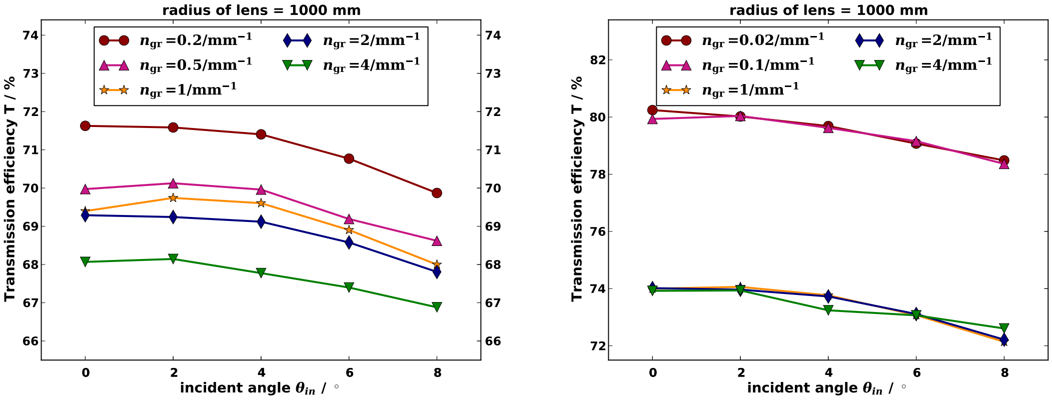

(a) including bulk absorption

(b) without bulk absorption

Figure 5.9: Transmission efficiency of the Fresnel lens as a function of the incident angle. Shown is the transmission efficiency for a different amount of grooves per mm.

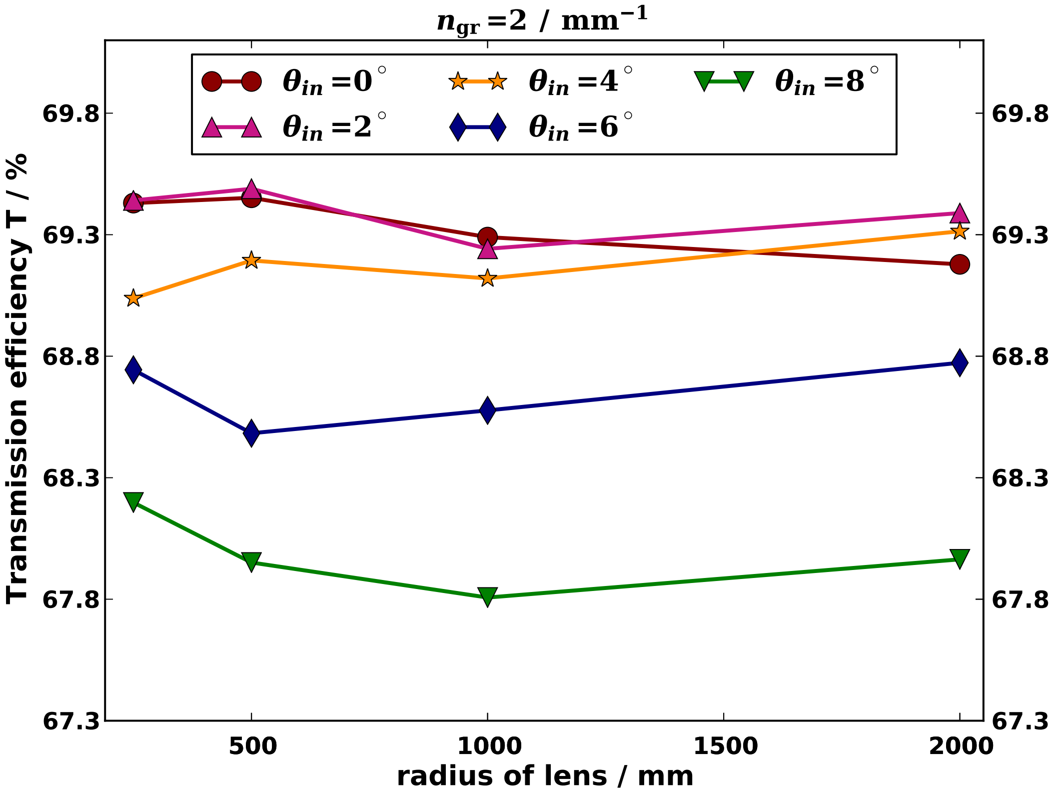

Figure 5.10: Transmission efficiency of the Fresnel lens as a function of the radius of the lens. Shown is the transmission efficiency for different incident angles. Bulk absorption is respected.

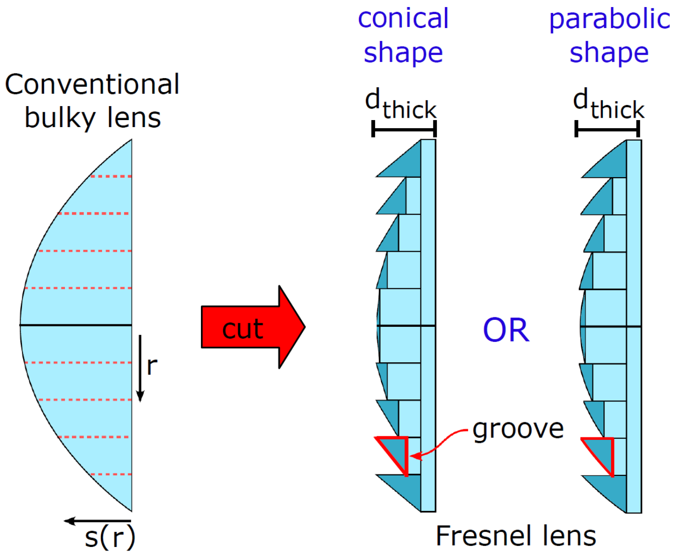

Figure 5.11: Illustration of the construction principle of a Fresnel lens. A conventional parabolic lens is divided into grooves which are located onto a common base plate. The contour of the bulky lens is preserved for parabolical shaped grooves and approximated for conical shaped grooves.

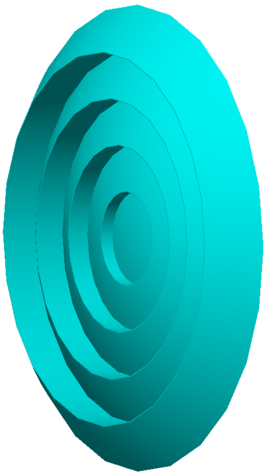

Figure 5.12: Geant4 simulation of a Fresnel lens where the contour of the groove is shaped like the curved surface of the original bulky lens.

5.2 Parabolic Fresnel Lens Groove Shape

An optical design using lenses with high refraction power suffers from spherical and chromatic aberration. The UV pass filter narrows the spectral bandwidth of the incident light. Winston cones are nonimaging optical components. In combination, the influence of chromatic aberration is of minor significance.
Spherical aberration can be reduced by modeling the Fresnel lens on an aspheric lens type. In this study the Fresnel lens is constructed according to a parabolic bulky lens. So far, the grooves for the Fresnel lens have been simulated as conical instead of parabolic shaped since this is a good approximation for a sufficiently large amount of grooves per mm and reduces computing time.

The influence of the groove curvature has been studied in more detail in this section by obtaining the contour of the curved surface of the corresponding part of the original bulky lens. A sketch of Fresnel lenses with parabolic and conical shaped grooves modeled by the profile of a parabolic bulky lens is depicted in figure 5.11. Also a Geant4 simulation of the lens with parabolic shaped grooves is shown in figure 5.12.

Image Quality

The image quality may be improved for a small number of grooves due to the better description of the original curved surface of the lens. For a large amount of grooves per mm the image quality converges for parabolic and conical grooves as assumed. Already for 0.5 grooves per mm the aberration radii coincide for a Fresnel lens radius of 250 mm (cf. figure 5.13). For both lens radii statistical fluctuations are observed. The number

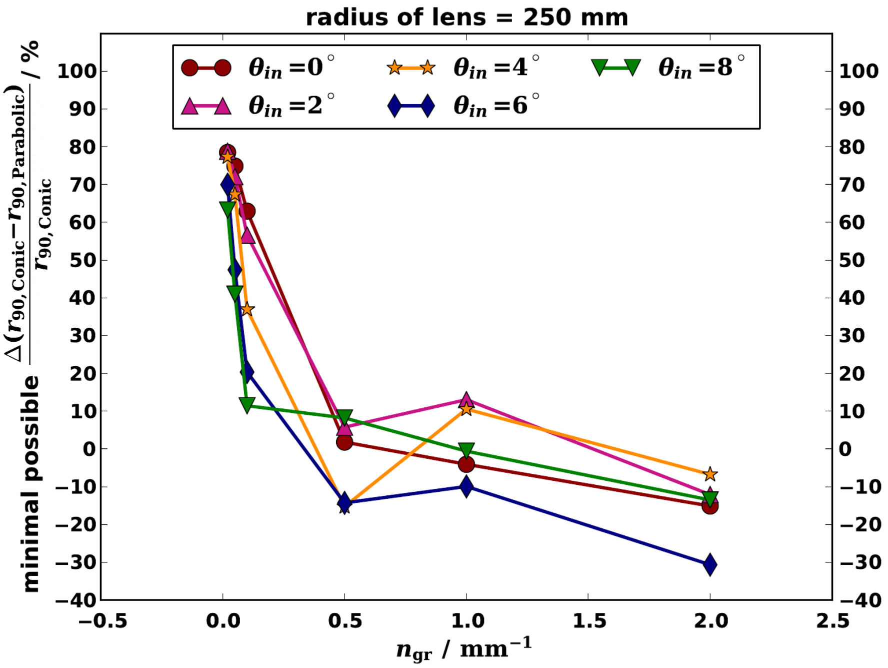

(a) radius of the lens = 250 mm

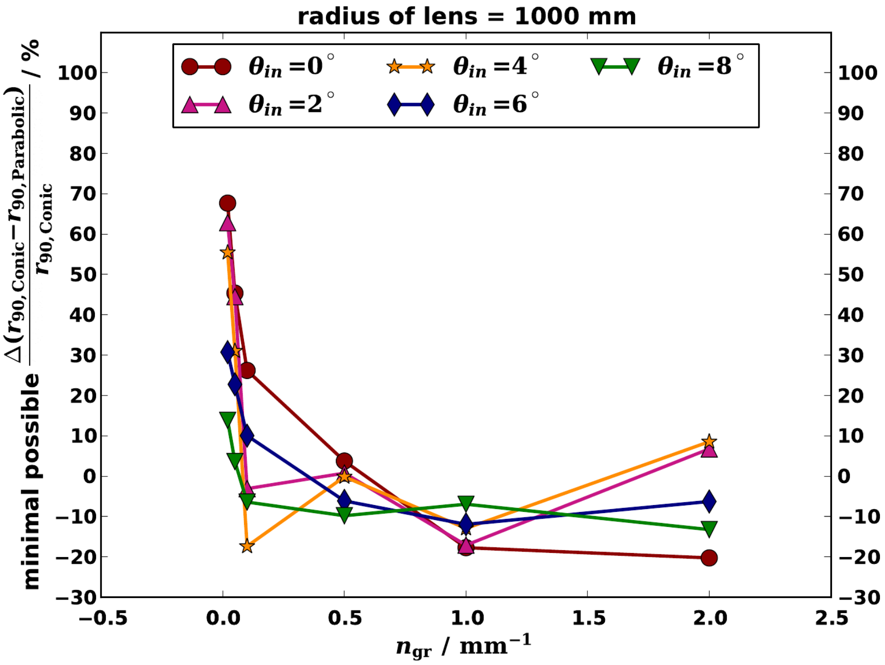

(b) radius of the lens = 1000 mm

Figure 5.13: Optimisation of the Fresnel lens granularity by the aberration radius r_{90}. Shown is the difference from the minimal possible r_{90} radius for conical shaped grooves to the aberration radius for parabolic shaped grooves. The difference is shown for different incident angles with respect to the optical axis as a function of the granularity, respectively the number of grooves per mm.

of photons per simulation is limited for computational reasons. As the general tendency of no significant improvement for the application of parabolic curved grooves is obtained, further simulations have been renounced.

The minimal possible aberration radius r_{90} for larger Fresnel lens radii slightly differs from the determined image quality of a Fresnel lens consisting of conical shaped grooves. The relative difference between both groove shapes is calculated for two optimisations: The optimisation for $\theta_{in} = 0\,^{\circ}$ of the r_{90} radius with a lens-to-focal-plane distance fixed by the optimal distance for an incident angle $\theta_{in} = 0\,^{\circ}$ is shown in the upper part of figure 5.14. As a comparison, the optimisation for all θ_{in} fixed by the distance where the aberration radius coincides for all incident angles is depicted in the lower plot. Thereby, positive values refer to an improved aberration radius for parabolic shaped grooves.

For both methods, the minimal aberration radii slightly decrease for high granularities by the application of conical shaped grooves. Therefore, the overall spot size is not improved by the application of parabolic grooves.

Transmission

The transmission efficiency of a parabolic lens is also slightly decreased in comparison to the Fresnel lens with conical shaped grooves as depicted in figure 5.15. Furthermore, the efficiency is less stable for different radii, especially for small incident angles.

Angular Distribution

Regarding the angular acceptance of the Winston cone, the angular distribution on the focal plane is investigated. All rays incident on the focal plane within a circle with a radius $r = 2 \cdot r_{90}$ are considered. The maximal angle of the distribution defines the maximal allowed incident angle accepted by the light concentrator. Implementing a Fresnel lens with parabolic grooves does not influence the angular acceptance of a Winston cone as shown in figure 5.16.

As the image quality, the transmission efficiency and the angular distribution for a Fresnel lens are not improved by the preservation of the curved surface of the original bulky lens, the application of conical grooves is a good approximation for a sufficiently large number of grooves per mm leading to a simplified construction of the Fresnel lens.

5.3 Correction for Displacement of Grooves

For a perfect continuous lens, the optimal lens-to-focal-plane distance z_{best} corresponds to the focal length of the lens f_{lens}. As already mentioned, for a Fresnel lens an additional shift is needed to achieve the minimal possible r_{90} radius.
The effect is introduced by the subdivision of the continuous lens into grooves. As a Fresnel lens is constructed based on a model of a conventional parabolic bulky lens, each groove

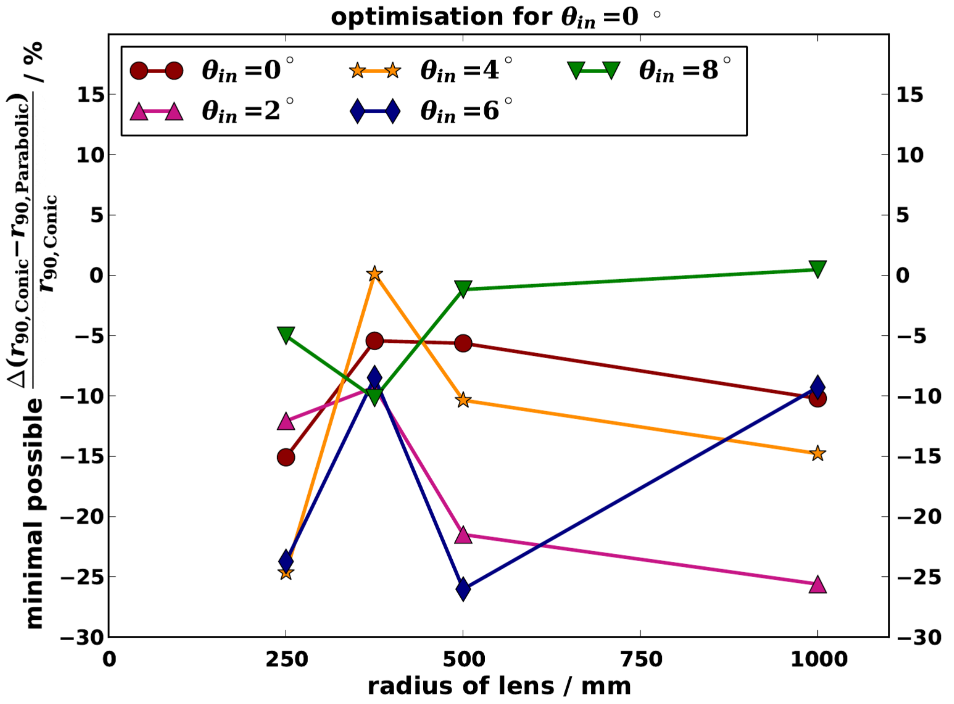

(a) The additional shift dz_{θ_0} between lens and focal plane is fixed by the optimal shift at an incident angle of $\theta_{in} = 0\,^\circ$.

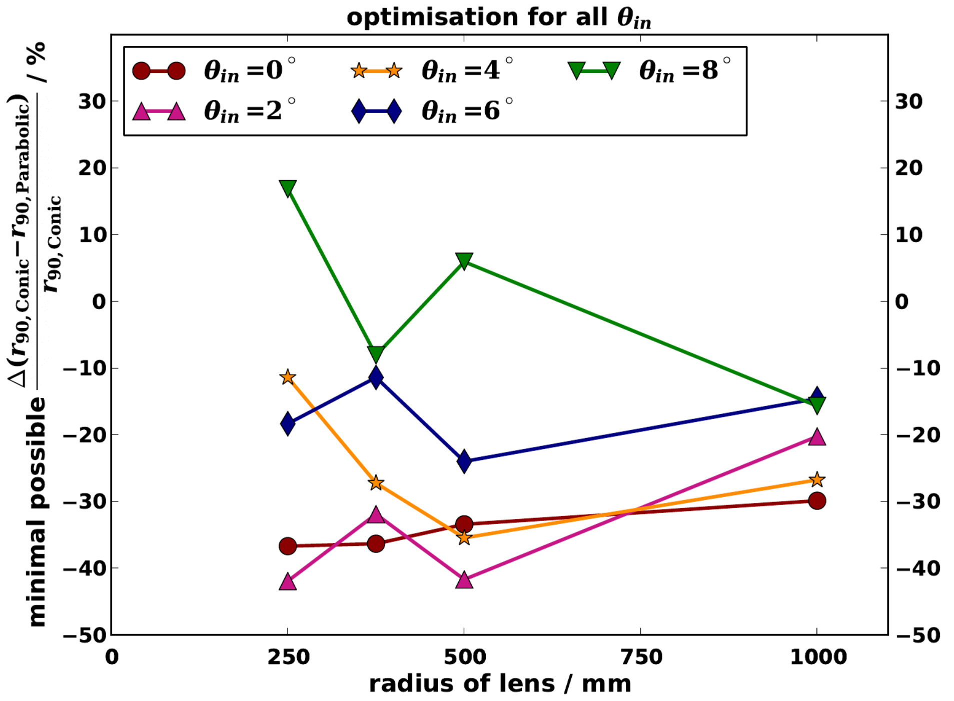

(b) The additional shift $dz_{\theta_{\mathrm{all}}}$ between lens and focal plane is fixed by the shift where the r_{90} radius becomes coincided for all incident angles.

Figure 5.14: Comparison of the image quality of conical and parabolic grooves. Shown is the minimal possible r_{90} for different incident angles with respect to the optical axis as a function of the lens radius. The lens granularity is fixed to 2 grooves per mm.

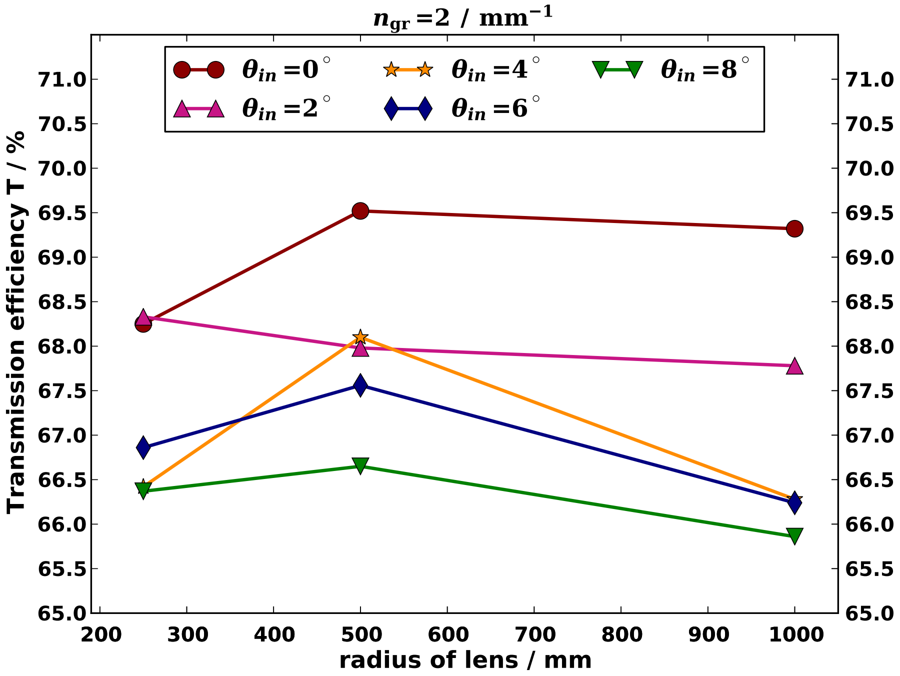

Figure 5.15: Transmission efficiency of the Fresnel lens as a function of the radius of the lens. Shown is the transmission efficiency for different incident angles of a lens with parabolic shaped grooves. Bulk absorption is respected.

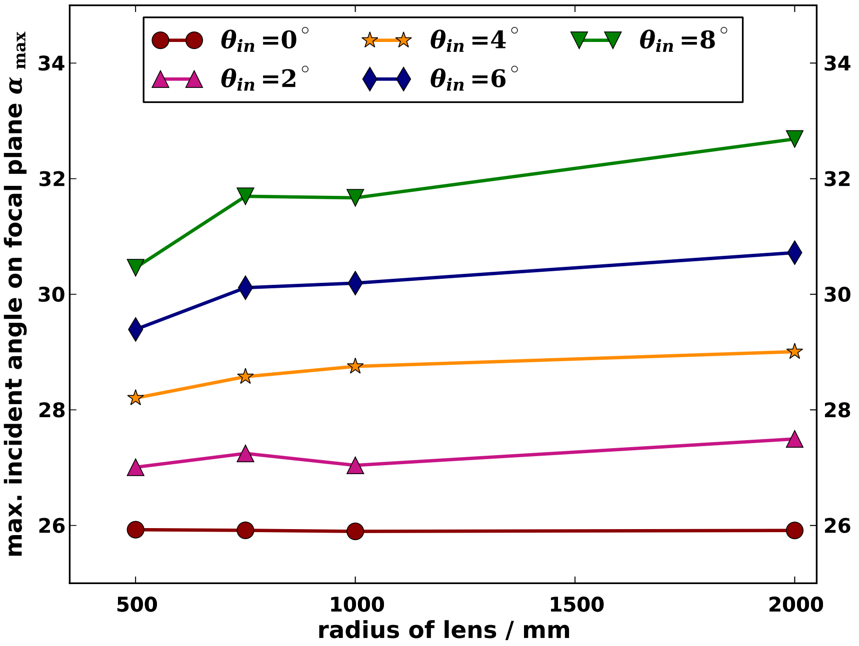

Figure 5.16: Maximum of the angular distribution of the light on the focal plane. Shown is the maximum angle α_{max} for different incident angles θ_{in} on the lens as a function of the lens radius. The granularity is fixed to 2 grooves per mm and the grooves have a parabolic curvature.

of the Fresnel lens is calculated depending on the size, the shape and focal length of the model.

However, approximating a bulky lens by a Fresnel lens influences the imaging characteristics and the path of the light rays as shown in figure 5.17. On the one hand, all grooves are translated onto a common base plate, thus a light ray enters the groove material at a different position along the optical axis compared to the original bulky lens. On the other hand, the light ray has to traverse less material. For each groove of a Fresnel lens, the displacement and the amount of traversed material differ. This may lead to an individual optimal distance between an individual groove and the focal plane.

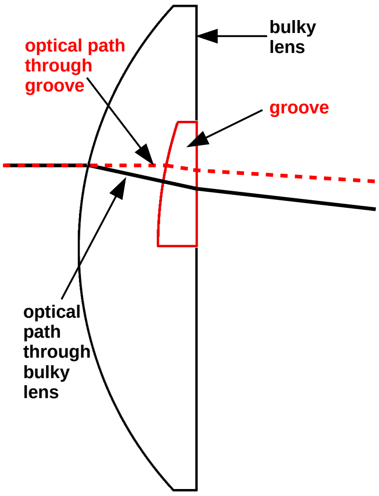

Figure 5.17: Path of the light ray is changed due to an approximation of the bulky lens by a Fresnel lens leading to a displacement of the groove onto a common base plate.

As for a specific Fresnel lens a fixed shift between the lens and the focal plane has to be chosen, a difference of the optimal distance for each groove and the focal plane would lead to a blurring of the image and thus to an increased aberration radius. Taking these effect into account may improve the image quality.

In the following analysis, the influence of the individual imaging characteristics of each groove will be studied in more detail.

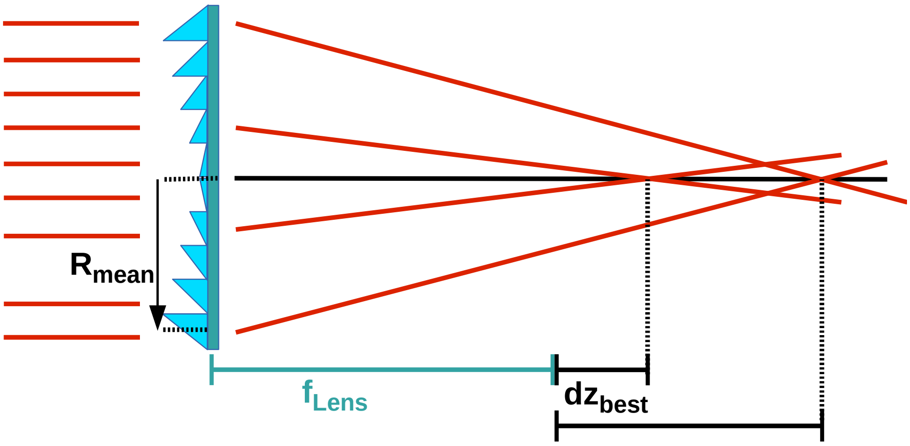

Figure 5.18: Sketch of a Fresnel lens. Shown is the optimal distance between each groove and the focal plane composed of the focal length f_{lens} and the optimal shift dz_{best}. The radial position of the groove is defined by the the mean position of the groove R_{mean}.

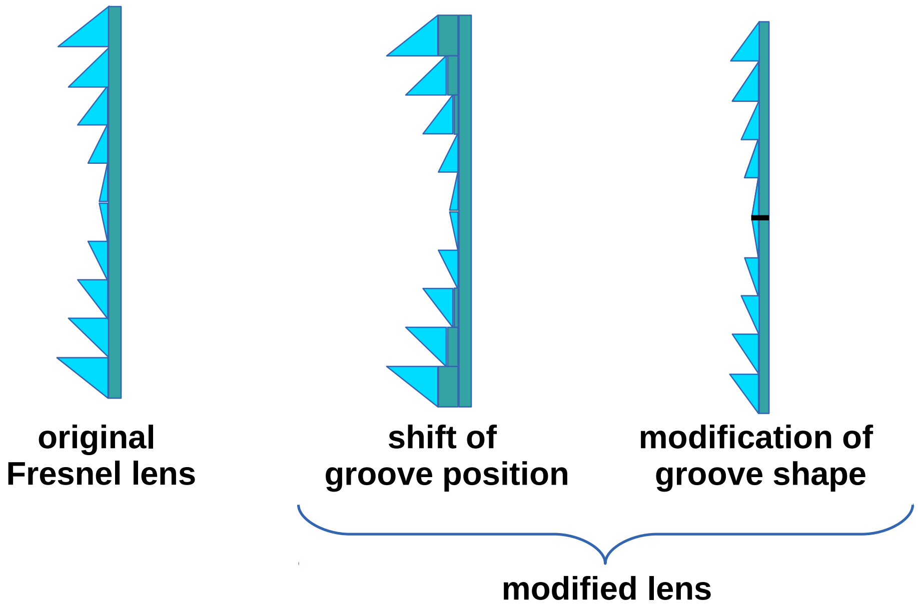

Figure 5.19: Sketch of two general methods for the application of an optimal groove-to-focal-plane distance. Shown is the original Fresnel lens compared to the modified lenses. The lens can be modified by the shift of the grooves along the optical axis or by applying a changed focal length to each groove which leads to a modified groove shape.

Determination of optimal distance

The optimal distance between a groove and the focal plane is calculated by the explicit illumination of each individual groove followed by the determination of the minimal r_{90} radius and the corresponding shift dz_{best} additionally needed to the focal length f_{lens}. Repeated for all grooves of a lens, a general functional relation between the mean radial position of the groove R_{mean}, the granularity n_{gr} and the shift dz may be found allowing to optimise the image quality for each configuration of a lens. The definition of the important parameters is illustrated in figure 5.18. The grooves are illuminated by light with an incident angle of $\theta_{in} = 0\,^{\circ}$ as a first estimation of the possible optimisation of the image quality. The radius of the lens is fixed.

Application of optimal distance

An optimal distance $z_{\text{best}} = f_{\text{lens}} + dz_{\text{best}}$ should be the same for each groove for an improved sharpness of the image. There are two general methods to obtain an optimal distance for each groove. The position of the grooves along the optical axis dz can be changed while keeping the shape of the grooves. However, all grooves together have to be connected as a continuous stable lens with a common base plate. For a relatively large needed shift, this would require additional material between the shifted groove and the common base plate. More material would lead to more absorption in the lens. Restricted by this requirement, the application of an optimisation of the shape of each groove may be preferred as the shape of the groove depends on the focal length. Both applications are sketched in figure 5.19.

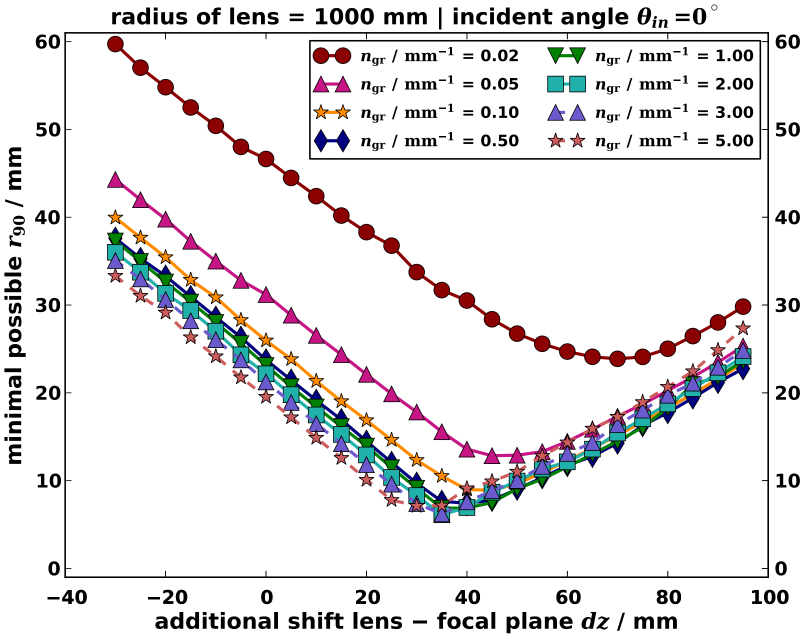

Figure 5.20: Shown is the r_{90} distribution as a function of the shift dz for different degrees of granularity. Simulations are based on a $2\,\mathrm{m}$ diameter lens with conical grooves illuminated by photons with an incident angle of $\theta_i = 0\,°$ with respect to the optical axis.

5.3.1 Determination of the Optimal Groove-to-Focal-Plane Distance

As the optimal distance dz_{best} is the crucial parameter in this study, its relation to other parameters of the optical design has to be investigated in the first instance.

The diameter of the lens is fixed to $2\,\mathrm{m}$ as a compromise between a large aperture and a decent aberration radius of the Fresnel lens. The only free parameter left is thus the granularity of the lens.

The study is performed for a small amount of grooves per mm, since changes between grooves become more distinct and can be studied in more detail. As shown in the previous section, a parabolic curvature of the grooves for this regime of grooves per mm n_{gr} results in smaller aberration radii. Therefore, each simulation is performed by illuminating the individual parabolic shaped groove by monochromatic light with a wavelength of $\lambda = 350\,\mathrm{nm}$.
As the area of the grooves increases for an outer radial position of the groove and decreases for a higher granularity, the density of optical photons incident on the groove is kept constant by adjusting the number of simulated photons for the corresponding illuminated area.

The r_{90} distribution as a function of the shift dz for an increasing amount of grooves per mm is shown for the illumination of a whole $2\,\mathrm{m}$ diameter lens (cf. figure 5.20). For less grooves/mm the distribution of the r_{90} as a function of the shift dz broadens. Therefore, statistical fluctuations may influence the accuracy to determine the minimum of the distribution defining the optimal shift dz for the studied regime of grooves per mm.

Method for the Determination of the Optimal Groove-to-Focal-Plane Distance

For the determination of the minimum of the distribution and its corresponding shift dz, the determination of the minimum by a parabolic fit on the simulated data is investigated.

To allow a stable determination of the minimum position, a fit on the data of a smaller region around the minimum is performed. Therefore, the position of the minimum dz_{rough} has been roughly calculated by simulations with a large step size over a wide range of dz. Around the minimum a smaller step size is needed to accurately determine the optimal distance.

The choice of the step size and the analysis window has to comprise an efficient analysis as well as the needed calculation power and time. Therefore, a simulation sample is analysed for the central groove of a 2 m diameter lens with $n_{\text{gr}} = 0.01\,\text{grooves/mm}$ (cf. figure 5.21) and the outermost groove for a lens granularity of $n_{\text{gr}} = 0.1\,\text{grooves/mm}$ to determine the optimal simulation parameters. Thereby, for each shift dz one simulation is performed:
In 0.05 mm steps the lens is additionally shifted for $dz = [0\,\text{mm}, 100\,\text{mm}]$ with respect to f_{lens}. The optimal shift dz_{best} has been calculated for different analysis windows and step sizes by fitting a parabolic function and calculating the position of the vertex. For comparison, the position defined by the shift dz corresponding to the minimal value of the calculated aberration radii is depicted.

The optimal analysis window for both grooves is found for $dz = [dz_{\text{rough}} - 10\,\text{mm},\ dz_{\text{rough}} + 10\,\text{mm}]$. The step size 0.25 mm is chosen as the minimum is adequately described and the amount of simulations is reduced. This analysis window and this step size are applied for all further simulations.

In general, the simulation of one specific groove and each shift dz is performed once to reduce computational power and time. Studying statistical fluctuations, the simulation of each configuration is repeated hundred times to estimate the uncertainties of a single simulation.

For the statistical test, the central groove of a 2 m diameter lens with $n_{\text{gr}} = 0.01\,\text{grooves/mm}$ is chosen as well as the outermost groove of a lens with $n_{\text{gr}} = 0.1\,\text{grooves/mm}$.

For each discrete shift between groove and focal plane the mean value and the uncertainty on the mean value of the corresponding r_{90} radius has been calculated. Taking the difference in the illuminated area into account, the central groove is analysed by ray-tracing simulations of 10000 photons, while the outermost groove is illuminated by 20000 photons. The statistical fluctuations are depicted for the central groove in figure 5.22. The spread of the aberration radius can lead to a misidentification of the minimum of the distribution. The maximal uncertainty on the mean of the r_{90} radius is thereby determined as:

$$\sigma_{r_{90},\,\text{central groove}} = 0.003\,\text{mm} \quad , \quad \sigma_{r_{90},\,\text{outermost groove}} = 0.134\,\text{mm} \tag{5.4}$$

As an estimation of the uncertainties on the optimal shift dz_{best} introduced by the fit the spread of the calculated dz_{best} is determined. Therefore, the r_{90} radius is simulated hundred times as a function of dz. For each distribution the optimal shift is calculated

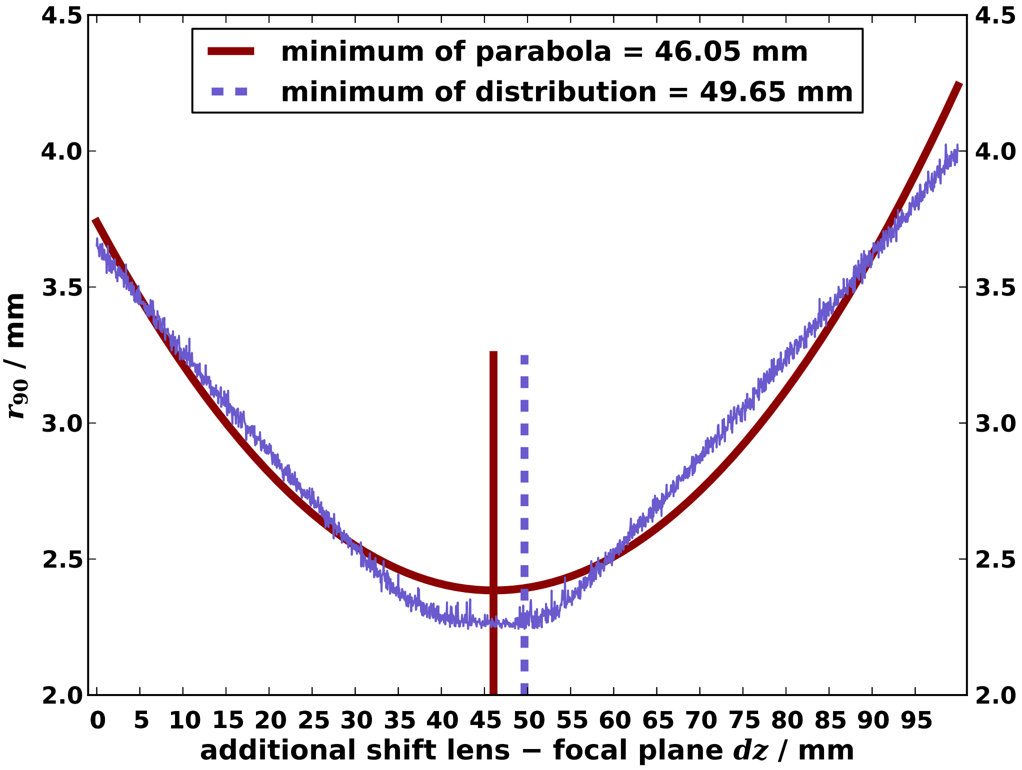

(a) $dz = [0\,\mathrm{mm},\ 100\,\mathrm{mm}]$, step size $= 0.05\,\mathrm{mm}$

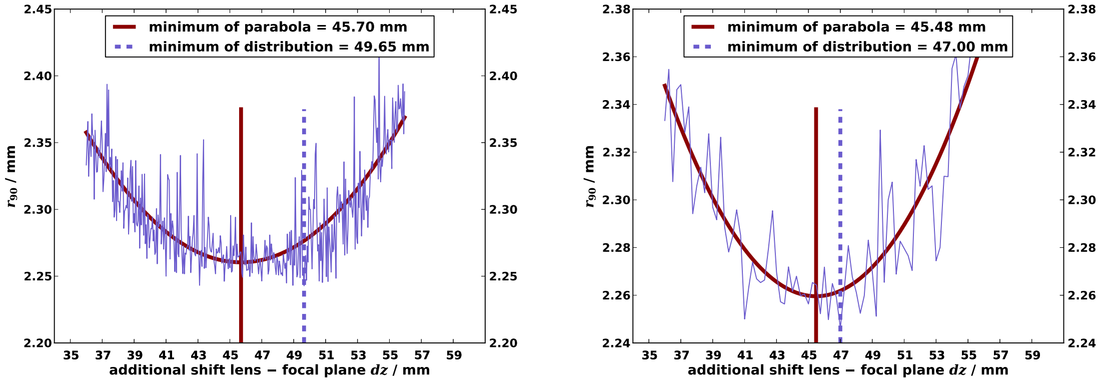

(b) $dz = [dz_{\mathrm{rough}} - 10\,\mathrm{mm}, dz_{\mathrm{rough}} + 10\,\mathrm{mm}]$, step size $= 0.05\,\mathrm{mm}$

(c) $dz = [dz_{\mathrm{rough}} - 10\,\mathrm{mm}, dz_{\mathrm{rough}} + 10\,\mathrm{mm}]$, step size $= 0.25\,\mathrm{mm}$

Figure 5.21: Simulation of the central groove to obtain the optimal analysis window and step size for a parabolic fit on the data. The lens diameter is fixed to $2\,\mathrm{m}$, the granularity to $0.01\,\mathrm{grooves/mm}$. Shown are different analysis windows and step sizes. For each window the position of the minimum is indicated by a vertical line. The minimum is determined by the corresponding shift of the minimal calculated r_{90} radius indicated by the purple line as well as by the position of the vertex of the fitted parabola indicated by the red line.

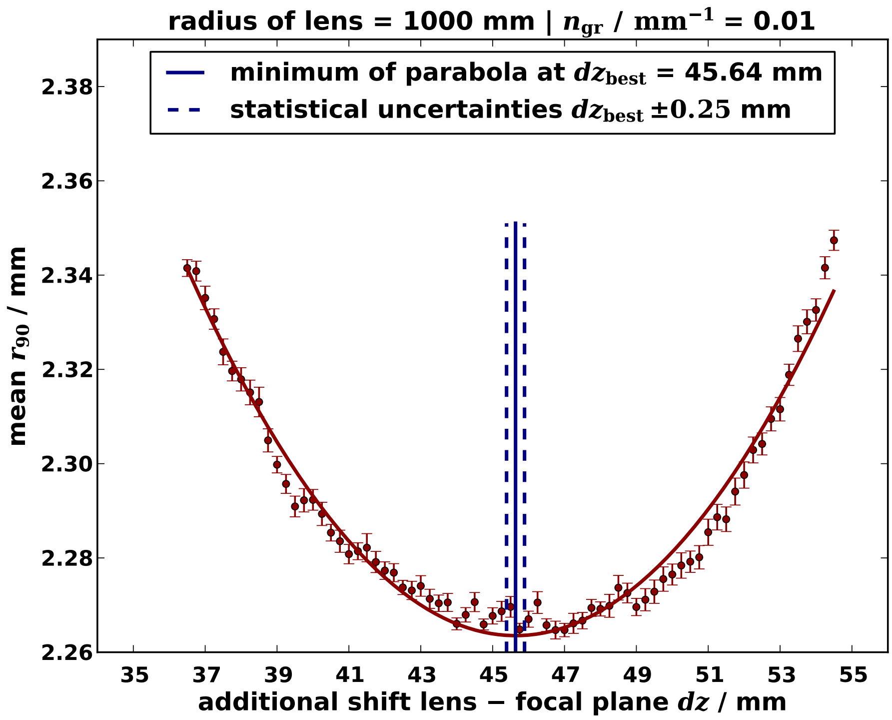

Figure 5.22: Statistical fluctuations of the r_{90} radius for an incident angle of $\theta_i = 0\,°$. The radius of the lens is fixed to $1000\,\mathrm{mm}$. Shown is the distribution for the central groove for a granularity $n_{\mathrm{gr}} = 0.01\,\mathrm{grooves/mm}$. Depicted is the optimal additional shift dz_{best} including statistical uncertainties. The aberration radius is determined for 100 simulations each including 10000 tracked optical photons.

on the one hand corresponding to the overall minimal simulated aberration radius, on the other hand corresponding to the vertex of the parabolic fit.

The distribution of the optimal shift for the latter (cf. figures 5.23 and 5.24, right) demonstrates a more stable determination of the minimum position. The fit of a parabola is therefore preferred for the determination of the minimum of the distribution.
The uncertainty on the root mean square of the distribution defines the uncertainty on the optimal shift. Grooves far away from the optical axis are more influenced by statistical fluctuations leading to a wider spread of the optimal distance as shown in figure 5.24. As a conservative estimate the uncertainty on the determination of the optimal distance dz_{best} is determined as

$$\sigma_{dz_{\mathrm{best}}} = 0.25\,\mathrm{mm} \qquad . \tag{5.5}$$

The study of influence of statistical fluctuations on the position of the optimal shift dz_{best} is summarised in figure 5.25.

Study of the Optimal Groove-to-Focal-Plane Distance

Based on the study of the influence of statistical fluctuations the optimal groove-to-focal-plane distance is determined by a parabolic fit for each groove of a 2 m diameter Fresnel lens for an incident angle of $\theta_{in} = 0\,°$. For different granularities of the lens, the optimal

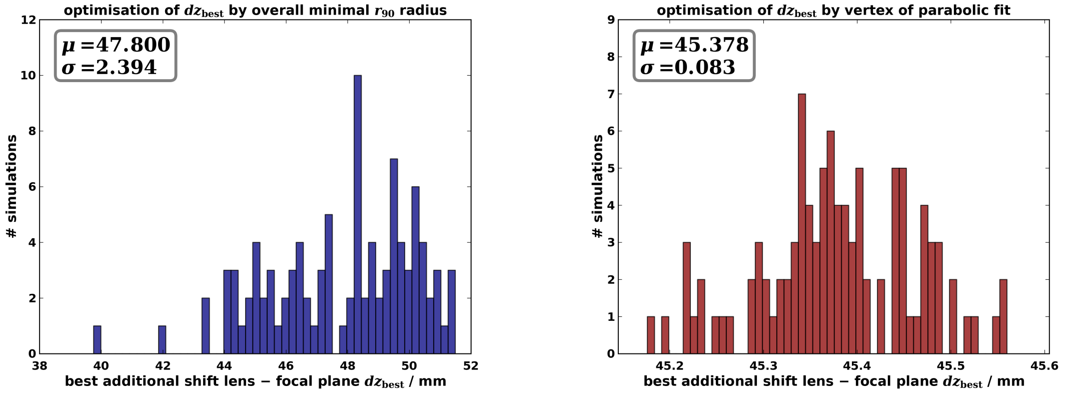

(a) corresponding shift dz_{best} for minimal r_{90} radius (b) dz_{best} defined by the vertex of a parabola

Figure 5.23: Histogram of dz_{best} for 100 simulations of the central groove of a $2\,\text{m}$ diameter lens with $n_{\text{gr}} = 0.01\,\text{grooves/mm}$. Compared are the calculation of the optimal distance by the minimal aberration radius and the fit of a parabolic function.

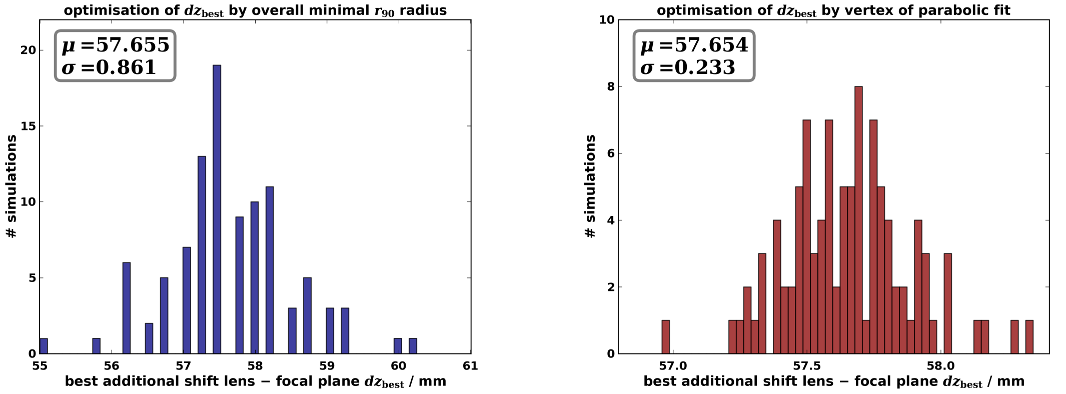

(a) corresponding shift dz_{best} for minimal r_{90} radius (b) dz_{best} defined by the vertex of a parabola

Figure 5.24: Histogram of dz_{best} for 100 simulations of the outermost groove of a $2\,\text{m}$ diameter lens with $n_{\text{gr}} = 0.1\,\text{grooves/mm}$. Compared are the calculation of the optimal distance by the minimal aberration radius and the fit of a parabolic function.

shift dz_{best} as a function of the mean radial position R_{mean} of the groove is depicted in figure 5.26.
A parabolic fit on the data describes the basic shape of data, whereby for each data point an uncertainty of $0.25\,\text{mm}$ is assumed as estimated in the previous section (cf. figure 5.24).

For a larger amount of grooves per mm the optimal shift dz_{best} decreases leading to an approach of the optimal distance z_{best} to the focal length of the original bulky lens as depicted for the parabolic fit in figure 5.27.

It is searched for a parametrisation of the functional relation between the optimal shift and the radial grooves position of a lens. The parabolic fits allows to relate the optimal distance not only sufficiently to the mean radial position of the groove R_{mean} but also to

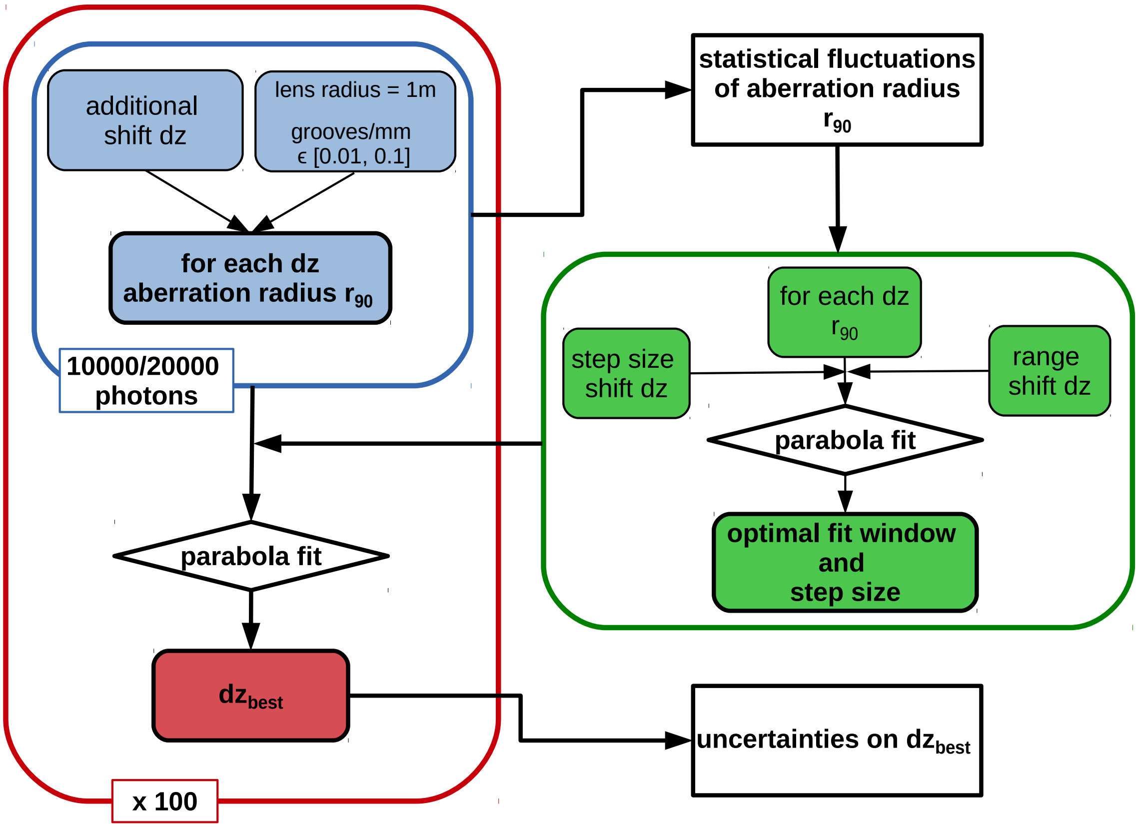

Figure 5.25: Sketch of the study of uncertainties on the optimal distance dz_{best} and the determination of the best analysis window and step size for the fit of a parabolic function. The aberration radius r_{90} is calculated for different shifts dz. The simulation of the distribution of the same groove is redone 100 times. For each simulation the position of the minimum is calculated by the fit of a parabolic function whereby an analysis for the optimal fit window and the step size has been performed by single simulations. By the spread of the distribution of the optimal shift dz_{best} the uncertainty of the calculation is estimated.

the granularity n_{gr} of the lens. Therefore, the parabolic fit is chosen for the further analysis and the parametrisation can be then described by the following equation:

$$dz_{\text{best}}\left(n_{\text{gr}}, R_{\text{mean}}\right) = a\left(n_{\text{gr}}\right) + b\left(n_{\text{gr}}\right) \cdot R_{\text{mean}} + c\left(n_{\text{gr}}\right) \cdot R_{\text{mean}}^2 \tag{5.6}$$

The fit on the parameters of the parabolic fit is shown in figure 5.28. For all parameters an exponential relation to the granularity n_{gr} can be found.

An implementation of the parametrisation for the optimal groove-focal-plane distance as according to equation (5.6) may result into an improvement of the image quality for a modified lens. A displacement of each groove along the optical axis by the corresponding needed shift dz_{best} would require a large additional amount of material between the shifted groove and the common base plate to obtain a stable modified Fresnel lens. As the material would change the light path and would lead to a decreased transmission efficiency, this method is renounced.

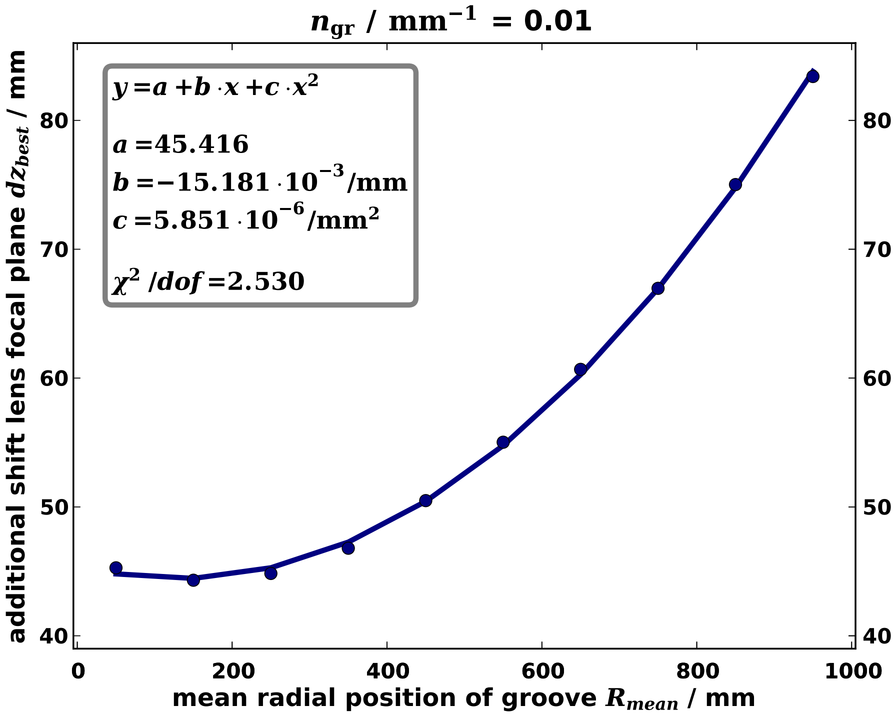

(a) 0.01 grooves/mm

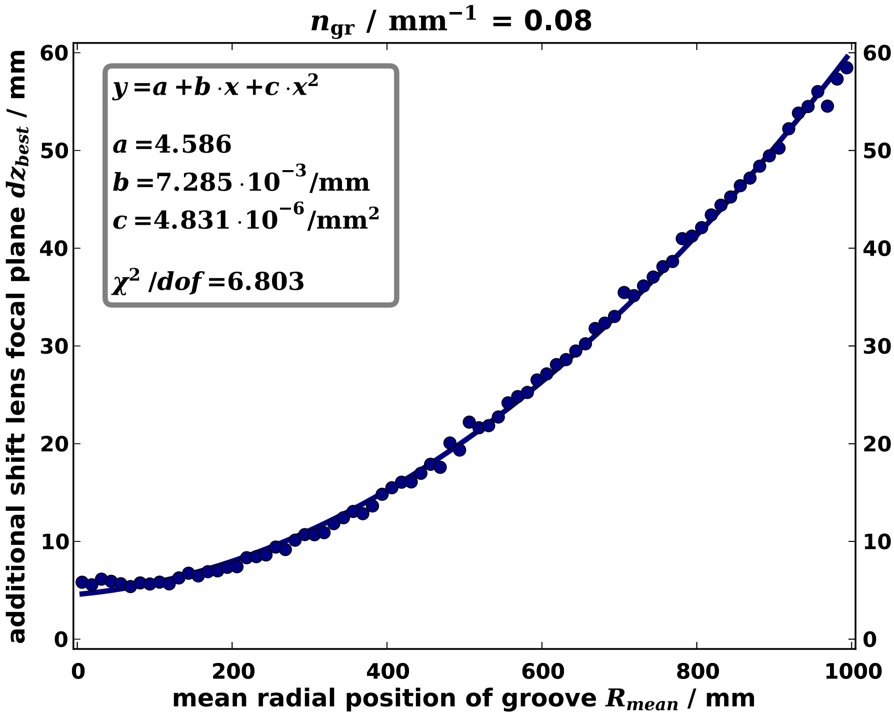

(b) 0.08 grooves/mm

Figure 5.26: Determination of the optimal distance dz_{best} as a function of the radial position of the grooves. Shown is a parabolic fit on the simulated data.

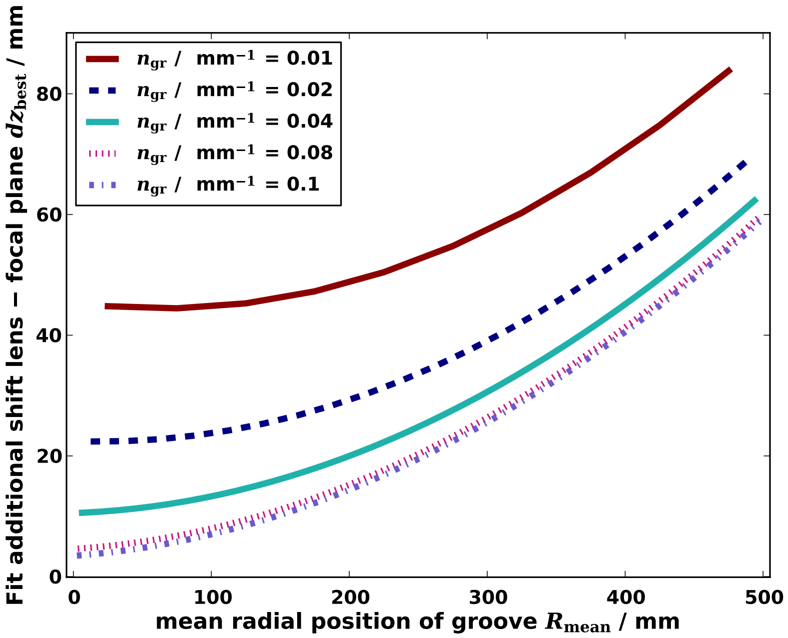

Figure 5.27: Fit of the optimal distance dz_{best} as a function of the radial position of the grooves. The different line styles denote different degrees of granularity.

Alternatively, the determined distance dz_{best} for each groove can be converted into a modified groove shape. Therefore, no additional material is acquired. In this study, this method is applied to construct a modified lens.

5.3.2 Optimisation of Groove Shape

The height h of a groove covering the radial range $[r_1, r_2]$ is calculated depending on the focal length f_{lens} according to the profile equation $s(r)$ (cf. equation (4.5)). Based on the functional relation (cf. equation (5.6)) between the mean radial position R_{mean} and dz_{best}, the height of each groove covering the radial distance $[r_1, r_2]$ of the lens is modeled by applying a focal length $f' = f_{\text{lens}} - dz_{\text{best}}$ corresponding to the mean radial position of the groove to compensate the difference in the optimal groove-focal-plane distance:

$$\text{h} = s(r_2) - s(r_1) = \frac{1}{2 \cdot f' \cdot (n_{\text{PMMA}} - 1)} \cdot (r_2^2 - r_1^2) \tag{5.7}$$

depending on the refractive index of the lens.

To determine the degree of optimisation a 2 m diameter Fresnel lens is simulated for different granularities and incident angles. The minimal possible aberration radius for each configuration is determined and compared with the aberration radius of a Fresnel lens based on the same simulation parameters but calculating the surface curvature of the groove with the focal length f_{Lens} of the bulky lens.

The change of the minimal possible r_{90} radius is calculated for the minimum of the aberration radius of each incident angle θ_{in} (shown in figure 5.29 and depicted in table 5.2).

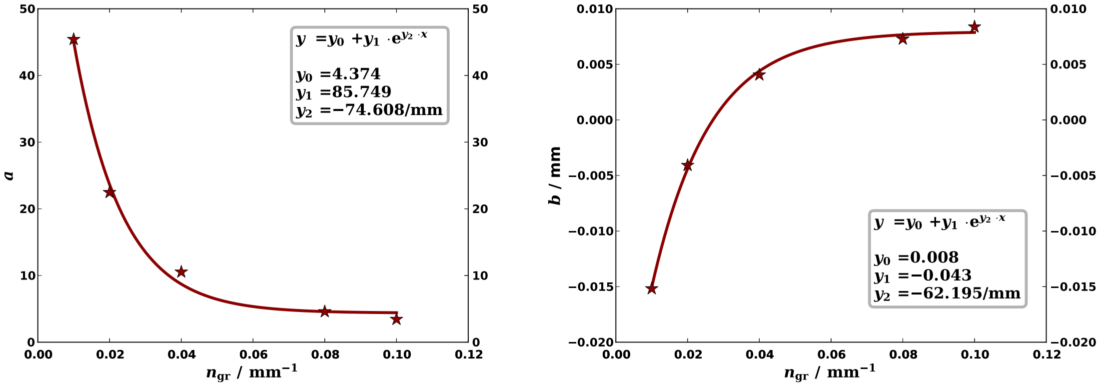

(a) Fit of parameter a (b) Fit of parameter b

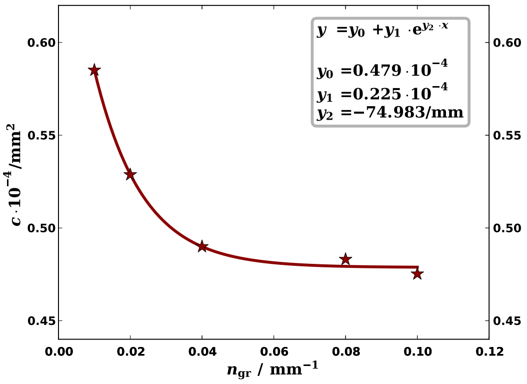

(c) Fit of parameter c

Figure 5.28: Fit for the determination of the three parameters a, b, and c of the parabolic functional relation between the optimal distance dz_{best} and the radial position of the grooves R_{mean}. Shown is each parameter as a function of the granularity n_{gr} of the lens. The data are best described by an exponential fit.

As expected the image quality of the lens is significantly improved for an incident angle of $\theta_{in} = 0\,°$. For other incident angles, the application of the parametrisation shows either only a slight influence on the minimal possible r_{90} radius or even a worse image quality for higher incident angles.

5.3.3 Study of Uncertainties on the Modification

The lens is modified by a parametrisation which defines the optimal shift for each groove as a function of the amount of grooves per mm and the radial position of each groove (cf. equation (5.6)). Uncertainties on the minimal aberration modified lens are determined:

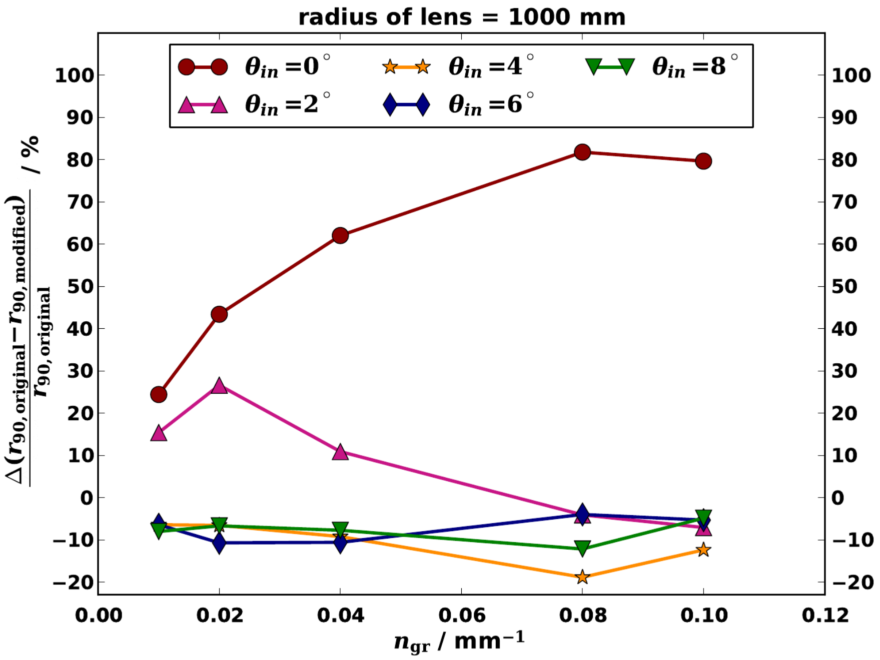

Figure 5.29: Comparison of the minimal aberration radii for the original Fresnel lens and the minimal aberration radii for the modified lens. Shown is the relative difference Δ for the minimal r_{90} radius as a function of the amount of grooves per mm n_{gr}. The minimal aberration radius is determined for each incident angle θ_{in}.

incident angle / °	**grooves / mm**	**minimum r_{90} / mm**	
		original lens	modified lens
0	0.01	9.89	7.48
	0.1	6.42	1.31
2	0.01	10.43	8.82
	0.1	9.32	9.98
4	0.01	14.04	14.94
	0.1	14.18	15.93
6	0.01	22.05	23.46
	0.1	21.12	22.24
8	0.01	30.31	32.74
	0.1	27.76	29.11

Table 5.2: Comparison of the minimal r_{90} radii for the original lens and the modified lens for each incident angle θ_{in}. Shown are the minimal aberration radii for two stages of granularity.

Uncertainties on the calculation of the parametrisation

The uncertainty on the used parametrisation is estimated by applying for each amount of grooves per mm an individual function determined by the best fit on the data as shown in figure 5.26.

Uncertainties on the manufacturing

The uncertainty on the simulation is compared with the uncertainty on the shape of the groove by the manufacturing of the Fresnel lens. Commonly a master tool is produced by milling machines. Thereby, polymeric Fresnel lenses can be fast reproduced. By using a CNC automatic milling machine the shape of the groove can be produced with an accuracy of approximately 0.02 mm [70]. This uncertainty is used as a first estimation and is applied to the modified lens by changing equally the height of each groove by ±0.02 mm. However, Fresnel lenses can be produced by more dedicated manufacturing processes with a better accuracy.

The influence of these uncertainties are listed in table 5.3 for the optimisation for each incident angle θ_{in} exemplary for two degrees of granularity. The uncertainties introduced by the use of the parametrisation are in the same order of the uncertainties introduced by the imperfect manufacturing of the lens.

Although the aberration radius is mostly improved by the individual function for each amount of grooves per mm, the image quality of the customized lens is still only increased for an incident angle of $\theta_{in} = 0\,^{\circ}$ referring to the angle for which the shape of the grooves has been optimised.

The application of an equal change of the groove height for each groove determines minimal aberration radii which fluctuate around the r_{90} radii of the modified lens.

As a deterioration of the image quality is expected, the fluctuations are studied in more detail:
The optimal distance for each individual groove of the modified lens is determined. Ideally, each groove should have the same optimal distance as expected. As shown in figure 5.30, the spread of the optimal distance is strongly improved but still the optimal distances for all groove are not the same. Therefore, an optimised aberration radius may occur if a different height of the groove is applied.

Furthermore, the modified lens is not optimal for higher incident angles. The change of the height thus may lead to an improvement of the image quality.

5.3.4 Optimisation for Finer Granularity

Also an optimisation of a Fresnel lens with a larger set of grooves per mm has been investigated. Therefore, the granularity of the 2000 mm diameter lens has been fixed

incident angle / °	**grooves / mm**	**minimum r_{90} / mm modified lens**	$\frac{\Delta(r_{90,\text{modified}}-r_{90,\text{uncertainty}})}{r_{90,\text{modified}}}$ / %	
			uncertainty on parametrisation	uncertainty on manufacturing $h^{+0.02\,\text{mm}}_{-0.02\,\text{mm}}$
0	0.01	7.48	-1.79	2.43 3.39
	0.1	1.31	15.85	−10.15 −8.19
2	0.01	8.82	-0.66	4.26 3.89
	0.1	9.98	11.82	5.79 −9.63
4	0.01	14.94	1.83	3.21 3.82
	0.1	15.93	2.89	8.95 5.85
6	0.01	23.46	1.60	2.09 1.88
	0.1	22.24	-0.81	−13.23 2.24
8	0.01	32.74	1.36	−0.07 0.92
	0.1	29.11	-0.10	2.08 −0.42

Table 5.3: Estimation of the uncertainties on the simulation. Shown are the minimal r_{90} radii for the modified lens. The calculated aberration radius is compared to the aberration radius determined when for each amount of grooves per mm an individual function is applied. Also the minimal r_{90} radii by taking the uncertainty introduced by the manufacturing into account is listed.

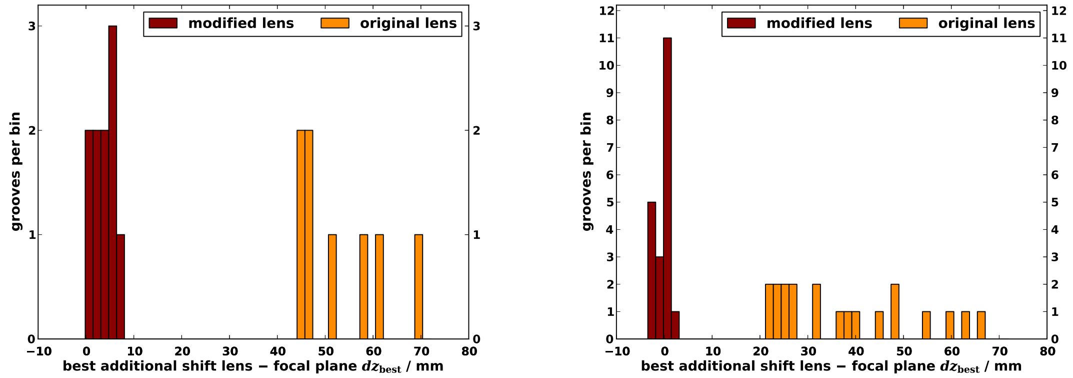

(a) n_{gr} / $\text{mm}^{-1} = 0.01$

(b) n_{gr} / $\text{mm}^{-1} = 0.02$

Figure 5.30: Histograms of the optimal shift dz_{best} for all individual grooves for different stages of granularities. Compared are the distribution of the original and the modified lens.

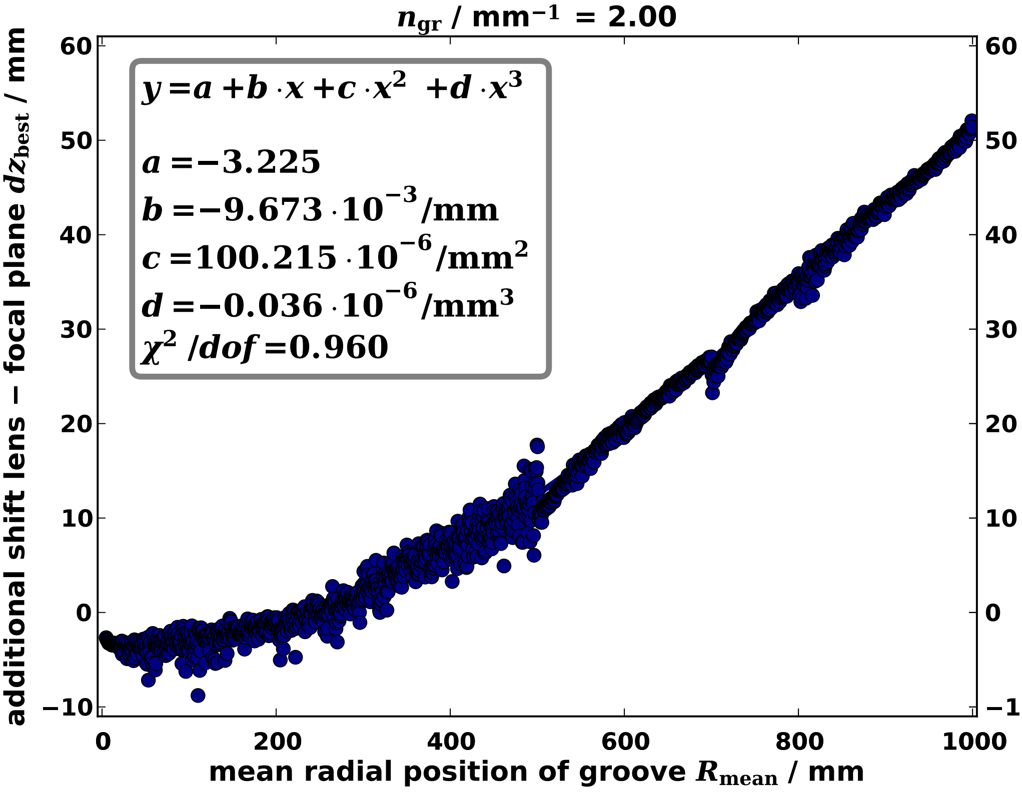

Figure 5.31: Determination of the optimal shift dz_{best} as a function of the mean radial position of the groove.

to 2 grooves/mm. This decision compromises between a granularity where the minimal possible r_{90} radius is already stable (cf. figure 5.7) as well as a dimension of the grooves where it could be still technical possible to put an optimisation of the groove shape into practice.

As for the previous study, the optimal distance between each groove of the lens and the focal plane is determined. The minimal distance as a function of the mean radius R_{mean} of each groove is depicted in figure 5.31. The calculated relation between the radial groove position in respect to the optical axis R_{mean}, the optimal shift dz_{best} and the lens granularity for smaller amount of grooves per mm can not be extrapolated up to $n_{\text{gr}} = 2$ /mm.

The optimisation of the lens by compensating the displacement of the groove onto a common base plate is analysed by the comparison of the minimal aberration radii for each incidnet angle θ_{in} for the original Fresnel lens and the minimal aberration radii for the modified lens (cf. table 5.4).

Taking the change of the light path into account significantly improves the image quality of the Fresnel lens for the incident angle for which the parametrisation has been optimised. The r_{90} radius for $\theta_{in} = 0\,°$ is improved from 5.96 mm to 0.52 mm respectively to about 9 % of the original value. For all other incident angles a slightly deterioration occurs.

incident	**r_{90} / mm**	
angle / °	original lens	modified lens
0	5.96	0.52
2	9.15	9.69
4	14.20	14.61
6	19.37	19.41
8	25.83	26.30

Table 5.4: Evaluation of the optimisation of the r_{90} radius by applying the change of an optimal distance between each groove and the focal plane. Listed are the aberration radii for the original and modified $2\,\mathrm{m}$ diameter Fresnel lens with a granularity of $2\,\mathrm{grooves/mm}$.

5.4 Evaluation

A study of a refractive optical telescope design using a Fresnel lens to focus the incoming light onto the focal plane has been presented whereby the size of the lens, the amount of number of grooves per mm and the distance between the lens and the focal plane have been left variable. The performance of the design has been optimised by analysing the minimal possible aberration radius r_{90} referring to the degree of blurring of the point spread function.
The influence of the chosen shape of the grooves has been investigated. Parabolic grooves, keeping the form of the original bulky lens, can be approximated by conical grooves for a granularity of the lens of above approximately one groove per mm. This refers to the preferred granularity to accomplish the best concentration power. The determined r_{90} radius and the angular distribution of the light onto the focal plane with respect to the optical axis are not improved by an application of parabolic shaped grooves.
Regarding both groove shapes, for large radii of the Fresnel lens the aberration radius rapidly increases and an implementation of a camera based on the relatively small sized light detection devices SiPMs may become insufficient.

Therefore, a possible optimisation has been performed correcting on the influence to the change of light path by an approximation of a bulky lens to a Fresnel lens and the displacement of the grooves onto a common base plate. By an illumination of each individual groove of the lens, an approximated functional relation of the optimal focal distance and the mean radial position of the groove can be determined. Applying the individual optimal focal length for each groove leads to a decreased minimal possible aberration radius for the incident angle for which the parametrisation has been determined. For all other incident angles the parametrisation shows a deterioration. However, the change of the light path may be taken into account by an optimisation of the groove shape for a minimal r_{90} radius for all incident angles. As this calculation would require many simulations due to a large amount of parameters, a dedicated study by the commercial optical design program ZEMAX is proposed. An analysis with Geant4 would be too slow.

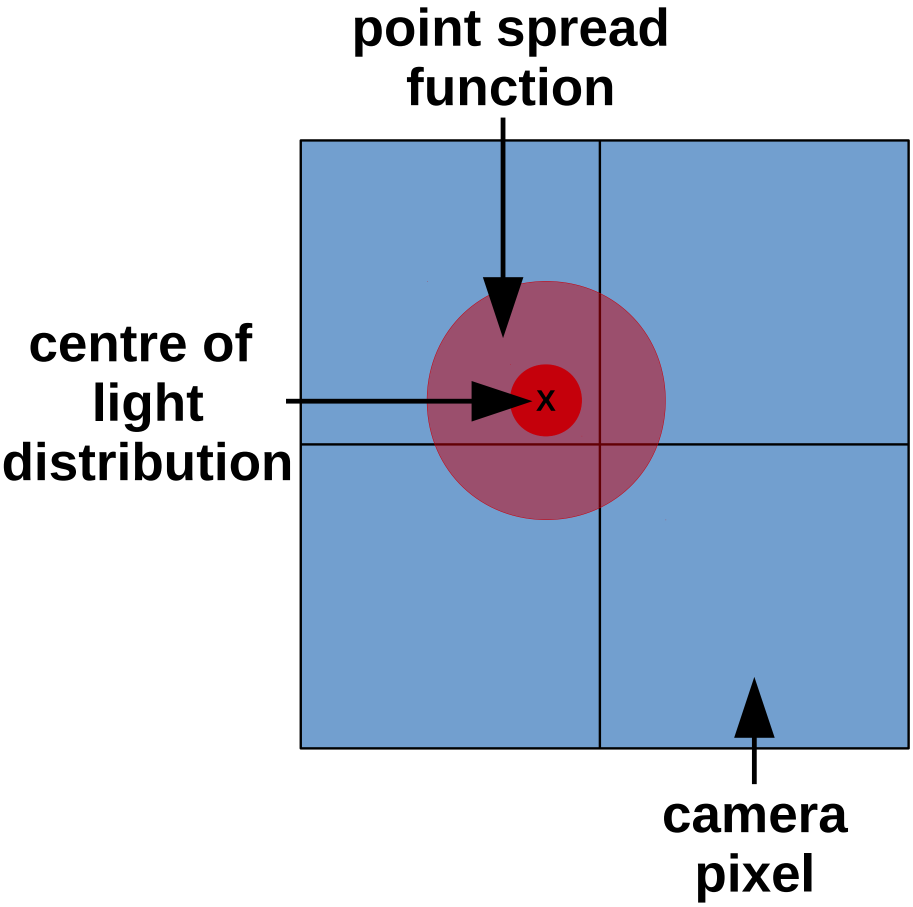

Figure 5.32: Sketch of the concept of a sampling camera. The spatial resolution is normally fixed by the size of the pixels. If coincident triggers of neighbouring pixels are required the centre of the light distribution can be calculated according to the detected light in each pixel. This leads to an improved spatial resolution.

Nevertheless, the overall performance of this refractive design is not optimal for the detection of fluorescence light by an SiPM camera: The aberration radius of a 2 m diameter lens is approximately 25 mm when the minimal aberration radius for all incident angles is required. As a comparison, the currently used hexagonal photomultiplier tubes (PMTs) of the Pierre Auger Fluorescence detector have a side to side pitch of 40 mm [5]. Thus, the nonimaging refractive design based on a Fresnel lens allowing a high transmission efficiency is a possible design for a fluorescence telescope detecting UHECRs by a PMT camera.

Regarding an SiPM camera based telescope as the FAMOUS prototype, still some opportunities can be investigated:
As a possibility to improve the poor spatial resolution due to large pixels, a sampling camera can be considered. A simplified example is shown in figure 5.32.

For a camera consisting of large sized pixels an improved spatial resolution can be achieved by simultaneously illuminating neighbouring pixels due to a blurred point spread function. As by an illumination of one pixel the spatial resolution is restricted by the size of the pixel, a coincident trigger in neighbouring pixels allows to determine the centre of the spot size analysing the amount of detected light in each pixel. The position of the centre can be determined with better accuracy and leads to an improved resolution.

Furthermore, the optimal field of view (FoV) of a fluorescence telescope can be reviewed by analysing the distribution of the maximal slant depth X_{max} of air showers. The question arises when X_{max} can be best reconstructed and resolved regarding the energy of the shower and the distance to the shower core. Thereby, the needed FoV in elevation and the elevation angle of the telescope will influence the requirements of a fluorescence telescope baseline design. A small field of view may allow a decrease of the focal length and a decrease of the aberration radius, as the r_{90} radius strongly increases with higher incident angles. Thus, larger Fresnel lens radii leading to an increased light collection area may be considered for an SiPM camera.

For the FAMOUS camera pixels 6 mm × 6 mm SiPM units are used. Thereby, each SiPM unit consists of four 3 mm × 3 mm SiPMs which can be read out separately or summed up. For FAMOUS, the trigger is based on the sum of all four SiPMs signals. For small apertures of the optical design, the amount of collected light is relatively low and taking the sum of each SiPM unit emerges as best discriminator. An increased aperture allows the collection of more light and a separate read out of each SiPM becomes more efficient. A dedicated study of this efficiency as a function of the light collection area could determine if a separate read out becomes sufficient to allow coincidence measurements. Requiring coincidences between the individual SiPMs of each unit would reduce the influence of the intrinsic noise of each SiPM leading to an improved signal-to-noise ratio and hence allows to enlarge the SiPM unit size. While increasing the size of each SiPM unit would lead to a strongly increased noise rate by reading out the summed-up signals, the requirement of coincidences could counteract this.

As a first assessment of the performance of the refractive design, the amount of fluorescence light reaching one pixel of the SiPM camera for vertical showers is roughly estimated.

While an extensive air shower travels through the atmosphere, fluorescence light is emitted isotropically. As the distance from the telescope to the shower core R_{p} of several km is large in comparison to the aperture area A of the telescope and the area of the region from which fluorescence light is emitted at a certain time, the size of the latter can be neglected assuming the „10-times-law“ [78]. Based on this assumption and taking into account that only a part of the emitted fluorescence light is reaching the telescope, the flux of fluorescence photons reaching a telescope aperture A has been calculated [82] based on the usage of radiometric quantities:

$$\Phi^{\mathrm{px}}_{\mathrm{shower}} = I_0 \frac{2 \cdot A \cdot \sin(\alpha_{\mathrm{FoV}}/2)}{R_{\mathrm{p}}^2} \exp^{-\alpha \cdot R_{\mathrm{p}}} \qquad . \tag{5.8}$$

The flux depends thereby on the aperture area A and the field of view α_{FoV} of the telescope. The distance from the shower core to the telescope R_{p} is constant for vertical showers. The intensity I_0 is defined as the amount of fluorescence photons emitted per second and certain solid angle at the point of the emission. The intensity I_0 is corrected by the correction factor $\alpha = 7.45 \cdot 10^{-2}\,\mathrm{km}^{-1}$ for the attenuation of the fluorescence light intensity due to the large travelled distance up to the telescope. Thereby, as an estimation only Rayleigh attenuation is taken into account.

While the shower develops in the atmosphere, the emitted fluorescence light is seen as a track in the camera. At each time of the duration of an event, the air shower is seen as a point source by the telescope. Therefore, at each time the fluorescence light is focused into only one single pixel of the camera. Therefore, the given flux can be assumed to be the flux of fluorescence light reaching one responding pixel of the camera (cf. equation 5.8).

The amount of fluorescence photons has to be compared to the expected noise and to the amount of background photons reaching the telescope for an evaluation of the performance. The limitation of the detector capabilities are defined by the number of detected photons originating from other light sources than the fluorescence light as well as by the dynamic range of the SiPM:

Night-sky brightness

As the fluxes of the fluorescence light are very small, the duty cycle of a fluorescence telescope is reduced to dark and moonless nights. The telescope has to be able to distinguish between the signal and the background flux of the night-sky brightness (NSB). The NSB summarises light from natural sources and artifical light sources by civilisation. Near Aachen, an upper limit of the NSB radiance L_{NSB} of

$$L_{\mathrm{NSB}} \leq 1.9 \cdot 10^{12}\,\mathrm{m}^{-2}\mathrm{s}^{-1}\mathrm{sr}^{-1} \tag{5.9}$$

has been determined for the fluorescence wavelength regime [81]. The NSB photons reaching the aperture area A of the telescope has to be included into a cone spanned by the field of view α_{FoV} of the telescope. The flux reaching one pixel depends on the field of view seen by the pixel α_{px} and can be then assumed as

$$\Phi_{\mathrm{NSB}}^{(\mathrm{px})} \leq L_{\mathrm{NSB}} \cdot 2\pi\,(1 - \cos(\alpha_{\mathrm{px}}/2)) \cdot A \qquad . \tag{5.10}$$

Dark noise counts of SiPM

The dynamic range of SiPMs is strongly limited by noise effects and defines the lower boundary of the detection capabilities of the telescope. The noise rate is thereby estimated by considering the dark count rates of the SiPM (cf. chapter 4.1). For currently available SiPM types [61], the dark count rate for an SiPM is typically $f_{\mathrm{dc}} = 100\,\mathrm{kHz/mm}^2$ leading for each pixel with an area A_{SiPM} to a noise flux of

$$\Phi_{\mathrm{dc}}^{(\mathrm{px})} \approx f_{\mathrm{dc}} \cdot A_{\mathrm{SiPM}} \qquad . \tag{5.11}$$

A telescope based on the following parameters (cf. table 5.5) is investigated based on the optimisation for all incident angles θ_{in} on a 2 mm diameter lens with conical grooves as shown in figure 5.4.

The size of the focal plane is calculated by

$$D_{\mathrm{fp}} = D_{\mathrm{lens}} \cdot \frac{\tan(\alpha_{\mathrm{FoV}}/2)}{\tan(\theta_{\mathrm{max}})} \tag{5.12}$$

aperture	r_{lens}	1000 mm
Winston cone entrance radius	r_1	25.63 mm
Winston cone exit radius	r_2	13.32 mm
max. accepted angle by Winston cone	θ_{max}	31.30 °
focal ratio	$N_f = f/(2 \cdot r_{\text{lens}})$	1
field of view per pixel	α_{px}	1.5 °
field of view	α_{FoV}	16 °

Table 5.5: Parameters of a refractive optical baseline design for a $2\,\text{m}$ diameter lens.

leading to a number of pixels of the camera of $\sqrt{n_{\text{px}}} = D_{\text{fp}}/(2 \cdot r_1) \simeq 10$ per one dimension.

A typical vertical shower with an energy of $E = 10^{18.5}\,\text{eV}$ has a peak intensity of approximately $I_0 = 10^{18}\,\text{photons}\,\text{s}^{-1}\,\text{sr}^{-1}$ [82]. Assuming a shower reaching the ground at a distance between shower core and telescope of $R_{\text{p}} = 3\,\text{km}$, the estimated flux of fluorescence photons reaching one camera pixel is calculated and compared with the estimated fluxes of the background:

$$\Phi^{\text{px}}_{\text{shower}} \simeq 100\,\text{GHz} \tag{5.13}$$
$$\Phi^{\text{px}}_{\text{NSB}} \leq 3\,\text{GHz} \tag{5.14}$$
$$\Phi^{\text{px}}_{\text{dark count}} \simeq 80\,\text{MHz} \tag{5.15}$$

While an air shower develops in the atmosphere, the incoming fluorescence light will illuminate several pixels of the camera. The mean number of illuminated pixels $n_{\text{px}}^{\text{response}}$ is thereby assumed to be at least in the order of the number of pixels in one dimension.
The duration of a typical event at the chosen distance $R_{\text{p}} = 3\,\text{km}$ is about $t_{\text{shower}} = 3\,\mu\text{s}$. Therefore, the calculation of the total amount of photons is determined by the whole event duration t_{shower} for the expected rates of the NSB photons and the dark noise of the SiPM. For the fluorescence signal reaching the camera, each pixel is only illuminated for a short time. Therefore, only a part of the complete event duration time has to be taken into account to calculate the total amount of photons at one pixel: $t \simeq t_{\text{shower}}/n_{\text{px}}^{\text{response}}$.

$$N^{\text{px}}_{\gamma,\text{shower}} \simeq 30 \cdot 10^3 \tag{5.16}$$
$$N^{\text{px}}_{\gamma,\text{NSB}} \leq 9 \cdot 10^3 \tag{5.17}$$
$$N^{\text{px}}_{\gamma,\text{dark count}} \simeq 240 \tag{5.18}$$

Although the refractive design is not optimal for the fluorescence light detection with an SiPM camera, the estimated amount of photons per responding pixel is an order of magnitude larger than the expected background of the night-sky-brightness.

Chapter 6

Reflective Telescope

Reflecting optical designs are based on the use of a single or a combination of mirrors. Each design includes an active mirror producing a magnified image on the focal plane from distant objects. Besides, passive mirrors are used to deflect the focused light out of the optical axis as often used for astronomical telescopes and are commonly planar [86]. In contrast to refractive optical designs, reflective systems are free from chromatic aberration, but may suffer from obstruction introduced by the placement of the focal plane or secondary mirrors into the path of light.

Along the variety of reflecting telescope designs, the Schmidt camera optics proved as an optimal design for the detection of the faint fluorescence light emitted by extensive air showers [5]. The optics allows a large entrance aperture and a wide field of view by obtaining an adequate focusing power with a focal ratio $N_f \simeq 1$. As already presented in chapter 3.2.1 the Schmidt camera optics is successfully used at the fluorescence detector (FD) of the Pierre Auger Observatory.

6.1 Schmidt Telescope Simulation

The baseline design of the Schmidt camera optics [77] consists of an active primary spherical mirror which focuses the light onto the focal plane. The focal plane is thereby located at the centre of the optical axis to avoid off-axis aberrations. For the Schmidt camera optics, the application of a focal ratio $N_f \leq 1$ is possible whereby the obstruction by the camera is minimised and a compact design with a large field of view is achieved. The baseline design of the Schmidt camera optics is depicted in figure 6.1.

The radius of the mirror $R_{\mathrm{mirror}} = 2 \cdot f$ is fixed by the focal length f. The focal plane is ideally located at the centre between the aperture and the spherical mirror. Since a compact design is required, the focal ratio $N_f \leq 1$ defines an entrance aperture radius of about $R_{\mathrm{p}} \geq R_{\mathrm{mirror}}/4$.

In figure 6.2 the image quality of a telescope with a $R_{\mathrm{mirror}} = 3400\,\mathrm{mm}$ and a focal length of $f = 1700\,\mathrm{mm}$ for several sizes of aperture R_{p} is shown referring to the optical design of the Pierre Auger FD. The image quality is strongly reduced by decreasing the focal ratio due to spherical aberration.

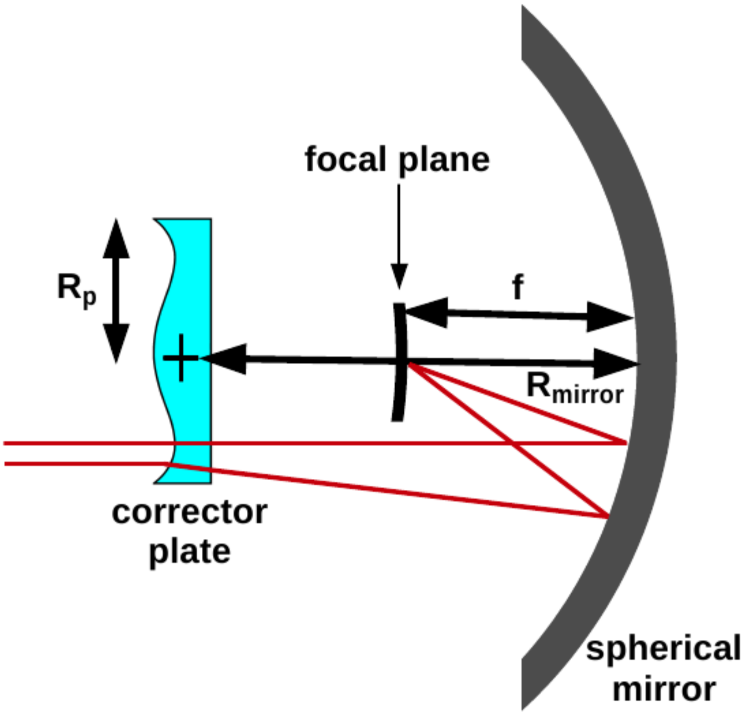

Figure 6.1: Sketch of the Schmidt camera optics. The aperture is defined by the radius of a Schmidt corrector plate R_p. The incoming light is reflected by the spherical mirror with a radius of R_mirror onto the curved focal plane. The focal plane is located at $R_\mathsf{mirror}/2$ referring to the focal length f of the telescope design.

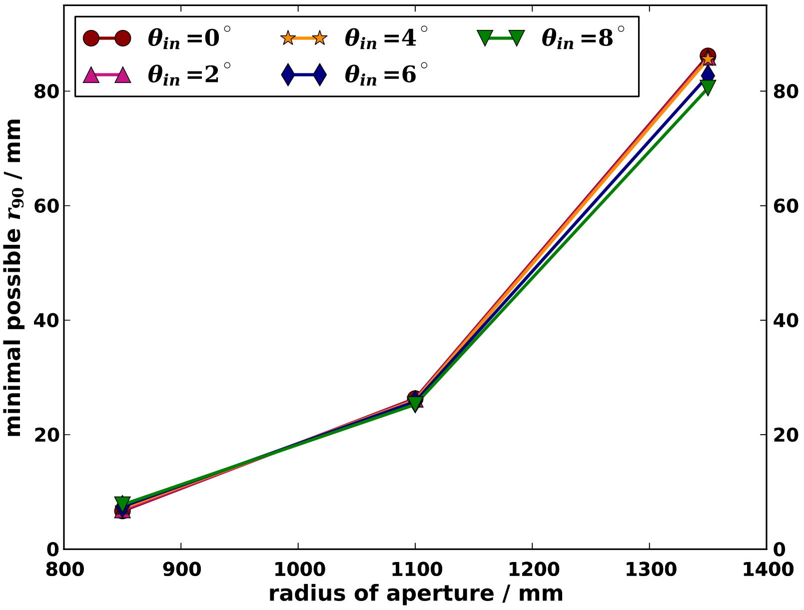

Figure 6.2: Image quality of the Schmidt camera optics without a corrector plate for different focal ratios. Shown is the minimal aberration radius as a function of the size of the aperture for a telescope design with a fixed radius of the mirror $R_\mathsf{mirror} = 3400\,\mathrm{mm}$ and a fixed focal length $f = 1700\,\mathrm{mm}$.

Therefore, the telescope design is optimised to reduce the effects of aberrations introduced by the spherical mirror. This allows the application of smaller focal ratios leading to an enlarged field of view.

curvature of field	For different incident angles the position of the focal plane slightly differs forming images over a curved surface symmetrical around the optical axis. As a compensation, a spherical curved focal plane has to be applied with $R_{\mathrm{fp}} = f$.
spherical aberration	The use of a spherical mirror introduces spherical aberrations leading to a focal length which depends on the incident position of the incoming light ray with respect to the optical axis. To correct for this aberration an aspheric refractive corrector plate is applied commonly known as Schmidt corrector plate. By the corrector plate, the wavefront of the incoming light is optimised before its reflection by the spherical mirror to compensate the spherical aberration. As the plate is relatively thin, the introduced chromatic aberration is adequately small. The concept of an implementation of a Schmidt corrector plate is illustrated in figure 6.3.

On the basis of the promising quantities of the Schmidt camera optics, this design is investigated for the detection of fluorescence light by a silicon photomultiplier (SiPM) camera. Regarding the small size of this light detection device, the baseline design has to be optimised to achieve a sufficient image quality referring to a small aberration radius r_{90}. Therefore, the Schmidt telescope is studied by ray-tracing simulations based on the Geant4 framework.

The image quality depends strongly on the aperture, which is defined by the size of the corrector plate. Its radius R_{p} is a free parameter in the following analysis.

6.1.1 The Schmidt Corrector Plate

The important optical component of the Schmidt camera optics is the corrector plate which was first invented by Bernhard Schmidt in 1931.
The corrector is thin $\mathcal{O}(mm)$ and nearly planar. Its shape is shown in figure 6.4, whereby the slope is strongly exaggerated for the purpose of a better presentation.

The thickness $T(r)$ of the plate as a function of the radial position r with respect to the optical axis can be theoretically calculated according to equation (6.1): The shape depends thereby on the focal length f of the optical system, the refraction index n of the material as well as on the radius of the plate R_{p} [31].

$$T(r) - T(0) = \frac{r^4 - \frac{3}{2} \cdot R_{\mathrm{p}}^2 \cdot r^2}{32 \cdot (n-1) \cdot f^3} \tag{6.1}$$

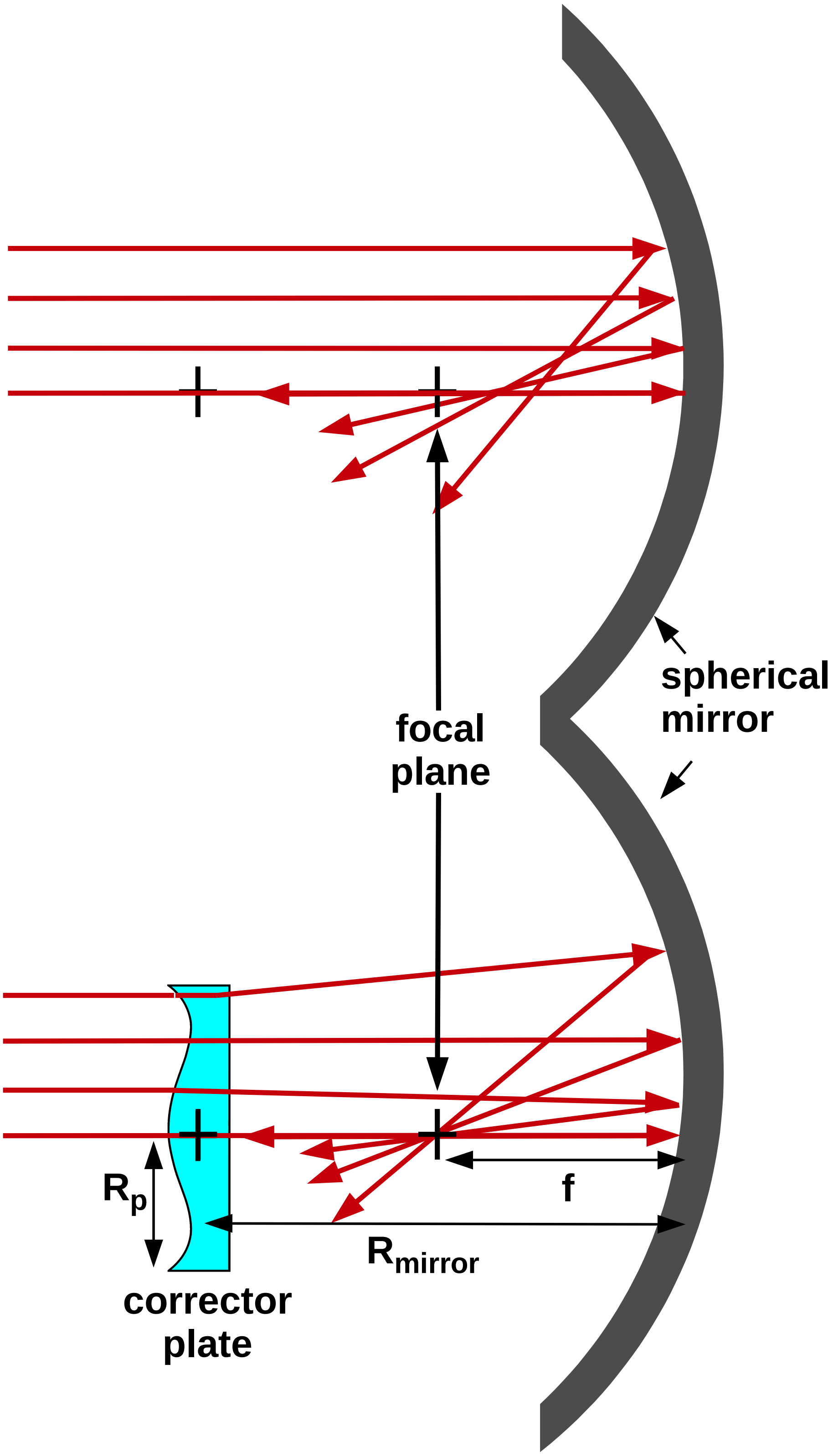

Figure 6.3: Illustration of the correction for spherical aberration by the Schmidt corrector plate. Without the plate, the image quality of the incoming light reflected by the spherical mirror is strongly reduced. By application of the plate, the wavefronts of the light is corrected in such a way, that the Schmidt camera optics is nearly free from spherical aberration leading to an improved image quality. The thickness and profile of the corrector plate are greatly exaggerated.

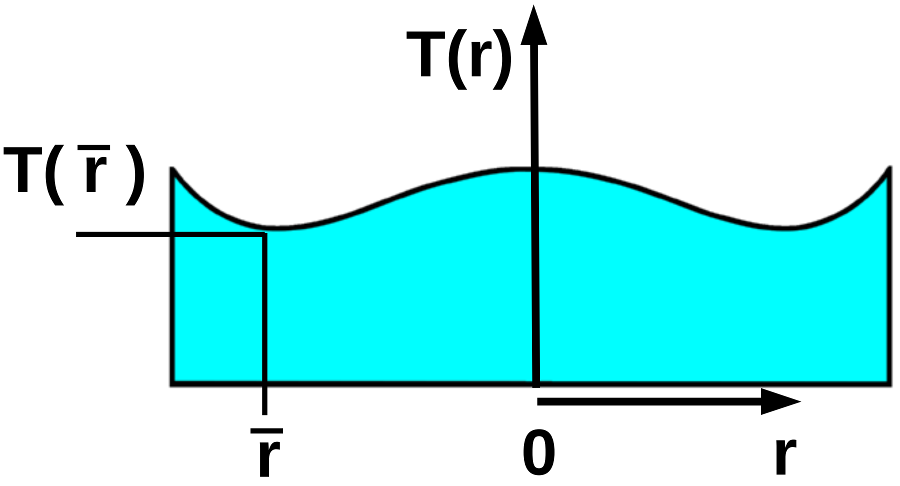

Figure 6.4: Profile of the Schmidt corrector plate. The thickness and profile of the corrector plate are greatly exaggerated. The total thickness $T(0)$ of the corrector plate is commonly in the order of a few mm, whereby most of the material is introduced for a better handling and stability of the plate. The neutral zone $\bar{r}$ indicates the region in which light rays are not influenced by the plate.

The maximal thickness of the corrector plate is given by $T(0)$. This total thickness $T(0)$ determines the degree of chromatic aberration. As this study is based on monochromatic light picked from the fluorescence light regime, chromatic aberration is not investigated. The total thickness $T(0)$ is estimated by calculating $T(\bar{r})$ for the neutral zone of the plate referring to the thinnest part of the lens. Thereby, $T(0)$ equal to 10 mm is chosen.

The position of the neutral zone $\bar{r}$ is defined as the region where incoming light rays are not deflected by the plate and is fixed by the radius of the aperture R_p:

$$\bar{r} = \frac{\sqrt{3}}{2} \cdot R_\mathrm{p} \qquad . \tag{6.2}$$

The theoretical profile of the Schmidt corrector plate for a certain aperture is validated by investigating the image quality respectively the aberration radius r_{90}. Therefore, the aperture of the Schmidt corrector is kept fixed.
The radius of the mirror $R_\mathrm{mirror} = 3400\,\mathrm{mm}$ is chosen to be the same as the mirror radius of the fluorescence detector of the Pierre Auger Observatory and is also a fix parameter.
As the Schmidt corrector is a continuous lens, the only free parameter left is the focal length f of the optical system. The profile of the plate depends on this parameter as well as the position and the curvature of the focal plane. Thus, the profile is determined by varying the focal length f and applying the change of the parameter also to the whole optical system. For the following analysis, one simulation is performed for each configuration with 100000 incident photons illuminating the whole aperture. In figure 6.5 the image quality for a 1100 mm radius plate is depicted for different incident angles. The size of the aperture has been chosen as the aperture size of the Schmidt camera optics of the fluorescence detector of the Pierre Auger Observatory.

As a first estimation of the focal length of the optical system, f is assumed to be in the range of $f \simeq 2 \cdot R_\mathrm{p} = 1700\,\mathrm{mm}$ as expected for the required focal ratio. However, the best image quality is achieved for a larger focal length, $f_\mathrm{optimal} = 1761\,\mathrm{mm}$. As the

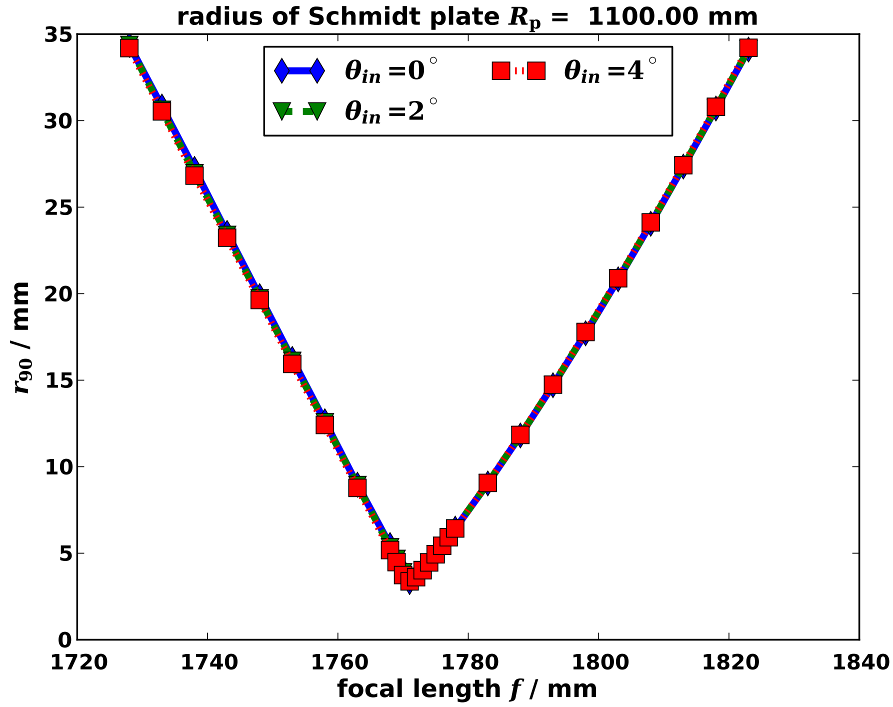

(a) complete range of focal length

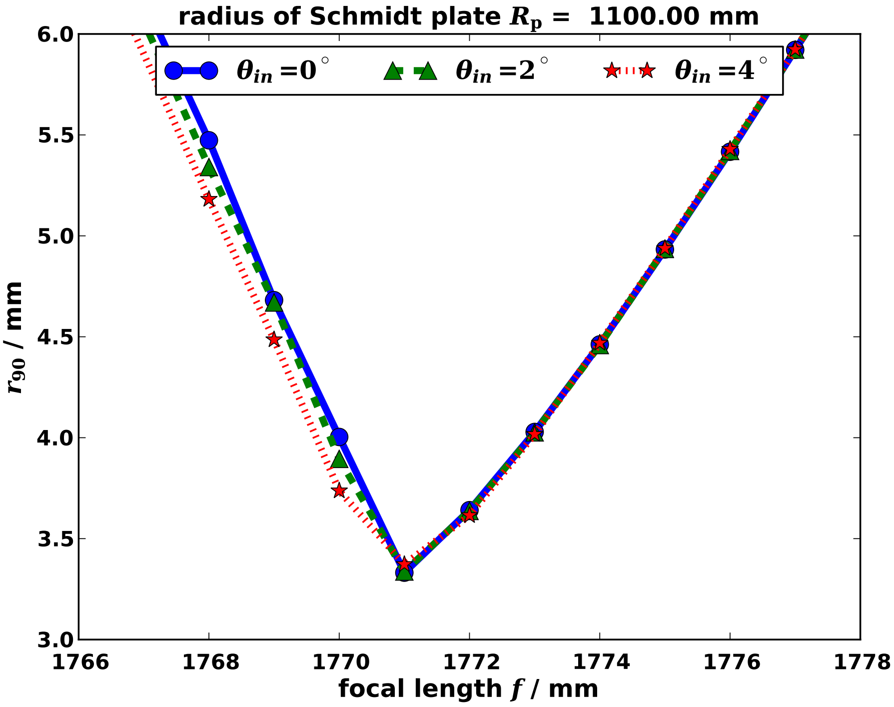

(b) zoom into the range around the minimum

Figure 6.5: Optimisation of the focal length f to obtain the optimal image quality. The focal length influences the shape of the Schmidt corrector plate. Shown is the aberration radius r_{90} as a function of the focal length. The optimal focal length is equal for different incident angles.

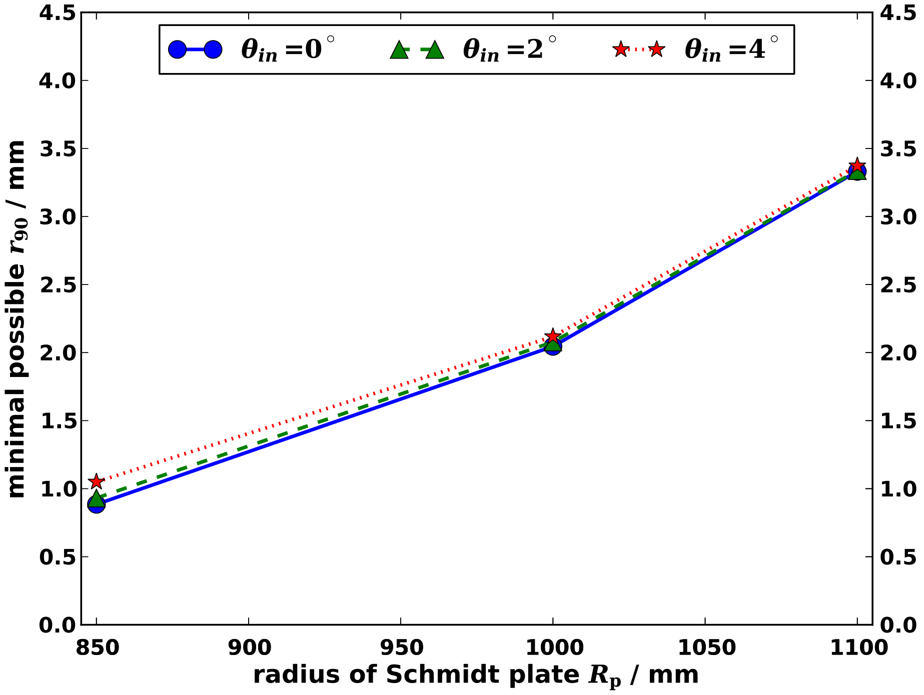

Figure 6.6: Optimisation of the Schmidt camera optics using a Schmidt corrector plate by the aberration radius r_{90}. For different incident angles, nearly the same image quality is obtained. The radius of the mirror is fixed to $R_{\text{mirror}} = 3400\,\text{mm}$. The aberration radius for the telescope design without a Schmidt corrector plate is indicated.

telescope is corrected for the effect of curvature of field by applying a curved focal plane, the position of the optimal focal length is nearly uniform for different incident angles. Also the minimal aberration radius remains stable and only a slight decrease of the image quality for higher incident angles is determined. For each size of the aperture, the optimal focal length has to be individually determined, whereby the radius of the mirror has been fixed to $R_{\text{mirror}} = 3400\,\text{mm}$ as the application of a Schmidt corrector will allow a larger aperture for the same radius and focal length of the telescope design. The image quality as a function of the aperture radius R_p decreases by increasing the size of the aperture (cf. figure 6.6). However, for all investigated sizes of the corrector plate the minimal aberration radius shows a sufficient focusing power for the use of an SiPM camera. As the image quality is nearly independent of the incident angle, this optical design allows a large field of view.

While the implementation of the Schmidt corrector plate yields a promising performance regarding the spot size on the focal plane, the application of the plate in the optical system will reduce the transmission efficiency of the telescope. As the fluorescence light is very faint and the duty cycle of a fluorescence telescope is limited to clear and moonless nights, a high transmission efficiency is required to obtain an improved collection of light allowing the detection of more distant and lower energetic showers.

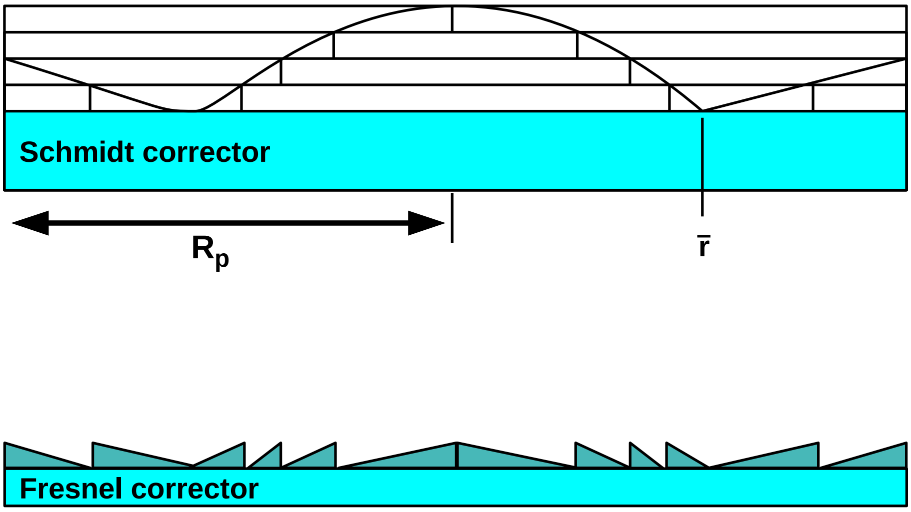

Figure 6.7: Illustration of the construction of a Fresnel corrector plate based on the model of a Schmidt corrector plate. The grooves of the Fresnel corrector plate are equally high.

6.1.2 Fresnel Lens Approximation of the Schmidt Corrector Plate

As already introduced in the previous chapters of the refractive design, a bulky lens can be reduced in weight, absorption and cost by an approximation with a Fresnel lens.
The same approach is respected for the reflective Schmidt telescope. A replacement of the Schmidt corrector plate by a Fresnel plate may increase the transmission efficiency of the optical system. The performance of the Fresnel plate is investigated and the optimal design regarding the image quality is determined.

The construction principle of a Fresnel plate is shown in figure 6.7. The base plate of the Schmidt corrector plate is maintained and its profile is approximated by conical grooves with equal height.

The Fresnel lens is modeled by the studied Schmidt corrector plate in the previous section and the same optimal focal length depending on the size of the aperture is applied.
However, as shown in the previous chapter, the optimal lens-to-focal-plane distance does not correspond to the focal length as expected for a conventional lens. Due to imperfections of the imaging characteristics of the Fresnel plate, a shift dz on the optical axis is needed additionally to the expected distance between focal plane and mirror. The shift dz is thus implemented as free parameter. Furthermore, an equal height h for all groove is implemented whereby the height is left variable to determine the best approximation of the original profile $T(r)$.

6.2 Baseline Design Optimisation for the FAMOUS Camera

The reflective optical design of a Schmidt telescope with a Fresnel corrector plate is investigated to achieve a baseline design suitable for the detection of extensive air showers by a silicon photomultiplier camera. As SiPMs are small sized light detection devices, the possible reduction of the spherical aberration and the improvement of the image quality

Aperture	R_p	250 mm
Focal ratio	$N_\mathrm{f} = \frac{f}{2 \cdot R_\mathrm{p}}$	1
Number of pixels	n_px	64 SiPMs, hexagonal packaging
Entrance radius of Winston cone	r_1	6.71 mm
Exit radius of Winston cone	r_2	3 mm
Pixel field of view angle	α_px	1.5 °
Total field of view	FoV	12 °
r_{90} for $\theta_{in} = 0\,°$	r_{90}	1.6 mm
Transmission efficiency	T	$\simeq 55\,\%$

Table 6.1: Parameters of the telescope design of the fluorescence detector prototype FAMOUS [82].

by the Fresnel corrector plate have to be determined.

As the FAMOUS prototype has successfully implemented an SiPM camera for the detection of fluorescence light, the reflective optical design requires a similar image quality for the use of an SiPM camera. The optical quantities of the FAMOUS prototype are reviewed in table 6.1.

The crucial parameter for a determination of an optical design for the SiPM camera of FAMOUS is thereby the entrance radius of the Winston cone. For an optimal detection efficiency for fluorescence light in turn, a large field of view and a large aperture is required. As for an increased aperture the maximal angle on the focal plane will also increase, the concentration power of the Winston cone will be reduced. Regarding the small sizes of the SiPMs, the minimal needed aberration radius of the reflective design should be therefore in the range of the Winston cone entrance of the FAMOUS camera.

For the reflective design, the Fresnel plate has to be optimised to achieve the best possible reduction of aberration:
The image quality is improved for a finer subdivision into grooves of the corrector profile (cf. figure 6.8). For a sufficiently large number of grooves, the Schmidt corrector plate profile can be adequately reproduced by the Fresnel corrector plate and the minimal aberration radius r_{90} coincides for different incident angles compared to the original plate. For comparison purposes, the minimal possible aberration radius of the Schmidt corrector plate is also indicated in the plot.

For an optimal approximation of the shape, a very small groove height of $\mathcal{O}(\mu\mathrm{m})$ is required. However, also for a Fresnel lens of 2 m diameter with a granularity of 2 grooves per mm, the height of the grooves ranges between [0.01 μm, 500 μm]. Therefore, a large sized optimal component approximated by a Fresnel lens is a highly complex device and challenging to manufacture with a sufficient accuracy.

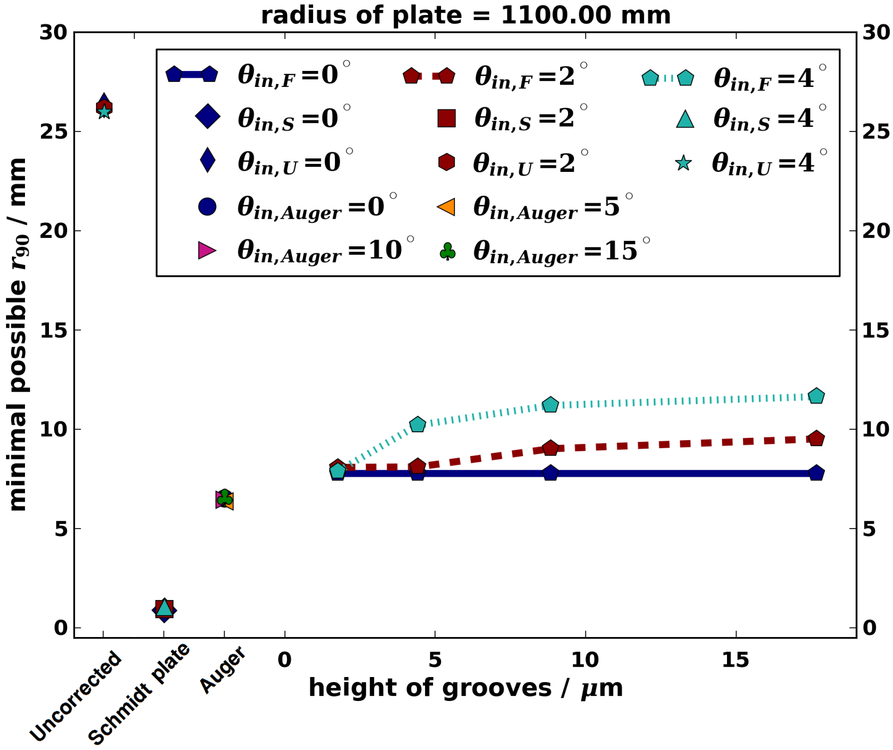

Figure 6.8: Optimisation of the image quality as a function of the height of the grooves into the Fresnel corrector plate is divided. Each groove is equally high. Shown are the minimal r_{90} radii for different incident angles ($\theta_{in,\mathrm{F}}$) for a plate radius of 1100 mm. For an easier comparison, also the aberration radii determined for the continuous Schmidt corrector plate ($\theta_{in,\mathrm{S}}$), the telescope without any correction ($\theta_{in,\mathrm{U}}$) and the fluorescence telescope of the Pierre Auger Observatory ($\theta_{in,\mathrm{Auger}}$) are depicted.

Nevertheless, the further simulations of a Fresnel plate with a radius of 1100 mm are performed with an equal groove height of 1.7 μm to achieve the optimal image qualities.

As the focal length f has been chosen to be the same as the focal length of the underlying Schmidt corrector plate, a uniform shift $dz = 5$ mm needed additionally to the focal length f for all incident angles is determined for a Fresnel plate with a radius of 1100 mm as shown in figure 6.9.

Based on these optimisations of the Fresnel plate, the overall minimal achievable aberration is calculated for different sizes of the aperture while the radius of the mirror is kept fixed. The aberration radius strongly increases with larger radii of the plate R_{p}, but is nearly uniform for all incident angles (cf. figure 6.10). The performance of the Fresnel plate in comparison to the Schmidt corrector plate shows an approximately three times higher r_{90} radius.

As the simulated image quality is reduced by the replacement of the Schmidt by a Fresnel corrector plate, the simulated transmission efficiency is improved (cf. figure 6.11). As an estimation of the transmission, the ratio of the number of photons passing through the plate and the number of photons emitted from the source is determined. Both types of

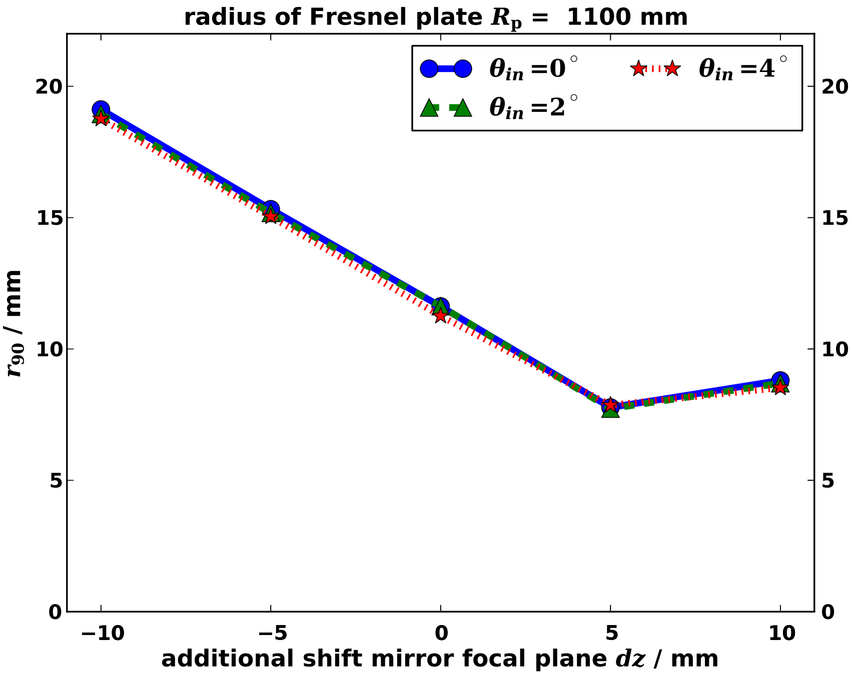

Figure 6.9: Optimisation of the additional shift dz between the distance of the Fresnel plate and the mirror. Shown is the aberration radius as a function of the shift for different incident angles on a $1100\,\mathrm{mm}$ radius plate.

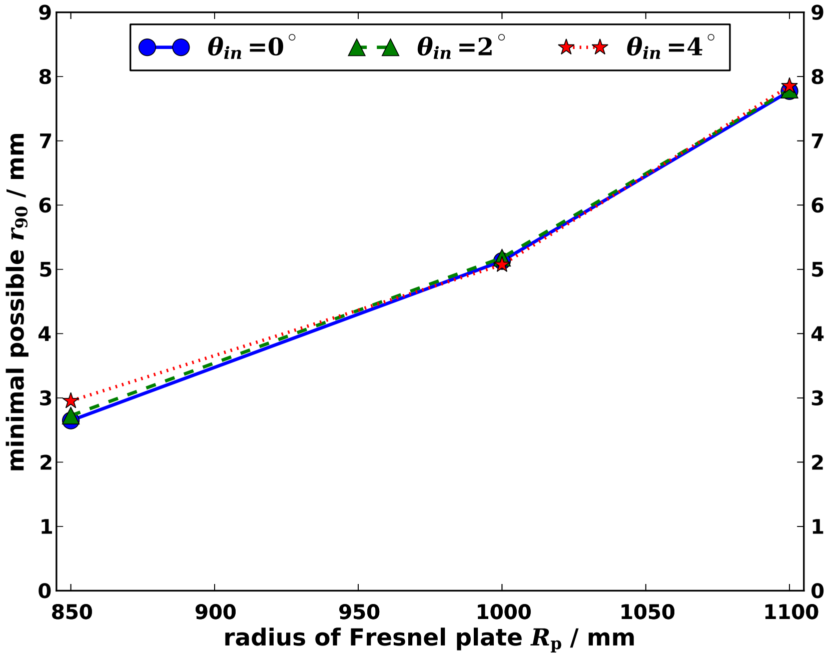

Figure 6.10: Minimal possible r_{90} radius as a function of aperture radius R_p for a Fresnel plate with an equal groove height of $1.7\,\mu\mathrm{m}$. The aberration radius is uniform for different incident angles. The radius of the mirror is fixed to $R_\mathrm{mirror} = 3400\,\mathrm{mm}$.

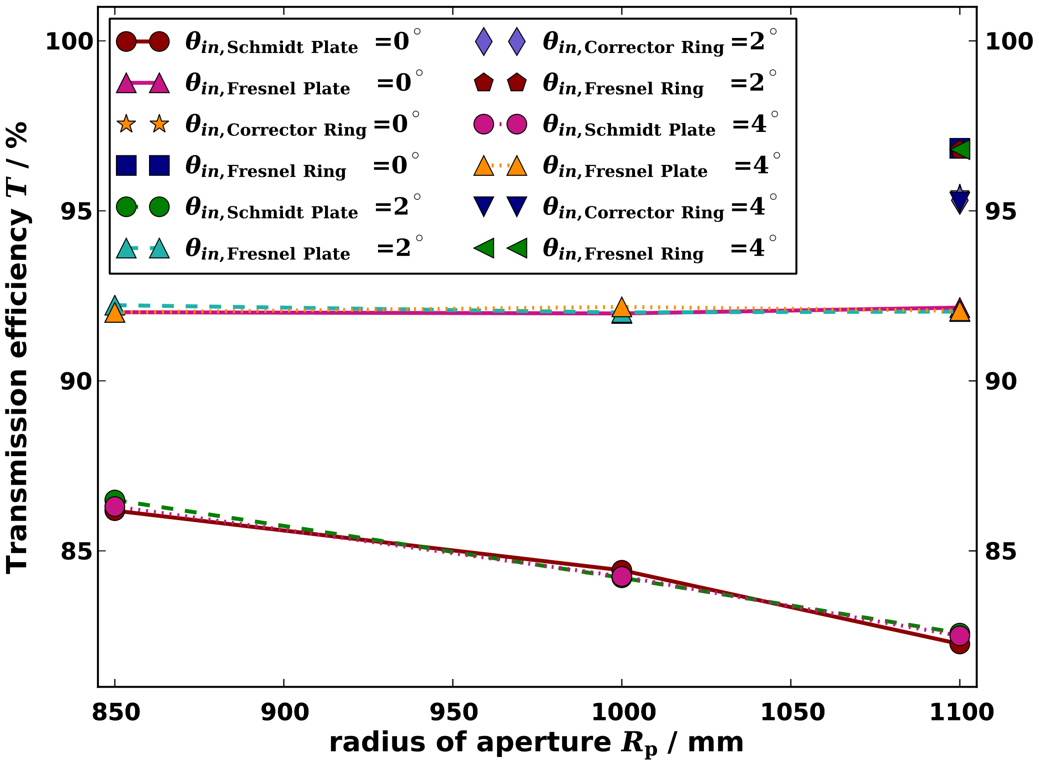

Figure 6.11: Comparison of the transmission efficiency of the Schmidt and the Fresnel corrector plate. The efficiency of the Fresnel plate (dashed lines) exceeds those of the Schmidt plate (solid lines). The transmission is comparable for all incident angles of one plate type.

plates are made of PMMA. Over 92% of the emitted photons are transmitted through the Fresnel plate, compared to $\simeq$ 85% for the bulky Schmidt plate. The grooves of the Fresnel plate are thereby located on a common base plate with a thickness of 1 mm. The thickness of the base plate of the Fresnel corrector corresponds to the base plate of the Schmidt corrector.

Also the transmission efficiency of an aperture radius of 1100 mm including a Schmidt corrector ring and a Fresnel corrector ring, each covering only the outer part of the aperture $R_{\text{ring}} = [850\,\text{mm}, 1100\,\text{mm}]$ is depicted.

It has to be noted, that the Schmidt corrector ring is made of optical glass BK7 and has a transmission efficiency of $T = 88.5\,\%$. The glass has an improved transmission (datasheet 3) compared to PMMA (transmission 2). However, as a Fresnel plate is a highly complex device, the manufacturing of a Fresnel plate made of glass would be quite challenging.

A screenshot of a Geant4 visualisation of the Schmidt telescope where the spherical aberration introduced by the spherical mirror is compensated by a Fresnel plate is illustrated in figure 6.12.

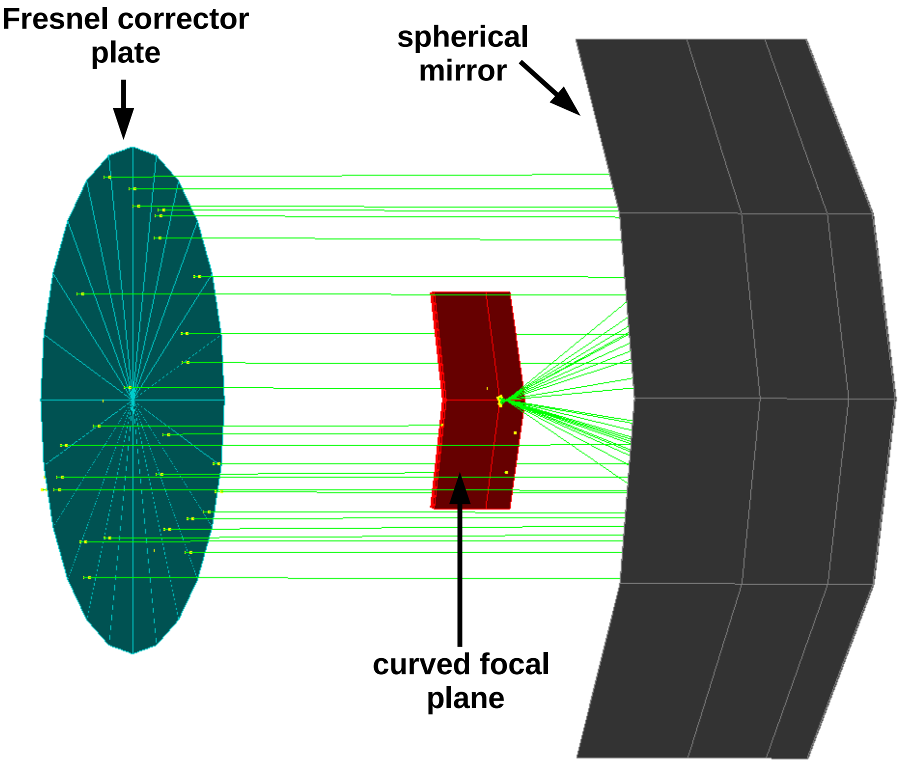

Figure 6.12: Visualisation of the Schmidt telescope simulated by Geant4. A Fresnel plate corrects spherical aberration introduced by the spherical primary mirror.

By the optimisation of the reflective Schmidt camera design, the following baseline design parameters are assumed:

$$R_{\mathrm{p}} = 1100\,\mathrm{mm} \tag{6.3}$$

$$R_{\mathrm{fp}} = 1776\,\mathrm{mm} \tag{6.4}$$

$$r_{90} \simeq 8\,\mathrm{mm} \tag{6.5}$$

6.2.1 The Fluorescence Detector of the Pierre Auger Observatory

The Schmidt camera optics shows a promising performance, regarding image quality and transmission efficiency, to detect fluorescence light by a Schmidt telescope with an implemented SiPM camera and a Fresnel corrector plate.
The Schmidt camera optics is already successfully installed at the fluorescence detector (FD) of the Pierre Auger Observatory, although a corrector ring instead of a corrector plate is chosen to reduce the spherical aberration. The corrector ring allows also a reduction of weight and absorption while a large part of the aperture is free of material and the ring is made of optical glass. The simulated spot size of approximately 13 mm in diameter for all incident angles is sufficient enough for the use of photomultiplier tubes.

The optical properties of the FD are summarised in table 6.2 and are illustrated in figure 6.13 [5].

Aperture	R_p	1100 mm
Radius of curvature of mirror	R_mirror	3400 mm
Radius of curvature of focal plane	R_fp	1743 mm
Aberration radius	r_{90}	$\simeq 6.5$ mm
Side to side pitch of pixel	d_px	40 mm
Number of pixels	n_px	440 PMTs, hexagonal packaging
Pixel field of view angle	α_px	1.5 °
Total field of view	FoV	30 ° × 30 ° in azimuth and elevation
Transmission efficiency of corrector ring	T	95 %

Table 6.2: Parameters of the telescope design of the fluorescence detector at the Pierre Auger Observatory [5].

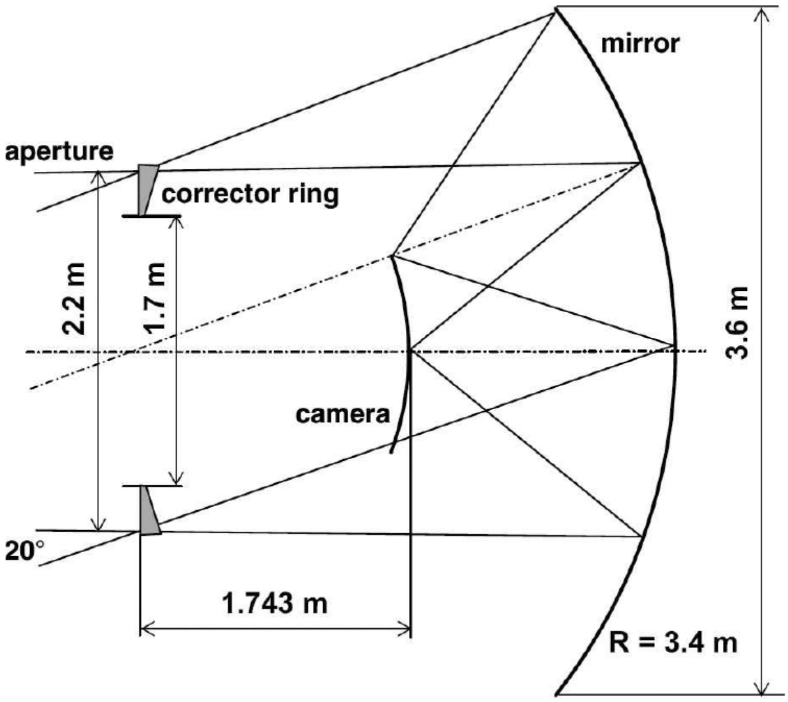

Figure 6.13: Sketch of a telescope of the fluorescence detector as used at the Pierre Auger Observatory [5].

Aperture	R_p	1100 mm
Radius of curvature of mirror	R_mirror	3400 mm
Radius of curvature of focal plane	R_fp	1776 mm
Aberration radius	r_{90}	$\simeq 8\,\mathrm{mm}$
Total field of view	FoV	30 °
Transmission efficiency of Fresnel corrector plate	T	92 %

Table 6.3: Parameters of a possible telescope design of a reflective fluorescence detector with a silicon photomultiplier camera.

As based on the same dimensions of the aperture, the mirror and the focal length as the FD of the Pierre Auger Observatory, further parameters of the chosen baseline design for the Fresnel plate concept can be roughly estimated by assuming other optical quantities also as related (cf. table 6.3):
Simulations of the FD show only a slight increase of the aberration radius while the incident angle is increased for a perfect alignment of the optical system. As for the Schmidt telescope with a Fresnel plate a similar behaviour is indicated at least for small incident angles, the pixel size is estimated as $r_{90} \simeq 8\,\mathrm{mm}$ for the upper boundary of the expected performance. Also the field of view is assumed to be in the same range as the FoV of the FD.

As a rough estimation, the aberration radius of the Fresnel plate concept for the same size of aperture is of the same size of the aberration radius of a Schmidt telescope using a corrector ring to compensate for aberrations.

However, the further quantities have been only assumed as well as the parameters of the fluorescence detector at the Pierre Auger Observatory are based on more realistic simulations. The mirror and the corrector ring is segmented to reduce its cost and small spaces between the segments reduce the reflection efficiency of the mirror. Taking such effects into account will lead to a more realistic and increased r_{90} radius also for the Schmidt telescope with a Fresnel plate. Thus, a more dedicated study of the Fresnel plate Schmidt optic has to be performed.

6.3 Evaluation

The reflective design of the Schmidt camera optics has been studied for the implementation of the SiPM camera of FAMOUS. As image quality criterion, the minimal aberration radius r_{90} has been determined as a function of the size of the aperture.

The classical Schmidt telescope is based on a spherical mirror and a thin aspheric Schmidt corrector plate to reduce spherical aberration. By implementing the corrector plate, the Schmidt telescope becomes nearly free from all aberrations which is translated into an excellent image quality even for aperture radii beyond 1 m. However, the plate also reduces the overall transmission efficiency of the optical system due to absorption in the bulky material.

To avoid too much loss of the already small fluxes of the fluorescence light, a study of an approximation of the Schmidt corrector by a Fresnel corrector has been performed. A configuration of the Fresnel lens can be found for which the image quality becomes sufficient for the use of small sized light detection devices for all incident angles. The performance is compared to the currently used fluorescence detector with a corrector ring at the Pierre Auger Observatory and a similar image quality and transmission efficiency is estimated.

The Fresnel plate is a highly complex optical component requiring a stable manufacturing with uncertainties below $\mathcal{O}(\,\mu\text{m})$.
To obtain such a large Fresnel plate within these resolutions may be become expensive. Furthermore, the stability of such a thin device has to be ensured by a support with a thin and rigid grid which would reduce the transmission, or by applying an increased size of the base plate which would lead to loss of light due to absorption. If, though, a precise manufacturing process can be established, the reproduction of multiple PMMA Fresnel plates may be become faster and less expensive.

The JEM-EUSO experiment utilizes large Fresnel lenses to improve the image quality [53]. The detector orbits the earth and is located on the International Space Station (ISS). By a complex refractive design consisting of several Fresnel lenses, the fluorescence light, emitted by cosmic rays induced air showers, is focused on a PMT camera. Among the Fresnel lenses, a lens with a groove height of $0.7\,\mu\text{m}$ is manufactured with a high accuracy. Therefore, such thin Fresnel lenses can be realised.

However, the replacement of a continuous corrector ring by a Fresnel corrector ring will not significantly improve the performance of the Schmidt telescope and is thus not preferred. Since for SiPMs a smaller aberration radius is preferable, a Schmidt corrector ring with a smaller inner radius may reduce the effect of spherical aberrations. Thereby, a compromise between a high transmission efficiency and an improved image quality has to be found.

A Schmidt telescope using an SiPM camera needs the same number of pixels than the Pierre Auger fluorescence detector camera consisting of 440 photomultiplier tubes if the same field of view per pixel $\alpha_{\text{px}} = 1.5\,^{\circ}$ is required. The aberration radii for both telescope designs allow also the choice of smaller field of view per pixel. Decreasing the pixel field of view may allow a finer sampling of the longitudinal profile of an extensive air shower (EAS). The EAS can be studied in more detail.

A dedicated study for the Schmidt telescope implementing an SiPM camera and a corrector ring is required. The amount of detected light compared to the night-sky-brightness and the intrinsic noise of the SiPM has to be determined as well as the optimal field of view per pixel should be reviewed.

Chapter 7

Summary and Outlook

The reflective telescope design of the Schmidt camera optics with an aperture diameter of $D = 2200\,\mathrm{mm}$ allows the implementation of a silicon photomultiplier (SiPM) camera to detect extensive air showers. By a Fresnel plate, a Schmidt corrector can be sufficiently approximated as well as a sufficient transmission efficiency of the optical system can be achieved. Regarding the image quality, a corrector ring is preferred as used at the fluorescence detector of the Pierre Auger Observatory which is also based on a Schmidt camera optics layout.

The use of the small sized light detection devices SiPMs decreases the available pixel sizes as for the fluorescence detector of the Pierre Auger Observatory. A smaller field of view per pixel is obtained. This may improve the resolution of the measurement of the longitudinal profile of extensive air shower initiated by cosmic rays.

The most crucial determined requirement for the Fresnel corrector plate is a groove height of $\mathcal{O}(\mu m)$. Therefore, the needed accuracy has to be determined and a manufacturing process has to be found to estimate the capability and costs of such a reflective design.

The approximation of the Fresnel corrector plate is based on the construction principle of a Fresnel lens. This has been investigated by studying a refractive design based on a relatively large Fresnel lens to focus the incoming fluorescence light onto the focal plane. Possible methods for an optimisation of the Fresnel lens layout have been performed to allow the use of silicon photomultipliers for large aperture refractive designs. By the approximation of a bulky lens and the subdivision into concentric grooves, the imaging characteristics of the lens are changed due to a displacement of the corresponding part of the bulky lens onto a common base plate. A parametrisation for this optimisation has been found for a small amount of grooves per mm. The Fresnel lens is only optimised for the corresponding incident angle for which the parametrisation has been determined. Here, a significant improvement can be found and the effect of displacement should be taken into account. However, for all other incident angles the parametrisation leads to a small deterioration. A dedicated study by the commercial optics software ZEMAX is thus proposed to find an overall optimisation for the complete range of incident angles. Nevertheless, the refractive optical design with a large aperture may be not sufficient for the purpose of the small size of the SiPMs.

As the FAMOUS prototype shows a promising simulated detector performance, the question arises, how to implement the novel detection technique of an SiPM camera at its best in a large ground-based experiment as the Pierre Auger Observatory.

A large exposure, needed due to the small fluxes of the cosmic rays in the ultra-high energy regime, can be achieved by implementing an array of few telescopes with a large aperture or by building an array with small sized fluorescence detectors with a smaller spacing between the telescopes. A Monte Carlo study is proposed, to determine the optimal array layout, depending on the telescope parameters as the aperture size, the field of view of the telescope and the trigger probability. Also cosmic ray properties as energy, distance from the telescope to the shower core and the slant depth, at which the shower has its maximum, has to be taken into account.

Bibliography

[1] `http://www.hamamatsu.com/jp/en/product/category/index.html`, Last checked June 6th, 2013.

[2] `http://cerncourier.com/cws/product/P000018334`, Last checked June 6th, 2013.

[3] `http://www.rp-photonics.com/p_i_n_photodiodes.html`, Last checked June 6th, 2013.

[4] `http://www.radiantzemax.com/zemax/`, Last checked July 6th, 2013.

[5] J. Abraham et al., "The Fluorescence Detector of the Pierre Auger Observatory", *Nucl.Instrum.Meth.*, vol. A620, pp. 227–251, arXiv:astro-ph/0907.4282, 2010.

[6] P. Abreu et al., "The Pierre Auger Observatory II: Studies of Cosmic Ray Composition and Hadronic Interaction models", arXiv:astro-ph/1107.4804, 2011.

[7] P. Abreu et al., "Antennas for the Detection of Radio Emission Pulses from Cosmic-Ray induced Air Showers at the Pierre Auger Observatory", *JINST*, vol. 7, pp. P10011, arXiv:astro-ph/1209.3840, 2012.

[8] P. Abreu et al., "Results of a self-triggered prototype system for radio-detection of extensive air showers at the Pierre Auger Observatory", *JINST*, vol. 7, pp. P11023, arXiv:astro-ph/1211.0572, 2012.

[9] P. Abreu et al., "The Pierre Auger Observatory V: Enhancements", *J.Phys.Conf.Ser.*, vol. 375, pp. 052006, arXiv:astro-ph/1107.4807, 2012.

[10] S. Agostinelli et al., "Geant4 - a simulation toolkit", *Nuclear Instruments and Methods in Physics Research Section A: Accelerators, Spectrometers, Detectors and Associated Equipment*, vol. 506, no. 3, pp. 250 – 303, `http://www.sciencedirect.com/science/article/pii/S0168900203013688`, 2003.

[11] D. Allard, "Extragalactic propagation of ultrahigh energy cosmic-rays", *Astropart.Phys.*, vol. 39-40, pp. 33–43, arXiv:astro-ph/1111.3290, 2012.

[12] D. Allard et al., "Implications of the cosmic ray spectrum for the mass composition at the highest energies", *JCAP*, vol. 0810, pp. 033, arXiv:astro-ph/0805.4779, 2008.

[13] I. Allekotte et al., "The Surface Detector System of the Pierre Auger Observatory", *Nucl.Instrum.Meth.*, vol. A586, pp. 409–420, arXiv:astro-ph/0712.2832, 2008.

[14] J. Allison et al., "Geant4 developments and applications", *Nuclear Science, IEEE Transactions on*, vol. 53, no. 1, pp. 270–278, DOI:10.1109/TNS.2006.869826, 2006.

[15] R. Aloisio, V. Berezinsky, and A. Gazizov, Transition from galactic to extragalactic cosmic rays, *Astropart.Phys.*, vol. 39-40, pp. 129–143, arXiv:astro-ph/1211.0494, 2012.

[16] H. Anderhub et al., "A novel camera type for very high energy gamma-ray astronomy based on Geiger-mode avalanche photodiodes", *JINST*, vol. 4, pp. P10010, arXiv:astro-ph/0911.4920, 2009.

[17] H. Anderhub et al., "Results of the prototype camera for FACT", *Nuclear Instruments and Methods in Physics Research A*, vol. 639, pp. 55–57, DOI:10.1016/j.nima.2010.09.063, May 2011.

[18] T. Antoni et al., "The Cosmic ray experiment KASCADE", *Nucl.Instrum.Meth.*, vol. A513, pp. 490–510, doi:10.1016/S0168-9002(03)02076-X, 2003.

[19] W.D. Apel et al., "The KASCADE-Grande experiment", *Nucl.Instrum.Meth.*, vol. A620, pp. 202–216, 2010.

[20] S. Argiro et al., "The Offline Software Framework of the Pierre Auger Observatory", *Nucl.Instrum.Meth.*, vol. A580, pp. 1485–1496, arXiv:astro-ph/0707.1652, 2007.

[21] F. Arqueros, J. R. Hoerandel, and B. Keilhauer, "Air Fluorescence Relevant for Cosmic-Ray Detection - Summary of the 5th Fluorescence Workshop, El Escorial 2007", *Nucl.Instrum.Meth.*, vol. A597, pp. 1–22, arXiv:astro-ph/0807.3760, 2008.

[22] P. Auger, P. Ehrenfest, R. Maze, J. Daudin, and R. A. Fréon, "Extensive Cosmic-Ray Showers", *Reviews of Modern Physics*, vol. 11, pp. 288–291, DOI:10.1103/RevModPhys.11.288, July 1939.

[23] M. Ave et al., "Spectrally resolved pressure dependence measurements of air fluorescence emission with AIRFLY", *Nuclear Instruments and Methods in Physics Research Section A: Accelerators, Spectrometers, Detectors and Associated Equipment*, vol. 597, no. 1, pp. 41 – 45, `http://www.sciencedirect.com/science/article/pii/S016890020801276X`, 2008.

[24] M. Ave et al., "Extensive Air Shower Universality of Ground Particle Distributions", *ICRC 2011, Beijing*, 2011.

[25] B. Keilhauer, *"Investigation of Atmospheric Effects on the Development of Extensive Air Showers and their Detection with the Pierre Auger Observatory"*, PhD thesis, Karlsruhe Institute of Technology (KIT), 2004.

[26] Benjamin Glauss, *"Optical Test Stand and SiPM characterization studies"*, Master thesis, RWTH Aachen University, III. Physikalisches Institut A, 2012.

[27] J. Beringer et al., *Phys. Rev. D86*, `http://pdg.lbl.gov`, 2012.

[28] J. Blumer, R. Engel, and J. R. Hoerandel, "Cosmic Rays from the Knee to the Highest Energies", *Prog.Part.Nucl.Phys.*, vol. 63, pp. 293–338, arXiv:astro-ph/0904.0725, 2009.

[29] M. Bohacova, "Study of the Air Fluorescence by AIRFLY", *Nuclear Physics B - Proceedings Supplements*, vol. 190, pp. 266–271, `http://dx.doi.org/10.1016/j.nuclphysbps.2009.03.098`, 2009.

[30] F.I. Boley, "Atmospheric Čerenkov Radiation from Cosmic-Ray Air Showers", *Rev. Mod. Phys.*, vol. 36, pp. 792–808, doi:10.1103/RevModPhys.36.792, `http://link.aps.org/doi/10.1103/RevModPhys.36.792`, Jul 1964.

[31] Max Born and Emil Wolf, *Principles of Optics*, Cambridge Univ. Press, 2009, 7th (expanded) edition.

[32] CERN, *Technical proposal*, LHC Tech. Proposal. Geneva, 1994, CERN-LHCC-94-38, `http://cdsweb.cern.ch/record/290969`.

[33] Pierre Auger Collaboration, Schwarze Löcher: Die Quellen höchstenergetischer kosmischer Teilchen?, press release, Available online at `http://www.auger.de/news/PRagn/` visited on July 16th 2013.

[34] Pierre Auger Collaboration, The Pierre Auger Project Design Report, *FERMILAB-PUB-96-024*, `www.auger.org/admin`, January 1996.

[35] Pierre Auger Collaboration, The Pierre Auger Project Technical Design Report, `www.auger.org/admin`, October 2001.

[36] The JEM-EUSO Collaboration, "The JEM-EUSO Mission: Contributions to the ICRC 2013", arXiv:astro-ph/1307.7071, 2013.

[37] E. Conti, G. Sartori, and G. Viola, "Measurement of the near-infrared fluorescence of the air for the detection of ultra-high-energy cosmic rays", *Astropart.Phys.*, vol. 34, pp. 333–339, arXiv:astro-ph/1008.0329, 2011.

[38] J. Costa, M. Pimenta, and B. Tomé, "A Geant4 Based Engineering Tool for Fresnel Lenses", *Nuclear Science, IEEE Transaction on*, vol. 54, no. 2, pp. 313–319, 2007.

[39] D. Wilson, *"Angular Dependence of the Relative Photon Detection Efficiency of Silicon Photomultipliers"*, Bachelor thesis, RWTH Aachen University, III. Physikalisches Institut A, September 2012.

[40] A. Davis and F. Kühnlenz, "Optical Design using Fresnel Lenses", *Optik & Photonik*, vol. 2, no. 4, pp. 52–55, `http://dx.doi.org/10.1002/opph.201190287`, 2007.

[41] A Davis, K. Levesque, and S. Wilt, Prism peak rounding in injection molded Fresnel lens solar concentrators, Technical paper, May 2011, `http://www.orafol.com/energy/americas/en/technical-papers`.

[42] V. de Souza, "An update on the measurement of the depth of the shower maximum made at the Pierre Auger Observatory", *33rd International Cosmic Ray Conference, Rio de Janeiro*, 2013.

[43] B. Dolgoshein, R. Mirzoyan, E. Popova, P. Buzhan, A. Ilyin, V. Kaplin, A. Stifutkin, M. Teshima, and A. Zhukov, "Large area UV SiPMs with extremely low cross-talk", *Nuclear Instruments and Methods in Physics Research Section A: Accelerators, Spectrometers, Detectors and Associated Equipment*, vol. 695, no. 0, pp. 40 – 43, DOI:10.1016/j.nima.2011.12.024, 2012.

[44] Michael Eichler, private communication.

[45] S. Eidelman et al., "Review of Particle Physics: Cosmic rays", *Physics Letters B*, vol. 592, pp. 1+, `http://pdg.lbl.gov`, 2004.

[46] E. Fermi, "On the Origin of the Cosmic Radiation", *Phys. Rev.*, vol. 75, pp. 1169–1174, DOI:10.1103/PhysRev.75.1169, Apr 1949.

[47] R. C. Fernow, *"Introduction to experimental particle physics"*, Cambridge Univ. Pr., 1986.

[48] T. K. Gaisser and A. M. Hillas, *Proc. 15th ICRC Plovdiv, Bulgaria*, vol. 8, pp. 353, 1977.

[49] Thomas K. Gaisser, *Cosmic Rays and Particle Physics.*, American Institute of Physics, 1979, 10., erw. Aufl.

[50] Schott GmbH, Optical Glass Collection Datasheets, April 2013, `http://www.schott.com`.

[51] J.G. Gonzalez, "The Offline Software of the Pierre Auger Observatory: Lessons Learned", arXiv:astro-ph/1208.2154, 2012.

[52] K. Greisen, "Cosmic Ray Showers", *Annual Review of Nuclear Science*, vol. 10, no. 1, pp. 63–108, DOI:10.1146/annurev.ns.10.120160.000431, 1960.

[53] Y. Hachisu et al., "JEM-EUSO lens manufacturing", 32ND INTERNATIONAL COSMIC RAY CONFERENCE, BEIJING 2011 .

[54] A. M. Hillas, "The Origin of Ultra-High-Energy Cosmic Rays", *Annual Review of Astronomy and Astrophysics*, vol. 22, no. 1, pp. 425–444, DOI:10.1146/annurev.aa.22.090184.002233, 1984.

[55] H. Hinterberger and R. Winston, "Efficient Light Coupler for Threshold Čerenkov Counters", *Review of Scientific Instruments*, vol. 37, pp. 1094–1095, DOI:10.1063/1.1720428, August 1966.

[56] Jorg R. Hoerandel, Models of the knee in the energy spectrum of cosmic rays, *Astropart.Phys.*, vol. 21, pp. 241–265, arXiv:astro-ph/0402356, 2004.

[57] J. Rennefeld, *"Studien zur Eignung von Silizium Photomultipliern für den Einsatz im erweiterten CMS Detektor am SLHC"*, Diploma thesis, RWTH Aachen University, February 2010.

[58] T. Jannson and R. Winston, "Liouville's theorem and concentrator optics", *Journal of the Optical Society of America A*, vol. 3, pp. 7–8, DOI:10.1364/JOSAA.3.000007, January 1986.

[59] K. Kamata and J. Nishimura, "The Lateral and the Angular Structure Functions of Electron Showers", *Progress of Theoretical Physics Supplement*, vol. 6, pp. 93–155, DOI:10.1143/PTPS.6.93, 1958.

[60] B. Keilhauer et al., "Nitrogen fluorescence in air for observing extensive air showers", arXiv:astro-ph/1210.1319, 2012.

[61] Hamamatsu Photonics K.K., MPPC Selection Guide, July 2013.

[62] A. Letessier-Selvon and T. Stanev, "Ultrahigh Energy Cosmic Rays", *Rev.Mod.Phys.*, vol. 83, pp. 907–942, arXiv:astro-ph/1103.0031, 2011.

[63] R. Leutz and Suzuki. A., *Nonimaging Fresnel Lenses: Design and Performance of Solar Concentrators*, Springer Verlag, 2001.

[64] Markus Lauscher, *"Characterisation Studies of Silicon Photomultipliers for the Detection of Fluorescence Light from Extensive Air Showers"*, Master thesis, RWTH Aachen University, January 2012.

[65] J. Matthews, "A Heitler model of extensive air showers", *Astroparticle Physics*, vol. 22, no. 5–6, pp. 387 – 397, DOI:10.1016/j.astropartphys.2004.09.003, 2005.

[66] C. Meurer and N. Scharf, "HEAT - a low energy enhancement of the Pierre Auger Observatory", *Astrophys.Space Sci.Trans.*, vol. 7, pp. 183–186, arXiv:astro-ph/1106.1329, 2011.

[67] M. Nagano and A. A. Watson, "Observations and implications of the ultrahigh-energy cosmic rays", *Rev. Mod. Phys.*, vol. 72, pp. 689–732, DOI:10.1103/RevModPhys.72.689, Jul 2000.

[68] T.. Niggemann et al., "Status of the Silicon Photomultiplier Telescope FAMOUS for the Fluorescence Detection of UHECRs", *33rd International Cosmic Ray Conference, Rio de Janeiro*, 2013.

[69] Tim Niggemann, private communication.

[70] Barthel Philipps, private communication.

[71] T. Pierog et al., "First results of fast one-dimensional hybrid simulation of EAS using CONEX", *Nucl.Phys.Proc.Suppl.*, vol. 151, pp. 159–162, arXiv:astro-ph/0411260, 2006.

[72] T. Pierog and K. Werner, "EPOS Model and Ultra High Energy Cosmic Rays", *Nucl.Phys.Proc.Suppl.*, vol. 196, pp. 102–105, arXiv:hep-ph/0905.1198, 2009.

[73] R. Meissner, *"Brightness Measurements of Stars and the Night-Sky with a Silicon-Photomultiplier-Telescope"*, Bachelor thesis, RWTH Aachen University, III. Physikalisches Institut A, September 2012.

[74] M. Risse and D. Heck, "Energy release in air showers", *Astropart.Phys.*, vol. 20, pp. 661, arXiv:astro-ph/0308158, 2004.

[75] S. Mann, *"Measurement of the UV Reflectivity of Aluminium in Different Stages of Oxidation"*, Bachelor thesis, RWTH Aachen University, III. Physikalisches Institut A, September 2012.

[76] O. Scholten, K. D. de Vries, and K. Werner, "Coherent radiation from extensive air shower", *Nucl.Instrum.Meth.*, vol. A662, pp. S80–S84, arXiv:astro-ph/1010.5268, 2012.

[77] D. J. Schroeder, *Astronomical Optics.*, Acadamic Press, 2000, 2nd edition.

[78] Gottfried Schroeder and Hanskarl Treiber, *Technische Optik - Grundlagen und Anwendungen.*, Vogel, 2007, 10., erw. Aufl.

[79] R. Sparvoli, "Direct measurements of cosmic rays in space", *Nuclear Physics B - Proceedings Supplements*, vol. 239–240, no. 0, pp. 115 – 122, `http://dx.doi.org/10.1016/j.nuclphysbps.2013.05.019`, 2013.

[80] T. Stanev, P. L. Biermann, and T. K. Gaisser, "Cosmic rays. 4. The Spectrum and chemical composition above 10^4 GeV", arXiv:astro-ph/9303006, 1993.

[81] M. Stephan, T. Hebbeker, M. Lauscher, C. Meurer, T. Niggemann, and J. Schumacher, "Future use of silicon photomultipliers for the fluorescence detection of ultra-high-energy cosmic rays", In *Society of Photo-Optical Instrumentation Engineers (SPIE) Conference Series*, volume 8155, September 2011, DOI:10.1117/12.893089.

[82] T. Niggemann, *"New Telescope Design with Silicon Photomultipliers for Fluorescence Light Detection of Extensive Air Showers"*, Master thesis, RWTH Aachen University, January 2012.

[83] Trevor C. Weekes, *Very high energy gamma-ray astronomy*, IOP, Bristol, 2003.

[84] W. T. Welford and R. Winston, *"The optics of nonimaging concentrators: light and solar energy"*, Acad. Press, New York, 1978.

[85] K. Werner, "The hadronic interaction model EPOS", *Nucl.Phys.Proc.Suppl.*, vol. 175-176, pp. 81–87, DOI:10.1016/j.nuclphysbps.2007.10.012, 2008.

[86] R. N. Wilsone, *Reflecting Telescope Optics I.*, Astronomy,Astrophysics Library, 2004, 2. ed., repr.

[87] R. Winston, J.C. Miñano, and P. Benítez, *Nonimaging Optics*, Electronics & Electrical. Elsevier Academic Press, 2005.

[88] S. Yoshida, *Ultra-high Energy Particle Astrophysics*, Nova Science Publishers, 2003.

Appendix A.

Reflexite® positive Fresnel lenses

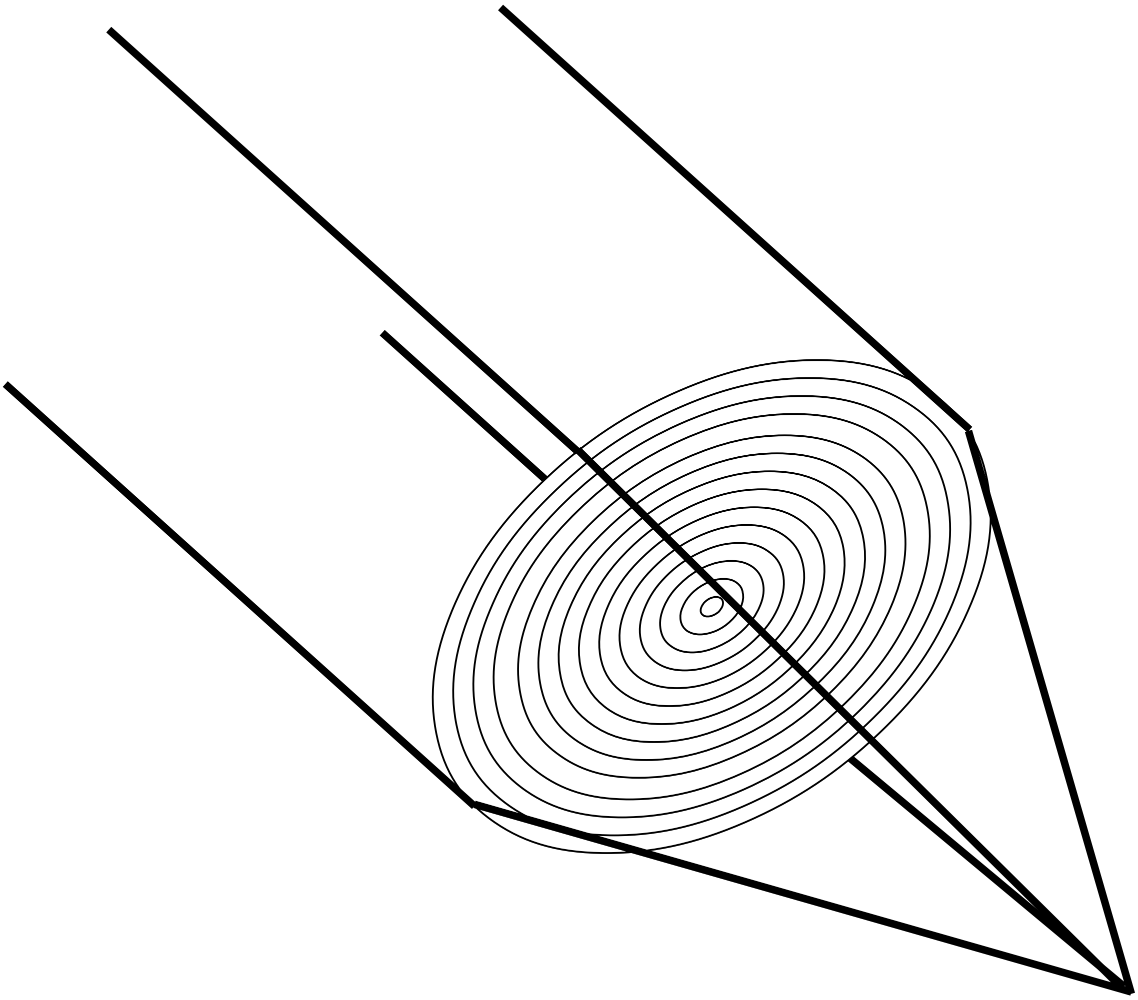

Figure 1: Illustration of a positive Fresnel lens. A collimated input beam is concentrated into one point.

Reflexite®
ENERGY SOLUTIONS

POSITIVE FRESNELLINSEN

Teilenummer	Brennweite	Rillenabstand	Schnittweite Fresnelfläche	Schnittweite Planfläche	Freie Öffnung	Dicke
SC 230	6,3 mm	0,102 mm	6,3 mm	unendlich	10,0 mm	1.8 mm
SC 245	10,8 mm	0,125 mm	10,8 mm	unendlich	6,4 mm	1.8 mm
SC 926	16,1 mm	0,102 mm	unendlich	16,1 mm	7,0 mm	1.8 mm
SC 231	16,3 mm	0,127 mm	unendlich	16,3 mm	18,0 mm	1.8 mm
SC 259	18,3 mm	0,254 mm	unendlich	18,3 mm	17,3 mm	1.8 mm
SC 253	24,0 mm	0,475 mm	unendlich	24,0 mm	23,3 mm	1.8 mm
SC 256	26,6 mm	0,508 mm	unendlich	26,6 mm	59,7 mm	1.8 mm
SC 258	28,7 mm	0,635 mm	unendlich	28,7 mm	45,0 mm	1.8 mm
SC 234	38,0 mm	0,381 mm	38,0 mm	unendlich	56,3 mm	1.8 mm
SC 244	40,8 mm	0,381 mm	40,8 mm	unendlich	86,9 mm	1.8 mm
SC 297	42,4 mm	0,076 mm	42,4 mm	unendlich	29,8 mm	1.8 mm
SC 252	48,3 mm	0,076 mm	48,3 mm	unendlich	63,3 mm	1.8 mm
SC 235	50,8 mm	0,229 mm	unendlich	50,8 mm	77,0 mm	1.8 mm
SC 241	51,0 mm	0,762 mm	51,0 mm	unendlich	109,8 mm	1.8 mm
SC 211	57,8 mm	0,076 mm	263,9 mm	74,0 mm	88,4 mm	1.8 mm
SC 277	68,5 mm	0,076 mm	unendlich	68,5 mm	88,9 mm	1.8 mm
SC 250	69,6 mm	0,279 mm	unendlich	69,6 mm	75,4 mm	1.8 mm
SC 236	72,5 mm	0,279 mm	unendlich	72,5 mm	101,3 mm	1.8 mm
SC 251	76,3 mm	0,127 mm	76,3 mm	unendlich	82,1 mm	1.8 mm
SC 237	77,5 mm	0,254 mm	unendlich	77,5 mm	59,4 mm	1.8 mm
SC 949	97,1 mm	0,254 mm	unendlich	97,1 mm	201,8 mm	1.8 mm
SC 242	101,1 mm	0,305 mm	101,1 mm	unendlich	85,8 mm	1.8 mm
SC 239	102,8 mm	0,508 mm	unendlich	102,8 mm	133,9 mm	1.8 mm
SC 228	111,8 mm	0,508 mm	unendlich	111,8 mm	164,0 mm	1.8 mm
SC 255	128,3 mm	0,254 mm	unendlich	128,3 mm	126,7 mm	1.8 mm
SC 948	129,1 mm	0,350 mm	unendlich	129,1 mm	180,5 mm	1.8 mm
SC 209	137,8 mm	0,254 mm	unendlich	137,8 mm	151,0 mm	1.8 mm
SC 248	151,7 mm	0,127 mm	151,7 mm	unendlich	152,9 mm	1.8 mm
SC 249	152,0 mm	0,381 mm	152,0 mm	unendlich	205,4 mm	1,8 mm
SC 223	152,8 mm	0,254 mm	unendlich	152,8 mm	202,4 mm	1,8 mm
SC 246	203,0 mm	0,457 mm	unendlich	203,0 mm	228,9 mm	1,8 mm
SC 950	219,0 mm	0,302 mm	unendlich	219,0 mm	223,3 mm	1,8 mm
SC 210	225,5 mm	0,178 mm	2007,0 mm	254,0 mm	257,6 mm	1,8 mm
SC 264	234,7 mm	0,508 mm	unendlich	234,7 mm	253,1 mm	1,8 mm

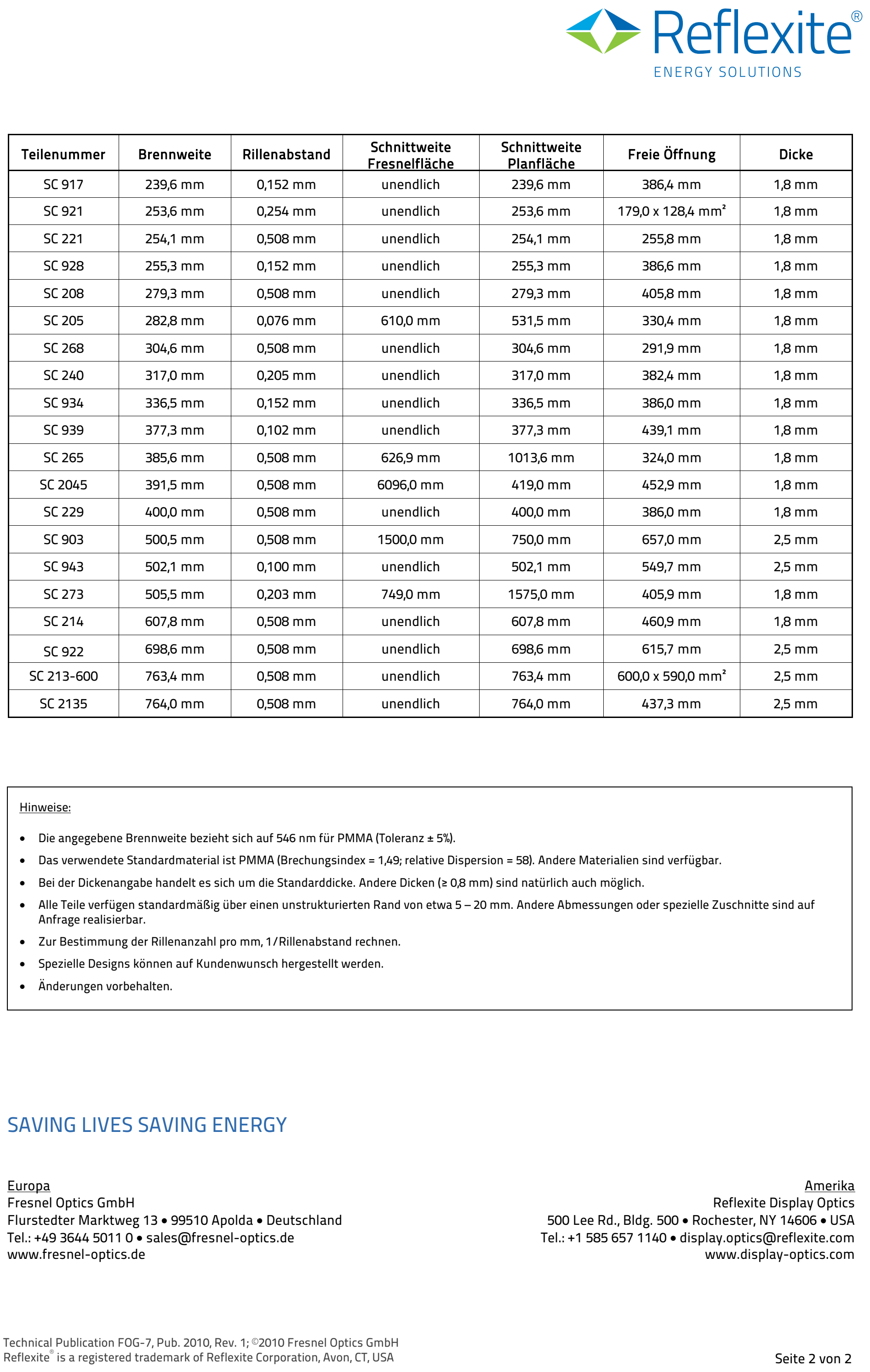

Reflexite®
ENERGY SOLUTIONS

Teilenummer	Brennweite	Rillenabstand	Schnittweite Fresnelfläche	Schnittweite Planfläche	Freie Öffnung	Dicke
SC 917	239,6 mm	0,152 mm	unendlich	239,6 mm	386,4 mm	1,8 mm
SC 921	253,6 mm	0,254 mm	unendlich	253,6 mm	179,0 x 128,4 mm^2	1,8 mm
SC 221	254,1 mm	0,508 mm	unendlich	254,1 mm	255,8 mm	1,8 mm
SC 928	255,3 mm	0,152 mm	unendlich	255,3 mm	386,6 mm	1,8 mm
SC 208	279,3 mm	0,508 mm	unendlich	279,3 mm	405,8 mm	1,8 mm
SC 205	282,8 mm	0,076 mm	610,0 mm	531,5 mm	330,4 mm	1,8 mm
SC 268	304,6 mm	0,508 mm	unendlich	304,6 mm	291,9 mm	1,8 mm
SC 240	317,0 mm	0,205 mm	unendlich	317,0 mm	382,4 mm	1,8 mm
SC 934	336,5 mm	0,152 mm	unendlich	336,5 mm	386,0 mm	1,8 mm
SC 939	377,3 mm	0,102 mm	unendlich	377,3 mm	439,1 mm	1,8 mm
SC 265	385,6 mm	0,508 mm	626,9 mm	1013,6 mm	324,0 mm	1,8 mm
SC 2045	391,5 mm	0,508 mm	6096,0 mm	419,0 mm	452,9 mm	1,8 mm
SC 229	400,0 mm	0,508 mm	unendlich	400,0 mm	386,0 mm	1,8 mm
SC 903	500,5 mm	0,508 mm	1500,0 mm	750,0 mm	657,0 mm	2,5 mm
SC 943	502,1 mm	0,100 mm	unendlich	502,1 mm	549,7 mm	2,5 mm
SC 273	505,5 mm	0,203 mm	749,0 mm	1575,0 mm	405,9 mm	1,8 mm
SC 214	607,8 mm	0,508 mm	unendlich	607,8 mm	460,9 mm	1,8 mm
SC 922	698,6 mm	0,508 mm	unendlich	698,6 mm	615,7 mm	2,5 mm
SC 213-600	763,4 mm	0,508 mm	unendlich	763,4 mm	600,0 x 590,0 mm^2	2,5 mm
SC 2135	764,0 mm	0,508 mm	unendlich	764,0 mm	437,3 mm	2,5 mm

Hinweise:

- Die angegebene Brennweite bezieht sich auf 546 nm für PMMA (Toleranz ± 5%).
- Das verwendete Standardmaterial ist PMMA (Brechungsindex = 1,49; relative Dispersion = 58). Andere Materialien sind verfügbar.
- Bei der Dickenangabe handelt es sich um die Standarddicke. Andere Dicken (≥ 0,8 mm) sind natürlich auch möglich.
- Alle Teile verfügen standardmäßig über einen unstrukturierten Rand von etwa 5 – 20 mm. Andere Abmessungen oder spezielle Zuschnitte sind auf Anfrage realisierbar.
- Zur Bestimmung der Rillenanzahl pro mm, 1/Rillenabstand rechnen.
- Spezielle Designs können auf Kundenwunsch hergestellt werden.
- Änderungen vorbehalten.

SAVING LIVES SAVING ENERGY

Europa
Fresnel Optics GmbH
Flurstedter Marktweg 13 • 99510 Apolda • Deutschland
Tel.: +49 3644 5011 0 • sales@fresnel-optics.de
www.fresnel-optics.de

Amerika
Reflexite Display Optics
500 Lee Rd., Bldg. 500 • Rochester, NY 14606 • USA
Tel.: +1 585 657 1140 • display.optics@reflexite.com
www.display-optics.com

Technical Publication FOG-7, Pub. 2010, Rev. 1; ©2010 Fresnel Optics GmbH

Appendix B.

Material Properties

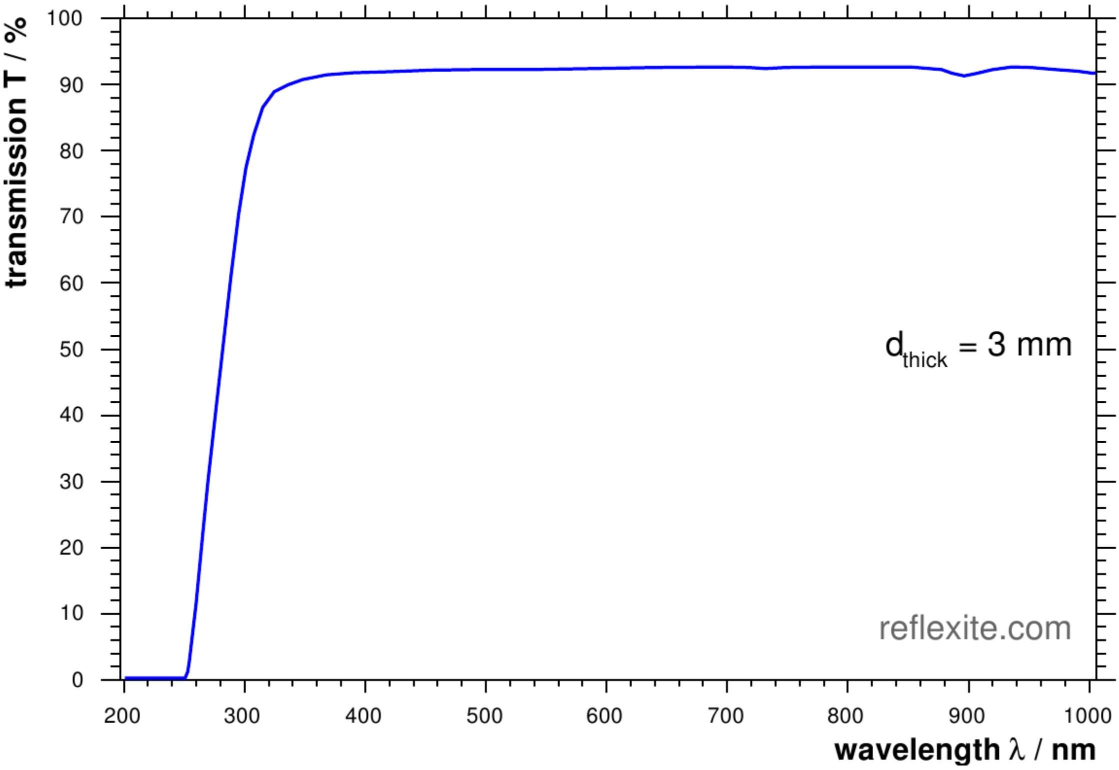

Figure 2: Transmission efficiency T of PMMA as a function of the wavelength λ. Taken from [82].

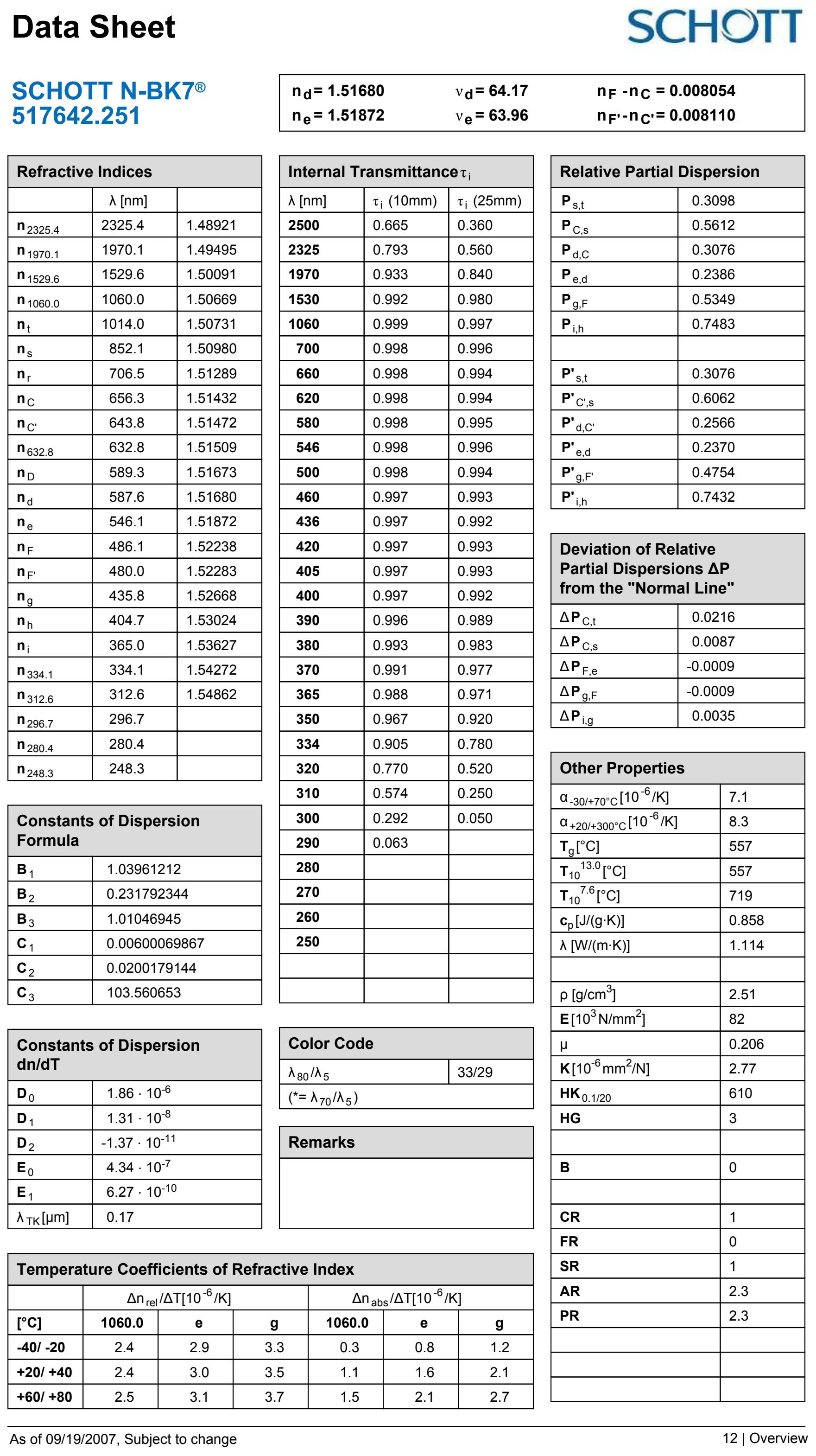

Data Sheet

SCHOTT

SCHOTT N-BK7®
517642.251

n_d = 1.51680	ν_d = 64.17	$n_F - n_C$ = 0.008054
n_e = 1.51872	ν_e = 63.96	$n_{F'} - n_{C'}$ = 0.008110

Refractive Indices

	λ [nm]	
$n_{2325.4}$	2325.4	1.48921
$n_{1970.1}$	1970.1	1.49495
$n_{1529.6}$	1529.6	1.50091
$n_{1060.0}$	1060.0	1.50669
n_t	1014.0	1.50731
n_s	852.1	1.50980
n_r	706.5	1.51289
n_C	656.3	1.51432
$n_{C'}$	643.8	1.51472
$n_{632.8}$	632.8	1.51509
n_D	589.3	1.51673
n_d	587.6	1.51680
n_e	546.1	1.51872
n_F	486.1	1.52238
$n_{F'}$	480.0	1.52283
n_g	435.8	1.52668
n_h	404.7	1.53024
n_i	365.0	1.53627
$n_{334.1}$	334.1	1.54272
$n_{312.6}$	312.6	1.54862
$n_{296.7}$	296.7	
$n_{280.4}$	280.4	
$n_{248.3}$	248.3	

Constants of Dispersion Formula

B_1	1.03961212
B_2	0.231792344
B_3	1.01046945
C_1	0.00600069867
C_2	0.0200179144
C_3	103.560653

Constants of Dispersion dn/dT

D_0	$1.86 \cdot 10^{-6}$
D_1	$1.31 \cdot 10^{-8}$
D_2	$-1.37 \cdot 10^{-11}$
E_0	$4.34 \cdot 10^{-7}$
E_1	$6.27 \cdot 10^{-10}$
λ_{TK} [μm]	0.17

Internal Transmittance τ_i

λ [nm]	τ_i (10mm)	τ_i (25mm)
2500	0.665	0.360
2325	0.793	0.560
1970	0.933	0.840
1530	0.992	0.980
1060	0.999	0.997
700	0.998	0.996
660	0.998	0.994
620	0.998	0.994
580	0.998	0.995
546	0.998	0.996
500	0.998	0.994
460	0.997	0.993
436	0.997	0.992
420	0.997	0.993
405	0.997	0.993
400	0.997	0.992
390	0.996	0.989
380	0.993	0.983
370	0.991	0.977
365	0.988	0.971
350	0.967	0.920
334	0.905	0.780
320	0.770	0.520
310	0.574	0.250
300	0.292	0.050
290	0.063	
280		
270		
260		
250		

Color Code

λ_{80}/λ_5	33/29
(*= λ_{70}/λ_5)	

Remarks

Relative Partial Dispersion

$P_{s,t}$	0.3098
$P_{C,s}$	0.5612
$P_{d,C}$	0.3076
$P_{e,d}$	0.2386
$P_{g,F}$	0.5349
$P_{i,h}$	0.7483
$P'_{s,t}$	0.3076
$P'_{C',s}$	0.6062
$P'_{d,C'}$	0.2566
$P'_{e,d}$	0.2370
$P'_{g,F'}$	0.4754
$P'_{i,h}$	0.7432

Deviation of Relative Partial Dispersions ΔP from the "Normal Line"

$\Delta P_{C,t}$	0.0216
$\Delta P_{C,s}$	0.0087
$\Delta P_{F,e}$	-0.0009
$\Delta P_{g,F}$	-0.0009
$\Delta P_{i,g}$	0.0035

Other Properties

$\alpha_{-30/+70°C}$ [10^{-6}/K]	7.1
$\alpha_{+20/+300°C}$ [10^{-6}/K]	8.3
T_g [°C]	557
$T_{10}^{13.0}$ [°C]	557
$T_{10}^{7.6}$ [°C]	719
c_p [J/(g·K)]	0.858
λ [W/(m·K)]	1.114
ρ [g/cm^3]	2.51
E [10^3 N/mm^2]	82
μ	0.206
K [10^{-6} mm^2/N]	2.77
$HK_{0.1/20}$	610
HG	3
B	0
CR	1
FR	0
SR	1
AR	2.3
PR	2.3

Temperature Coefficients of Refractive Index

	$\Delta n_{rel}/\Delta T$ [10^{-6}/K]			$\Delta n_{abs}/\Delta T$ [10^{-6}/K]		
[°C]	**1060.0**	**e**	**g**	**1060.0**	**e**	**g**
-40/ -20	2.4	2.9	3.3	0.3	0.8	1.2
+20/ +40	2.4	3.0	3.5	1.1	1.6	2.1
+60/ +80	2.5	3.1	3.7	1.5	2.1	2.7

As of 09/19/2007, Subject to change

12 | Overview

Figure 3: Material properties of the glass N-BK7 [50].

Acknowledgements - Danksagungen

Mein erster Dank geht an Herrn Prof. Dr. Hebbeker, der mir in seinem Insitut die Möglichkeit gab, die Arbeit zu verfassen und die dafür notwendige Forschungsarbeit durchzuführen. Ebenso gilt mein Dank Herrn Prof. Dr. Wiebusch, der sich bereit erklärt hat, meine Arbeit als Zweitgutachter zu begleiten. Neben den Gutachtern hatten noch viele andere Anteil am Gelingen dieser Arbeit. Die Auger Arbeitsgruppe hat mich immer tatkräftig mit Ideen und Diskussionen unterstützt. Besonders hervorzuheben sind dabei Tim Niggemann, der sich vornehmlich der Betreuung dieser Arbeit gewidmet hat, sowie meine Büronachbarn Maurice Stephan und Markus Lauscher. Die gute Atmosphäre und ständige Bereitschaft meine Analysen zu diskutieren, haben geholfen, die unterschiedlichsten Aspekte dieses Forschungsgebiets zu beleuchten. Diesbezüglich geht auch ein Dank an Matthias Plum, der sich durch intensives Korrekturlesen an dieser Arbeit verdient gemacht hat. Aber auch außerhalb der Arbeitsgruppe fand ich viel Unterstützung. Die "Hallenbewohner" waren stets zu Anregungen und Hinweisen bereit. An dieser Stelle möchte ich Lukas Koch besonders erwähnen. Seine Inspiration hat die Arbeit stets gefördert. Auch möchte ich mich bei Claire Prouvé, mon lapin rose, bedanken. Sie hat es immer wieder geschafft, mich mit ihrer wundervollen Art zu motivieren und aufzubauen.

Es ist nicht möglich allen zu Danken, die mich bei dem Verfassen dieser Arbeit unterstützt haben. Aber auch allen, die in dieser Auflistung fehlen und trotzdem ihren Anteil an dieser Arbeit hatten, gilt mein Dank.